DEVELOPMENT OF GRAPHENE MATERIALS AND PHTHALOCYANINES FOR APPLICATION IN DYE-SENSITIZED SOLAR CELLS

A thesis submitted in fulfilment

of the requirements for the degree of

Master of Science

of

Rhodes University

By

Francis Chindeka

Grahamstown, South Africa

March 2020

To

My wife Alice, daughters Tapiwa and Vongai for always being there for me, I will always love and cherish you.

My late parents, Vingirai and Martha Chindeka for being my first teachers, raising and nurturing me. You taught me to believe in myself and work hard.

My brothers, sisters and your families for all the support.

My colleagues and friends

This research is dedicated to you all.

Acknowledgements

I wish to acknowledge with much appreciation, all those who made the completion of this research work a possibility.

My great and sincere appreciation goes to my supervisor, Distinguished Professor Tebello Nyokong for the unwavering support, guidance, useful comments and encouragement throughout my studies. Thank you for the many opportunities you afforded me.

To my co-supervisor, Dr. Philani Mashazi, thank you so much for the supervision, guidance and support, you are truly invaluable.

To Professor Rui Krause, thank you so much for all the unwavering support.

To my wife, Alice, daughters Tapiwa and Vongai, I cannot thank you enough for all your understanding, motivation, encouragement and support. Words alone cannot describe how grateful I am.

To my parents, brothers and sisters, thank you so much for raising and nurturing me.

To all my S22 colleagues, thank you so much for all the help and the wonderful times we shared.

To the Chemistry department academic and support staff, thank you all for the different important roles you played.

To the many women and men in the research community who are doing sterling work

Abstract

Two sets of dye-sensitized solar cells (DSSCs) were fabricated. In the first set, dye-sensitized solar cells (DSSC) were fabricated by incorporating graphene materials as catalysts at the counter electrode. Platinum was also used as a catalyst for comparative purposes. Different phthalocyanines: hydroxyl indium tetracarboxyphenoxy phthalocyanine (**1**), chloro indium octacarboxy phthalocyanine (**2**) and dibenzoic acid silicon phthalocyanine (**3**) were used as dyes. Complex **3** gave the highest power conversion efficiency (η) of 3.19% when using nitrogen doped reduced graphene oxide nanosheets (NrGONS) as a catalyst at the counter electrode, and TiO_2 containing rGONS at the anode. The value obtained is close to 3.8% obtained when using Pt catalyst instead of NrGONS at the cathode, thus confirming that NrGONS is a promising candidate to replace the more expensive Pt. The study also shows that placing rGONS on both the anode and cathode improves efficiency.

In the second set, DSSCs were fabricated by using 2(3,5-biscarboxyphenoxy), 9(10), 16(17), 23(24)-tri(tertbutyl) phthalocyaninato Cu (**4**) and Zn (**5**) complexes as dyes on the ITO-TiO_2 photoanodes containing reduced graphene oxide nanosheets (rGONS) or nitrogen-doped rGONS (NrGONS). The evaluation of the assembled DSSCs revealed that using ITO-TiO_2-NrGONS-CuPc (**4**) photoanode had the highest fill factor (FF) and power conversion efficiency (η) of 69 % and 4.36 % respectively. These results show that the asymmetrical phthalocyanine complexes (**4**) and (**5**) showed significant improvement on the performance of the DSSC compared to previous work on symmetrical carboxylated phthalocyanines with η = 3.19%.

Contents **Pages**

List of abbreviations

^{1}H NMR	=	Proton Nuclear Magnetic Resonance
abs	=	Absorbance
AC	=	Alternating current
AFM	=	Atomic force microscope
APCVD	=	Atmospheric pressure chemical vapor deposition
ATR	=	Attenuated total reflectance
BE	=	Binding energy
CB	=	Conduction band
C_{dl}	=	Double layer capacitance
CE	=	Counter electrode
CPE	=	Constant phase element
CV	=	Cyclic voltammetry
CVD	=	Chemical vapor deposition
DBSiPc	=	Dibenzoic silicon phthalocyanine
DBU	=	1,8-diazobicylo[5.4.0]undec-7-ene
DCM	=	Dichloromethane
DMF	=	Dimethylformamide
DLD	=	Delay line detector
DPV	=	Differential pulse voltammetry
DSSCs	=	Dye-sensitized solar cells
$E_{1/2}^{ox}$	=	Half wave potential for the first ring oxidation
$E_{1/2}^{red}$	=	Half wave potential for the first ring reduction
E_g	=	Band gap energy
E_{HOMO}	=	Energy of the highest occupied molecular orbital

EIS	=	Electrochemical impedance spectroscopy
E_{LUMO}	=	Energy of the lowest unoccupied molecular orbital
EVA	=	Evaluation curve fitting software
Fc/Fc^{+}	=	ferrocene/ferrocenium
FF	=	Fill factor
FRA	=	Frequency response analysis
FTO	=	Fluorine doped tin oxide
GCE	=	Glassy carbon electrode
GO	=	Graphite oxide
GONS	=	Graphene oxide nanosheets
HOMO	=	Highest occupied molecular orbital
IOs	=	Invers opals
ITO	=	Indium doped tin oxide
LED	=	Light emitting diode
LUMO	=	Lowest unoccupied molecular orbital
MPcs	=	Metallophthalocyanines
MALDI	=	Matrix assisted laser desorption/ Ionisation
Nd–YAG	=	Neodymium–doped Yttrium Aluminium Garnet
NIR	=	Near infrared
NrGONS	=	Nitrogen doped reduced graphene oxide nanosheets
Pcs	=	Phthalocyanines
PDT	=	Photodynamic therapy
PMT	=	Photomultiplier tube
PVP	=	Polyvinyl pyrrolidone
QDs	=	Quantum dots

RMS	=	Root mean square
rGONS	=	Reduced graphene oxide nanosheets
sccm	=	Standard cubic centimetre per minute
SWV	=	Square wave voltammetry
$TBABF_4$	=	Tetrabutylammonium tetrafluoroborate
TCOs	=	Transparent conductor oxides
TEM	=	Transmission electron microscopy
THF	=	Tetrahydrofuran
TOF	=	Time of flight
TOF-SIMS	=	Time-of-Flight Secondary Ion Mass Spectrometer
TTIP	=	Titanium (iv) tetraisopropoxide
UV	=	Ultraviolet
V_{oc}	=	Open circuit voltage
Vis	=	Visible
XPS	=	X ray photoelectron spectroscopy
XRD	=	X ray diffractometer

List of symbols

α	=	Non-peripheral position
β	=	Peripheral position
η	=	Power conversion efficiency
ω	=	Angular frequency
Ω	=	Ohm
λ	=	Wavelength

List of figures

List of schemes

List of tables

Preamble

The thesis reports on the synthesis and characterisation of graphene materials and metallo phthalocyanines (MPcs) and their application in dye-sensitized solar cells (DSSCs). An overview of DSSCs and MPcs is given.

Chapter 1: Introduction

1.1 Dye-sensitized solar cells

Various environmental concerns and the depletion of fossil fuel have boosted research into alternative sources of clean and sustainable energy including the sun which is the largest and available source. Dye-sensitized solar cells (DSSCs) are low cost thin film solar cells. They have attracted considerable attention since the pioneering work by O'Regan and Grätzel **[1]**. A typical DSSC is assembled by placing an electrolyte, either liquid or solid, containing a redox system in between the photoanode and the photocathode/counter electrode (CE), **Fig. 1.1**. The photoanode consists of highly porous nanocrystalline metal oxide nanoparticles (e.g. titanium dioxide (TiO_2), zinc oxide (ZnO) or hybrid materials) photosensitized by dye molecules. At the photocathode, the reduction of the electrolyte occurs and at the photoanode the oxidation of the same electrolyte occurs. Counter electrodes are commonly composed of ~15–20 nm thick platinum (Pt) layer, deposited onto transparent conductor oxides (TCOs) such as indium doped tin oxide (ITO) **[2, 3]**. Efforts to replace Pt with cheaper materials has gained significant attention. Graphene exhibits remarkable electrical/ electronic, optical and mechanical properties that qualify it for applications in optoelectronic devices **[4].** Hence the motivation to study graphene as part of this thesis

The dye photosensitizer is one of the key DSSC components. For a dye molecule to be an excellent sensitizer, it must possess several functional groups such as carbonyl (C=O) or hydroxyl (-OH) capable of chelating to the Ti (IV) sites on the TiO_2 surface **[2, 3**]. Metallophthalocyanines (MPcs) which are a subject of this thesis, are very well-suited as sensitizers because of their good stability, high extinction coefficients and

the large variety of central metal ions and chemical substituents at different positions of the ligands **[2, 5].**

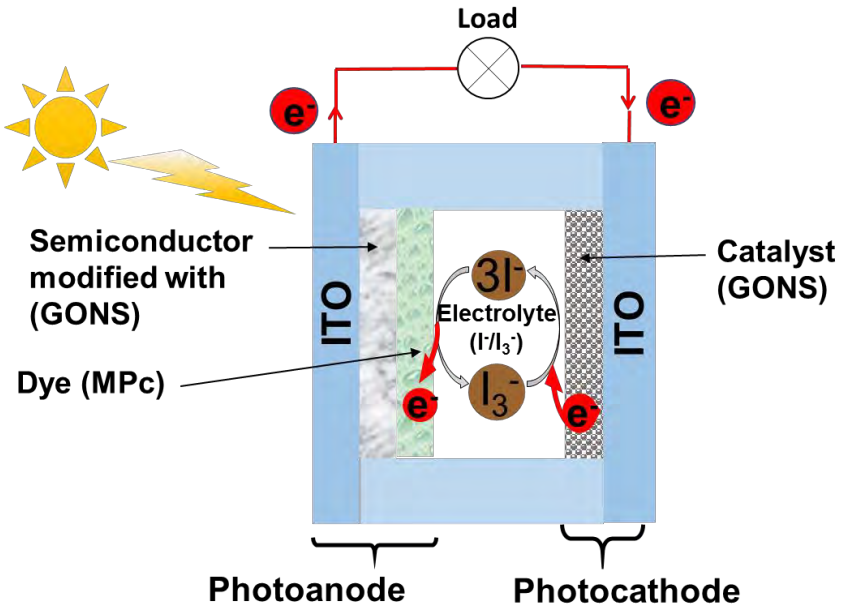

Figure 1.1: Schematic representation of a dye-sensitized solar cell (DSSC) showing graphene oxide nanosheets (GONS) incorporated in the photoanode and photocathode and MPc dye photosensitiser.

Low-symmetry in MPcs is also expected to improve performance of DSSCs due to improved directionality of its electronic orbitals in the excited state, provided by the electron-donating (e.g. phenylthio) “push” groups and electron-withdrawing (e.g. carboxylic acid) “pull” group **[5-8].**

1.2 Graphene materials

Graphene is a one atom thick (~0.34 nm) sheet of sp^2 bonded carbon atoms arranged in a hexagonal honeycomb lattice in which one atom forms each vertex (**Figure 1.2**) **[4]**. Graphene oxide nanosheets (GONS) are chemically modified graphene comprising a single layer of networked carbon atoms and oxygen functional groups, such as epoxides, carboxylic acids, and alcohols. It can be reduced by chemical,

electrochemical or thermal methods to form reduced GONS (rGONS). The structure and properties including electrocatalytic activity of rGONS are somewhere between graphene oxide (an insulator) and pristine graphene (a semi metal), depending on the degree of reduction and starting structure of the graphene oxide **[9-11].** rGONS are lightweight, lack the intrinsic band gap, are transparent, have unparalleled strength, good conductivity and unique levels of white light absorption among other properties. rGONS have great potential for use in transistors, electrocatalysis, photovoltaic cells, supercapacitors, fuel cells and biological sensors **[10-12]**. Hence rGONS are a subject of this thesis.

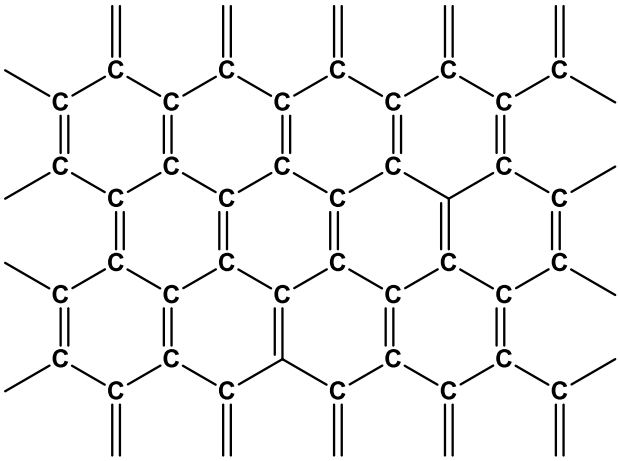

Figure 1.2: Graphene structure.

1.2.1 Synthesis of graphene materials

The synthesis of graphene can be divided into two categories: the top down and the bottom up approaches **(Figure 1.3)**.

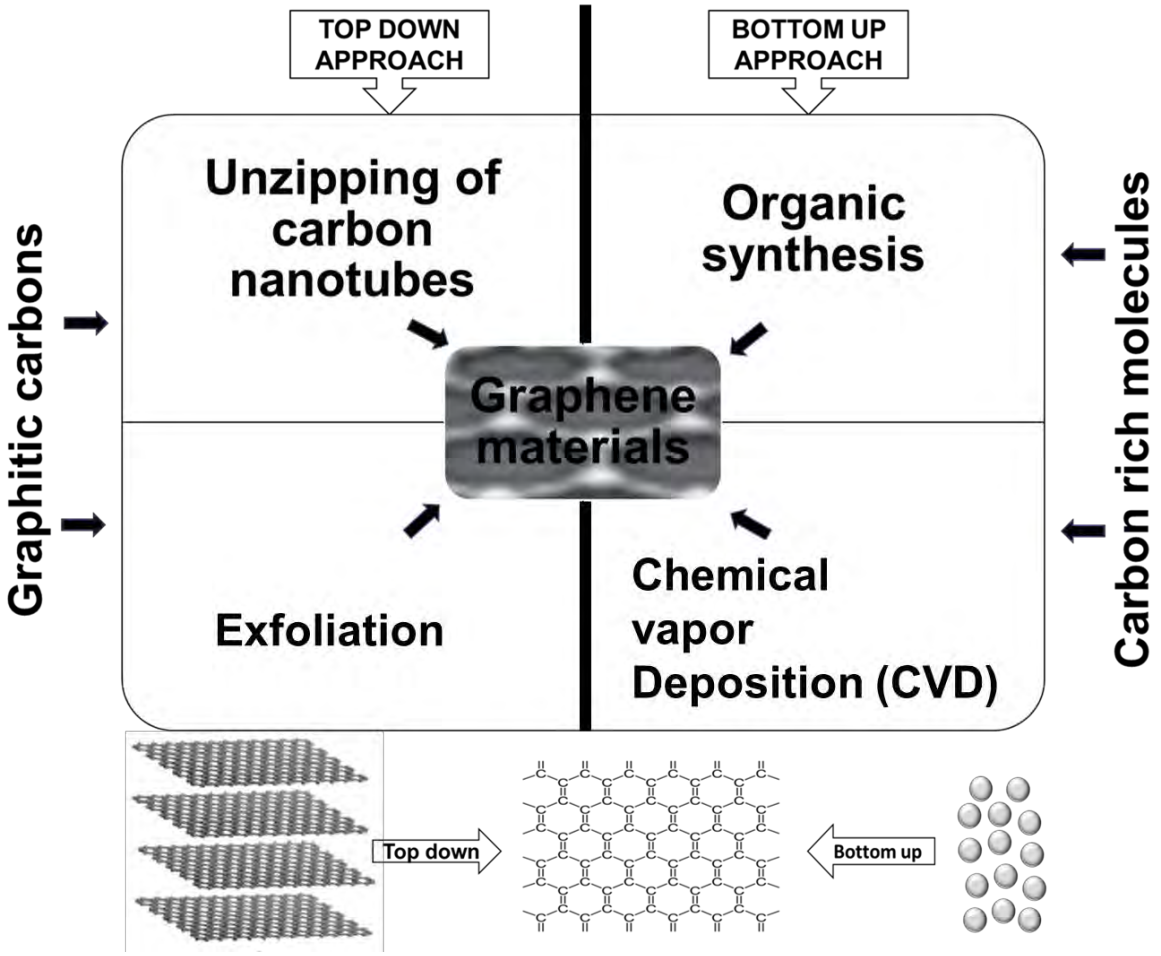

Figure 1.3: Different approaches to synthesising graphene illustrating the top down and bottom up methods.

In the top down approach, precursors of graphene are stripped down to a few layers of graphite by chemical, mechanical or thermal treatments. Some of the methods are mechanical exfoliation, ball milling, micromechanical cleavage of graphite, electrochemical exfoliation, reduction of graphite oxide (GO), graphite intercalation, microwave synthesis using MPc, nanotube slicing, pyrolysis method and sonication **[13-25]**.

The bottom up approach (employed in this work) includes methods like epitaxial growth on silicon carbide (SiC) where graphene is obtained by heating silicon carbide (SiC) at 1100 °C **[26]**. The dry ice method in brief involves completely burning Mg

ribbon inside a dry ice bowl, covered up by another dry ice (solid CO_2) slab **[27].** In chemical vapor deposition (CVD) on transition metals, graphene can be grown on a heated (1000 °C) metal film (e.g. nickel or Cu). This is followed by introducing a gaseous carbonaceous precursor (e.g. methane) under inert conditions (Ar or N_2) at low pressure. If atmospheric pressure is used, the method is called atmospheric pressure chemical vapor deposition (APCVD). This enables the carbon from the methane gas to be absorbed on the nickel or copper film. Cooling down the system with precursor turned off enables the carbon to diffuse out of the nickel or copper surface and form graphene sheets. Nickel is usually used as substrate due to its catalytic activity toward hydrocarbon decomposition and the low solubility of carbon in nickel. This facilitates production of atomically thin films **[9, 10, 13, 14, 28-35]**.

In this work, reduced graphene oxide was prepared by APCVD on Cu foil with C_2H_2 in an Ar and H_2 environment, according to literature methods **[36]** with minor modifications.

1.2.2 Application of graphene materials in dye-sensitized solar cells (DSSCs)

Graphene materials have great potential for applications in all aspects of DSSCs due to their good electrical/ electronic, optical and mechanical properties.

In a DSSC, a photoexcited electron is injected from the dye into the metal oxide semiconductor (TiO_2 or ZnO) where it diffuses to the current collector. Various interfaces in the DSSC can have adverse effects on performance as they play critical roles in charge separation and transport. Electrons generated from the excited dye molecules following absorption of light, are separated at the metal oxide (e.g. TiO_2)/ dye interface. The electrons are then transported through the disordered 3D network of TiO_2 nanoparticles by trap-limited diffusion processes via a number of colloidal

particles and grain boundaries, to the collecting electrode. This random path increases the chance of charge recombination where electrons injected into the metal oxide semiconductor can recombine with the dye or with oxidized species of the redox couple **[10, 37-40],** thus reducing DSSC efficiency. Iodide (I^-) ions in the electrolyte migrate from the counter electrode to the nanopores of the metal oxide semiconductor (e.g. TiO_2) and transfer electrons to the highest occupied molecular orbital (HOMO) level of the dye thus getting oxidised to I^-_3 ions. Some of the I^-_3 ions can then penetrate the porous TiO_2 and be in direct contact with the TCO surface, thereby collecting the electrons from the TCO surface through back transport reaction **[10, 11, 37]**. Losses can also occur due to the voltage drop between the dye lowest unoccupied molecular orbital (LUMO) level and the Fermi level of the metal oxide semiconductor, and the ohmic resistance in the semiconducting layer. Therefore, manipulating the competition between charge transport and charge recombination is key in fabricating high performance DSSCs [**10, 11, 37, 41].** Dense layers of TiO_2 (~20−100 nm thick) are often used as a blocking layer to prevent recombination of electrons at the ITO and the oxidised species of the electrolyte (I^-_3) **[42, 43].** Many groups have sought to use graphene materials to improve the conduction pathways from the point of photogenerated carriers to the collecting electrode in order to improve efficiency. **Kim et al. [10]** used a photocatalytically reduced graphene oxide−TiO_2 nanoparticle composite as blocking layer to prevent recombination between fluorine doped tin oxide (FTO) and I^-_3**.** Some groups have incorporated graphene materials in the metal oxide semiconductor scaffolding to improve photocurrent density in the photoanode. **Yang et. al. [44]** argue that graphene can act as an electron bridge in the photoanode, shuttling electrons to the current collector thus lowering recombination in the device. They also argue that inclusion of graphene induce formation of macropores in the TiO_2

films causing scattering of light**.** Furthermore, when a graphene sheet exists in between TCO and TiO_2, electrons can be transported from TiO_2 to graphene but not in reverse, as the work function of graphene (–4.4 eV with respect to vacuum level) is more negative than the conduction band of TiO_2 (− 4.2 eV with respect to vacuum level). Incorporation of rGONS in the TiO_2 scaffold leads to a much more efficient device **[10, 32, 40, 44-52].** Hence rGONS are employed in this work.

The photocathode/ counter electrode (CE) is an indispensable component in DSSCs that utilise redox mediators for charge transport. It injects electrons into the electrolyte to catalyze iodine reduction (I_3^- to I^-) after charge injection from the photooxidized dye to the metal oxide semiconductor **[1, 53-60]**. The reduced species (I^-), regenerates the photooxidized dye while the oxidised species (I^-_3) is reduced at the CE. However, the inert nature of the graphene basal plane often restricts charge transfer at the graphene/liquid electrolyte interface despite the high in plane charge mobility, thus I^-_3 reduction occurs only at edge planes. As a result, surface modification of graphene is required to improve in-plane charge-transfer **[61].** In addition, for the DSSC system to work efficiently, (i) the redox species must be able to readily diffuse between the anode and the cathode, (ii) the rate of dye regeneration by I^- must be faster than regeneration from the metal oxide semiconducting scaffold, and (iii) the rate of reduction of I^-_3 must be slow at the photoanode and fast at the photocathode. In order to address requirement (iii) a catalyst material is required on the photocathode to lessen the overpotential required to reduce I^-_3, hence the use of Pt as a catalyst at the cathode **[10].** Pt has limited reserves on earth, and it is costly. It suffers degradation over time, especially when in contact with the I^-/I_3^- liquid electrolyte, and tends to induce formation of polyiodides, strongly reducing the efficiency of DSSCs. The aforementioned problems have boosted efforts towards the replacement of Pt with

cheaper and/or more stable materials **[10, 62].** In 2010, Roy-Mayhew et al. **[63]** discovered that functionalizing graphene contributes to the high catalytic activity of graphene towards I^-/I_3^- redox reaction, showing comparable performance to the Pt catalyst **[64-66].** Doping the carbon network with heteroatoms (e.g., N, B, and P) has been demonstrated to enhance the electrical conductivity and surface hydrophilicity. Doping improves charge-transfer and electrolyte–electrode interactions, respectively**.** Furthermore, heteroatom nitrogen-doped carbon nanomaterials can act as metal-free electrodes with higher electrocatalytic activities, better long-term operation stability, and more tolerance to crossover/poisoning effects relative to a platinum electrode. This has made N-doped carbon nanomaterials ideal as low-cost, but very effective, counter electrodes in DSSCs **[67- 70],** hence nitrogen doped reduced graphene oxide nanosheets (NrGONS) are studied in this thesis.

1.2.3 Characterising graphene materials

Graphene materials can be characterised using two generic methods namely microscopy and spectroscopy. In this thesis, the characteristics of the synthesised reduced graphene oxide nanosheets (rGONS) and nitrogen-doped reduced graphene oxide nanosheets (NrGONS) were investigated using transmission electron microscopy (TEM), Raman spectroscopy, X-ray diffraction (XRD) and X-ray photoelectron spectroscopy (XPS). The morphology of materials can be investigated using TEM. Raman spectroscopy is the most direct and non-destructive technique to characterise the structure and quality of carbon materials particularly to determine the defects, the ordered and disordered structures and the number of layers **[71-73].**

Table 1.1 shows graphene materials that have been used in the photoanode and photocathode for fabricating DSSCs. It can be observed from **Table 1.1** that there are no graphene materials that have been used in combination with metallophthalocyanines as dyes in fabricating DSSCs. This research work reports for the first time on the use of metallophthalocyanines dyes and graphene materials for fabricating DSSCs.

Table 1.1: Carbon nanomaterials that have been used in the photoanode and photocathode for fabricating DSSCs.

Photoanode	Photocathode	Dye	Ref.
FTO/Reduced graphene/TiO_2	Pt	cis-diisothiocyanato-bis(2,2'-bipyridyl-4,4'-dicarboxylato) ruthenium(II) bis(tetrabutylammonium), coded as N719 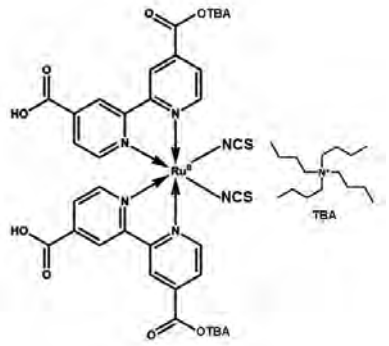	**[10]**
FTO/TiO_2/rGONS	FTO/ colloidal graphite	N719	**[12]**
FTO/graphene/TiO_2	FTO/Pt	N719	**[37]**
FTO/Graphene/TiO_2	FTO/Pt	N719	**[48]**
FTO/titania–graphene	FTO/Pt	N719	**[50]**
ITO/Reduced graphene oxide/TiO_2	ITO/Pt	N719	**[51]**
FTO/TiO_2	FTO/graphene	$Ru(dcbpy)_2(NCS)_2$ (dcbpy = 2,2-bipyridyl-4,4-dicarboxylato) dye; coded as 535-bisTBA N719	**[61]**

FTO/TiO_2	FTO/functionalised graphene sheets	Cis-bis(isothiocyanato)bis(2,2′-bipyridyl-4,4′-dicarboxylato)ruthenium(II), coded as N3	**[63]**
FTO/TiO_2	FTO/moderately reduced graphene oxide	cis-diisothiocyanato-bis(2,2'-bipyridyl-4,4'-dicarboxylic acid) ruthenium(II) coded as Ru 535	**[65]**
ITO/TiO_2	ITO/graphene oxide	N719	**[66]**
FTO/TiO_2	FTO/ N-doped Graphene, FTO/ $_r$GONS	N719	**[70]**
ITO/TiO_2/rGONS/TiO_2	ITO/Pt	D719 (Alternative name N719)	**[74]**
FTO/Graphene/TiO_2	FTO/Graphene	N719	**[75]**
FTO/Graphene/TiO_2	FTO/Pt	N719	**[76]**
FTO/Graphene oxide/TiO_2	FTO/Pt	N719	**[77]**
FTO/TiO_2	FTO/rGONS	N719	**[78]**
FTO/ TiO_2	FTO/Graphene	N719	**[79]**

FTO/TiO_2	FTO/Reduced graphene oxide (rGO)	N719	**[80]**
FTO/TiO_2	FTO/graphene	N719	**[81]**
FTO/TiO_2	FTO/3D graphene	N719	**[82]**

ITO = Indium doped tin oxide

FTO = Fluorine doped tin oxide

1.3 Metallophthalocyanines

Metallophthalocyanines (MPcs) are planar macrocyclic compounds comprising of an 18-π conjugated electron system and containing four isoindole units linked together through nitrogen atoms **Figure 1.4.** They have good optical properties, good chemical and thermal stability, absorb intensely in the red and near infra-red regions of the solar spectrum, have high extinction coefficients, are nontoxic and can easily be oxidised and reduced. Their chemical properties can easily be manipulated by structurally varying the central metal and the chemical substituents at non-peripheral (α) positions (positions 1, 4, 8, 11, 15, 18, 22, 25) and peripheral (β) positions (positions 2, 3, 9, 10, 16, 17, 23, 24) to form symmetrical or asymmetrical MPcs **[83-87]**. Owing to these properties, phthalocyanines have found applications in solar cells, optical devices, electronic/ photoelectronic components, nonlinear optics, photocatalysis, electrocatalysis, photodynamic therapy (PDT) and gas sensing among others **[83-107].**

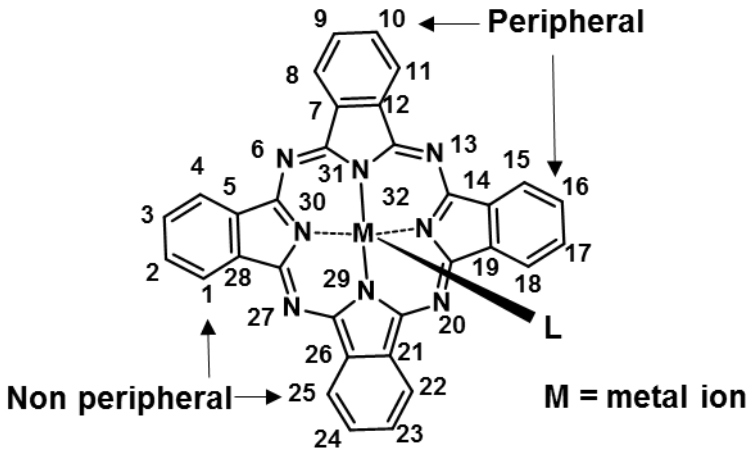

Figure 1.4: Chemical structure of phthalocyanine showing the non-peripheral (α), peripheral (β) positions and L (axial ligand on the metal ion).

Phthalocyanines (Pcs) have weak Soret band (~350 nm) and strong Q-band (~650 nm and beyond) making them good candidates as photosensitisers in DSSCs. Examples of substituents used for Pcs are: alkyl such as *tert*-butyl for good solubility in organic solvents, anionic or cationic for water solubility, alkoxy or alkylthio with electron donating capabilities **[87, 108].** Symmetrical (same functional group), asymmetrical (two different functional groups) and axially substituted Pcs were employed in this research work.

1.3.1 Synthesis of Pcs

1.3.1.1 Symmetrical

Symmetrical Pcs due to their uniform planar macrocycle, exhibit aggregation, poor solubility in common organic solvents and lack electron directionality in the excited state. This tends to limit their use in applications in DSSCs where specific binding with semiconductor molecules is required for improved efficiencies. Aggregation promotes non-radiative deactivation of the dye excited states thus reducing the power conversion efficiency **[2, 87].**

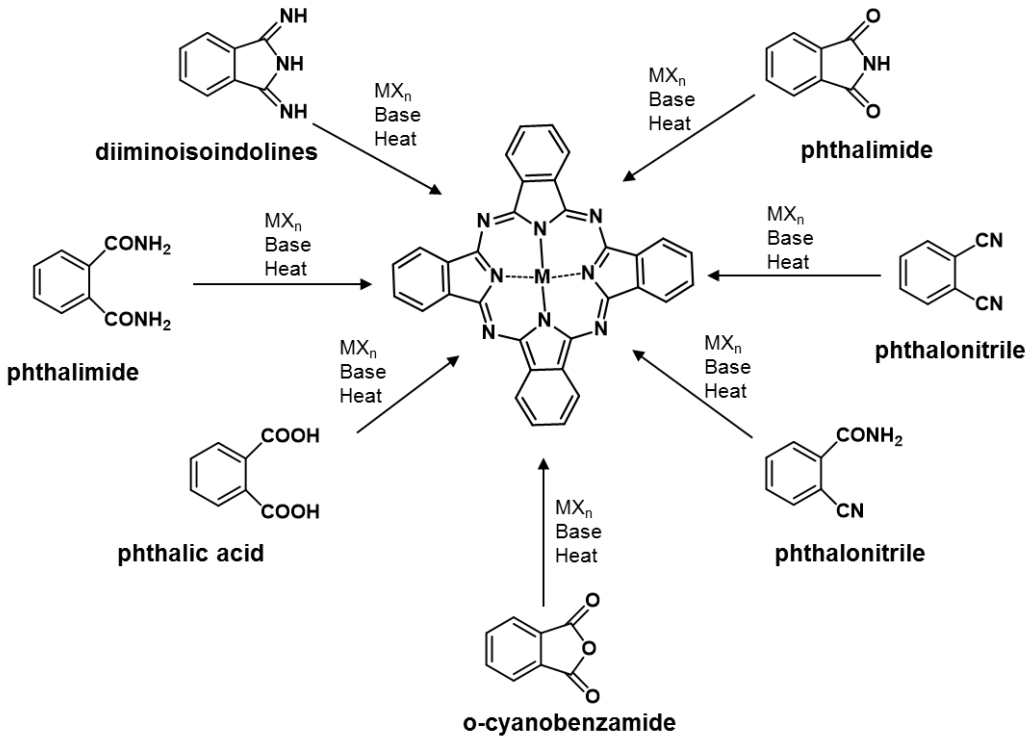

Scheme 1.1: Synthesis of phthalocyanines showing different precursors that can be used. MX = metal salt.

Synthesis of symmetrical metallophthalocyanines **(Scheme 1.1)** can be performed by using cyclotetramerization of phthalic acid derivatives (such as phthalic acid anhydride, phthalimides, o-cyanobenzamide, and 1,3-diiminoisoindolines among others), urea as nitrogen source, metal salt and a catalyst **[109-111]**). The disadvantage of this method is that some impurities remain in the product and they are difficult to remove. Using cyclo condensation of mono substituted 3-nitro phthalonitrile precursors yields non peripheral substitution while mono substituted 4-nitrophthalonitrile yields peripheral substitution **[110, 112, 113].** For applications requiring very high purity such as in solar cells, phthalonitriles (such as 1,2 dicyanobenzene) or their ammonia adducts (like the 1,3-diimino isoindolemines) bearing between one and four substituents are employed as precursors in the cyclotetramerization reaction **[86, 87, 110].**

1.3.1.2 Asymmetric

The symmetry of MPcs can be broken by placing two different functional groups on the molecule to form asymmetrical MPcs as shown in **Scheme 1.2**. Linstead and co-workers pioneered the research work on asymmetrical Pcs since 1955 **[114-116].**

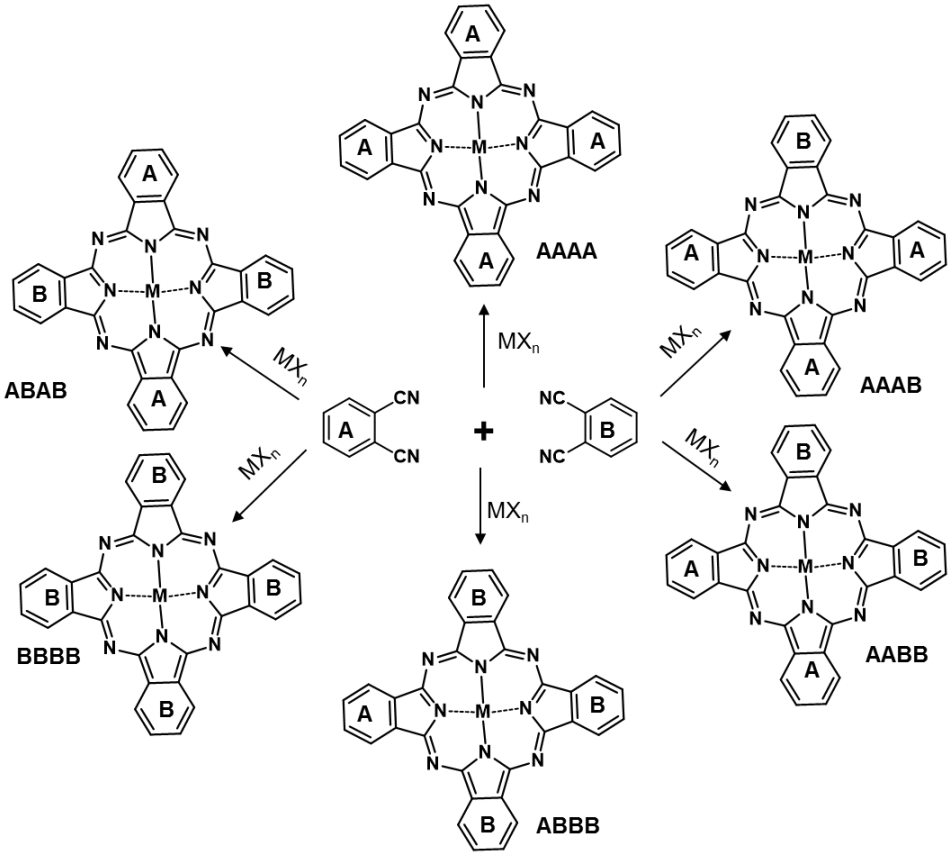

Scheme 1.2: Synthesis of asymmetrical Pcs using the statistical mixed condensation method showing anticipated products.

A variety of methods can be used to synthesise asymmetrical Pcs including statistical mixed condensation **(Scheme 1.2**), sterically driven cross condensation and polymer support-based approach. For application as photosensitisers in DSSCs, the desired Pc can be synthesised in such a way that it has an acid substituent at one of the isoindoline units for better binding with semiconductor surface. The other three isoindoline units can be functionalized with different substituents to make them more

soluble, facilitate ease of purification and hinder aggregation **[87, 116].** The statistical mixed condensation of two different phthalonitriles is the oldest and most popular for the synthesis of AAAB compounds using a ratio of the 3:1 of two precursors with similar reactivity. The method is generally non-selective and if two phthalonitriles with similar reactivity are taken in equimolar quantities all six possible products **(Scheme 1.2)** would be formed in statistical proportions (i.e. AAAA (8.33%), AAAB (25%), AABB (25%), ABAB (8.33%), ABBB (25%), and BBBB (8.33%)) **[116].** Taking into consideration the well-known aggregation properties of phthalocyanines, preparative scale separation of such reaction mixtures by conventional chromatographic methods could be very challenging. As a result, the statistical condensation approach has never been used for targeting all six possible products. On the contrary, this method is predominantly used for preparation of the AAAB asymmetric phthalocyanine analogues and, in several cases, for the preparation of opposite ABAB and adjacent AABB compounds **[116].**

In this work, the statistical mixed condensation method was used to synthesise the asymmetrical MPcs.

1.3.2 Phthalocyanine spectra

MPcs have two distinct ground state electronic absorption bands known as B band and Q band as shown in **Figure 1.5**. As stated above, the B band is usually seen around 300-400 nm and Q band around 650-700 nm depending on the nature of the central metal, point of substitution, ring expansion, protonation nature of substituents and solvents **[117-120].**

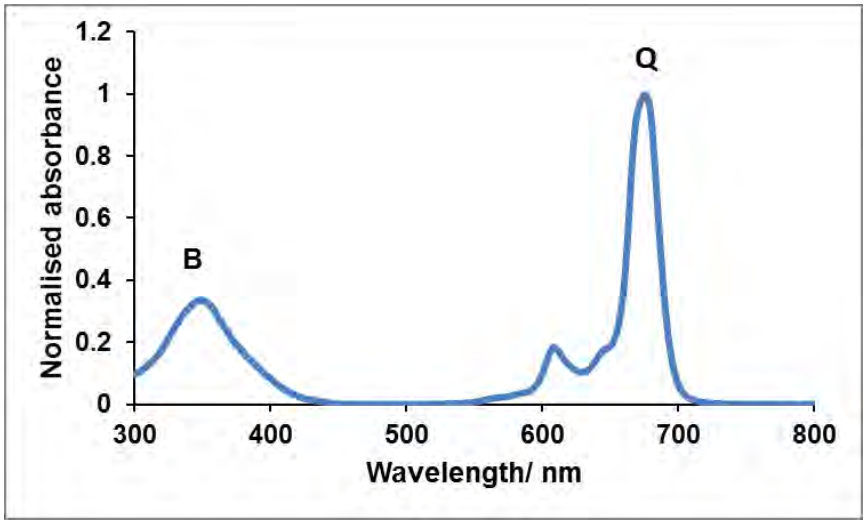

Figure 1.5: Typical ground state electronic absorption spectrum of metallophthalocyanines**.**

Gouterman and coworkers **[121, 122]** proposed a four orbital model that gives an ideal picture of electronic transitions that occur in metallophthalocyanines between the HOMO and LUMO. The symmetrical Q band is due to their D_{4h} symmetry which results from transitions from electronic transitions π (a_{1u}) of the HOMO to the degenerate π* (e_g) of the LUMO, as shown in **Figure 1.6**. Metallophthalocyanines are also characterized by two B bands, B_1 and B_2 due to two transitions, a_{2u} and b_{2u} of the HOMO to e_g of the LUMO respectively **[123, 124].** Aggregation in MPcs is judged by broadening or splitting of the Q-band **[118, 125]**.

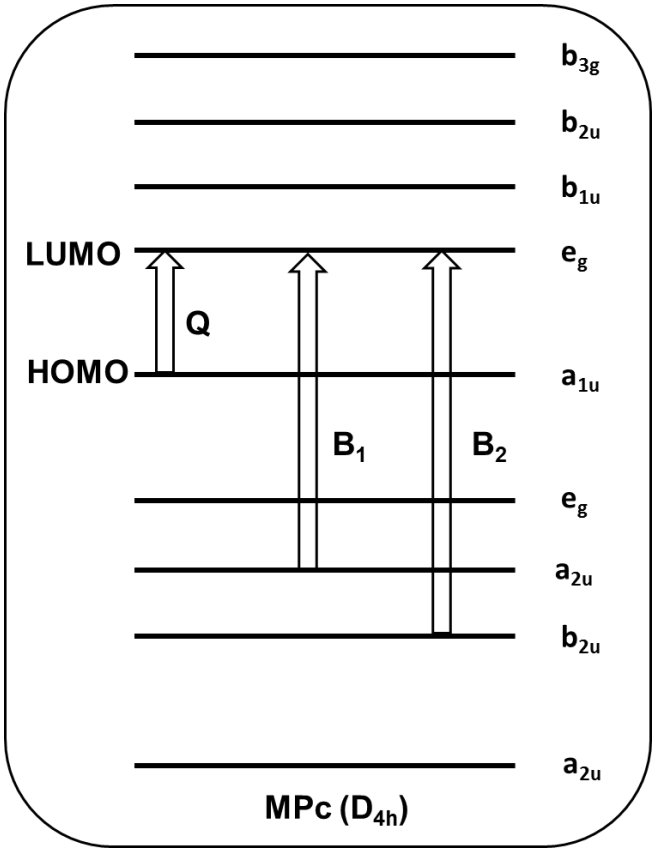

Figure 1.6: Representation for ground state electronic transitions of molecular orbitals of MPcs.

1.3.3 Electrochemical behavior

Metallophthalocyanines that are employed as sensitizers in DSSCs ideally should be easily oxidised and reduced. The redox properties of MPcs are determined by the type of central metal, axial ligands, substituents on the ring and solvents used. Substituents that are electron donating like *tert*- butyl groups, make the complex easier to oxidise and harder to reduce. Phthalocyanines with central metals that are not electroactive have their redox activity occurring at the ring. In DSSCs, in order for electronic transfer from the excited dye to the metal oxide semiconductor to be energetically favourable, the excited state energy (LUMO) of the MPc dye should be higher in energy than the conduction band of the semiconductor (ZnO or TiO_2). MPc complexes with LUMO

energies above the semiconductor conduction band edge would be best suited for DSSCs provided other factors like aggregation were addressed **[2].**

1.3.4 Application of metallophthalocyanines in dye-sensitized solar cells.

MPcs are very well-suited as sensitizers because of their good stability, high extinction coefficients and the large variety of central metal ions and chemical substituents at different positions of the ligands **[2, 5].** The carboxylate substituents on the MPcs synthesised in this work are used to anchor the dye to the metal oxide semiconductor surface and provide electronic coupling. The *tert*-butyl groups enhance solubility, minimise aggregation and tune the LUMO level of the Pc thus providing directionality in the excited state. Improved solubility leads to efficient impregnation of the photoanode from a solution of the sensitizer **[2, 5].** The electron donating capability (push) of the *tert*-butyl groups towards the central Pc ring as opposed to the electron-withdrawing character (pull) of the carboxylic acid functionality, adds push-pull characteristics to the molecular orbitals. This synergistic effect of the sensitizer is helpful for electron injection to the metal oxide semiconductor from the excited state and suppresses electron back transfer to the dye and their shuttling back to the electrolyte (recombination) **[2, 3].**

Table 1.2 shows a selection of asymmetric Pcs used for DSSCs **[5, 6, 87, 126-131].** Despite one report using an unsubstituted ZnPc -CdS/CdSe quantum dots and Au nanoparticles/graphene oxide composite in DSSCs **[131],** no investigations have been conducted on DSSCs based on MPc dyes and graphene materials on both the photoanode and photocathode, hence the aim of this work**.**

Table 1.2: Asymmetrical phthalocyanines that have been used for DSSCs

Phthalocyanine dye	Photoanode	Photocathode	Ref.
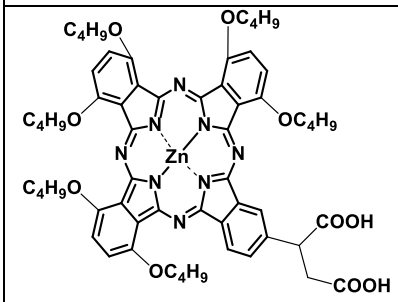	TiO_2	Pt	**[5]**
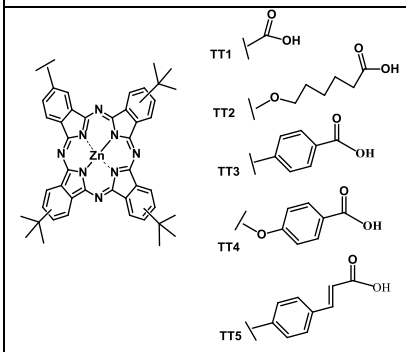	TiO_2	Pt	**[6]**
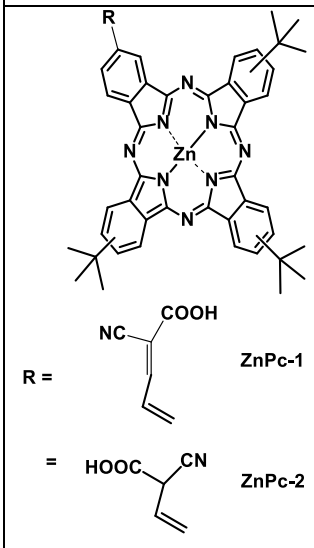	TiO_2	Pt	**[87]**

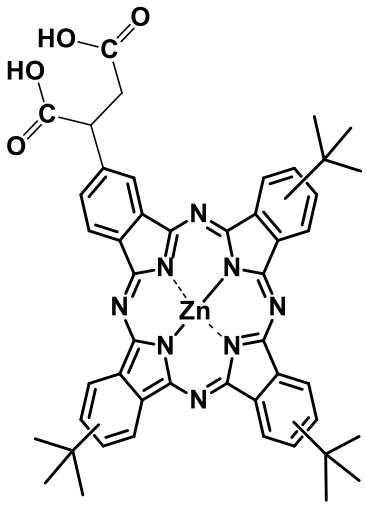	TiO_2 (solid state DSSC)	Gold (Au)	**[126]**
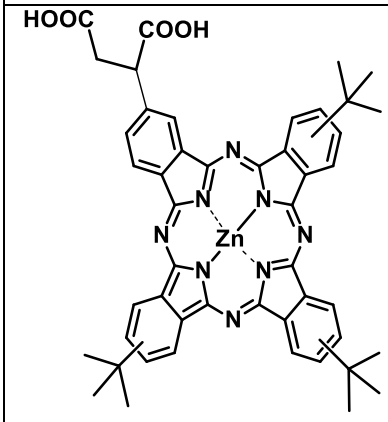	TiO_2	Pt	**[127]**
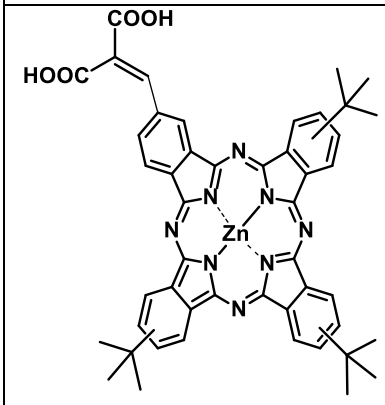	TiO_2	Pt	**[128]**

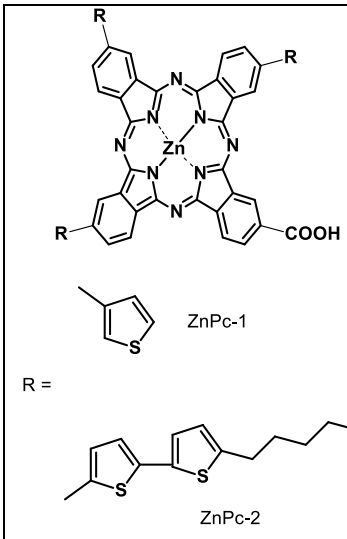	TiO_2	Pt	**[129]**
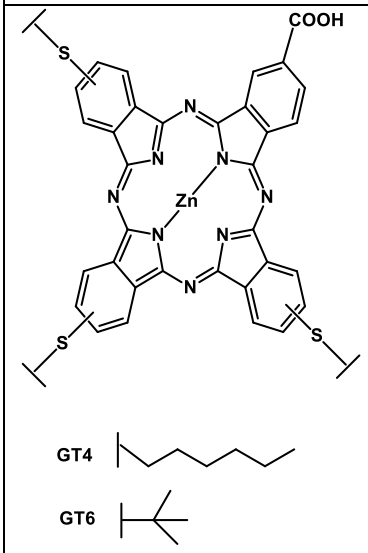	TiO_2	Pt	**[130]**
ZnPc combined with CdS/CdSe quantum dots (QDs) (co-sensitization)	ZnO inverse opals (IOs)	Copper(I) sulfide (Cu_2S) modified with Au nanoparticles/graphene oxide (Au NPs/GO) composite	**[131]**

1.3.5 Pcs used in this work

This research work reports for the first time on synthesis and characterisation of a novel axially substituted silicon phthalocyanine complex **3** and a novel asymmetrically

substituted copper phthalocyanine complex **4**, **Table 1.3**. Two reported symmetrically substituted indium phthalocyanine complexes **(1, 2)** and an asymmetrically substituted zinc phthalocyanine complex **5,** were also employed, **Table 1.3 [2, 132, 133,134].** All complexes (**1-5**) were for the first time used as dyes to fabricate DSSCs consisting of graphene materials (reduced graphene oxide (rGONS), nitrogen doped reduced graphene oxide (NrGONS)) on both the photoanode and photocathode **(Fig. 1.1)**. As earlier stated, carboxy groups on the MPcs form hydrogen bonds with hydroxide groups on the surface of the TiO_2. Graphene improves suppression of charge recombination at the photoanode/dye/electrolyte interface and also enhances electron transport in the photoanode.

Table 1.3: Phthalocyanines studied in this research work

Phthalocyanine dye	Photoanode	Photocathode
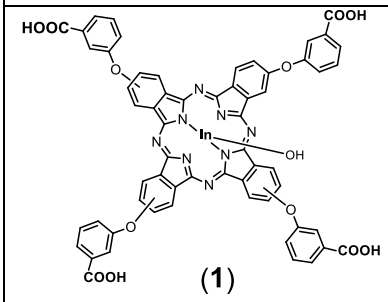 (**1**) Hydroxyl indium tetracarboxyphenoxy phthalocyanine **[134]**	ITO/TiO_2	ITO-PVP/rGONS ITO-PVP/NrGONS ITO-Pt
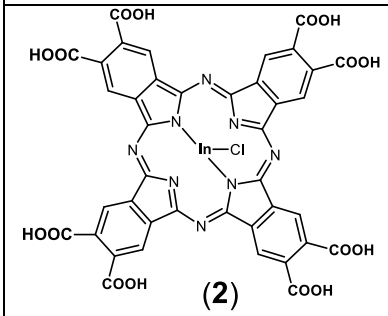 (**2**) Chloro indium octacarboxy phthalocyanine **[133]**	ITO/TiO_2	ITO-PVP/rGONS ITO-PVP/NrGONS ITO-Pt
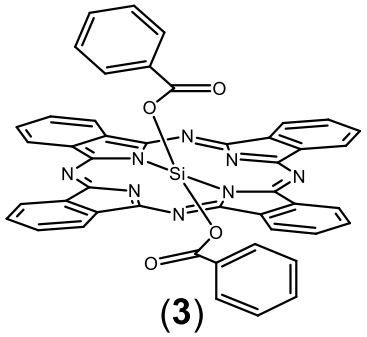 (**3**) Dibenzoic acid silicon phthalocyanine **[New Pc]**	ITO/rGONS/TiO_2	ITO-PVP/rGONS ITO-PVP/NrGONS ITO-Pt

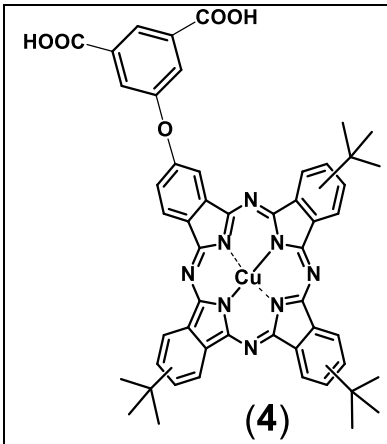 (**4**) 2(3,5-biscarboxyphenoxy), 9(10), 16(17), 23(24)-tri(tertbutyl) phthalocyaninato Cu (II) **[New Pc]**	All done with rGONS and NrGONS	ITO/NrGONS
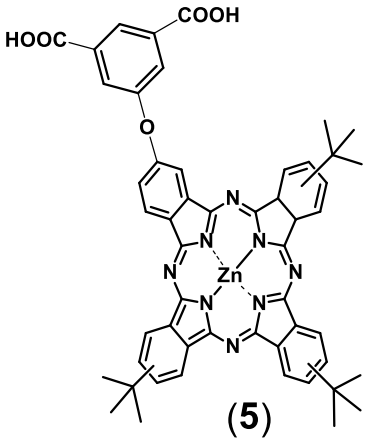 (**5**) 2-[5-(phenoxy)-isophthalic acid] 9(10), 16(17), 23(24)-tris (tertbutyl) phthalocyaninato Zinc (II) **[132]**	All done with rGONS and NrGONS	ITO/NrGONS

ITO = Indium doped tin oxide, rGONS = Reduced graphene oxide, NrGONS = Nitrogen doped reduced graphene oxide, PVP = Polyvinyl pyrrolidone

i. Complexes (**1**) and (**2**) are compared for the effect of the substituent

ii. Complex (**3**) for axial ligation

iii. Complexes (**4**) and (**5**) are compared for the effect of the central metal

1.4 Evaluation of dye-sensitized solar cells

Performance of dye-sensitized solar cells is evaluated using current density vs voltage curves (J-V) **(Fig. 1.7)** and electrochemical impedance spectroscopy (EIS). From the resultant J-V measurements, the fill factor (FF) and power conversion efficiency η, are evaluated as shown in **Eqs. (1.1)** and **(1.2) [10, 135, 136].**

$$FF\ (\%) = \frac{P_{max}}{J_{sc}\ x\ V_{oc}} x\ 100 \qquad \textbf{(1.1)}$$

$$\eta(\%) = \frac{J_{sc}\ x\ V_{oc}\ x\ FF}{I_o}\ x\ 100 \qquad \textbf{(1.2)}$$

where, P_{max}, J_{sc}, V_{oc} and I_0 are the maximum power output, short circuit photocurrent density, open circuit photovoltage and intensity of incident light respectively. FF is a measure of the squareness of the J–V curve of a solar cell and determines the maximum power from a solar cell. Power conversion efficiency (η %) shows how well the solar cell converts light into electricity.

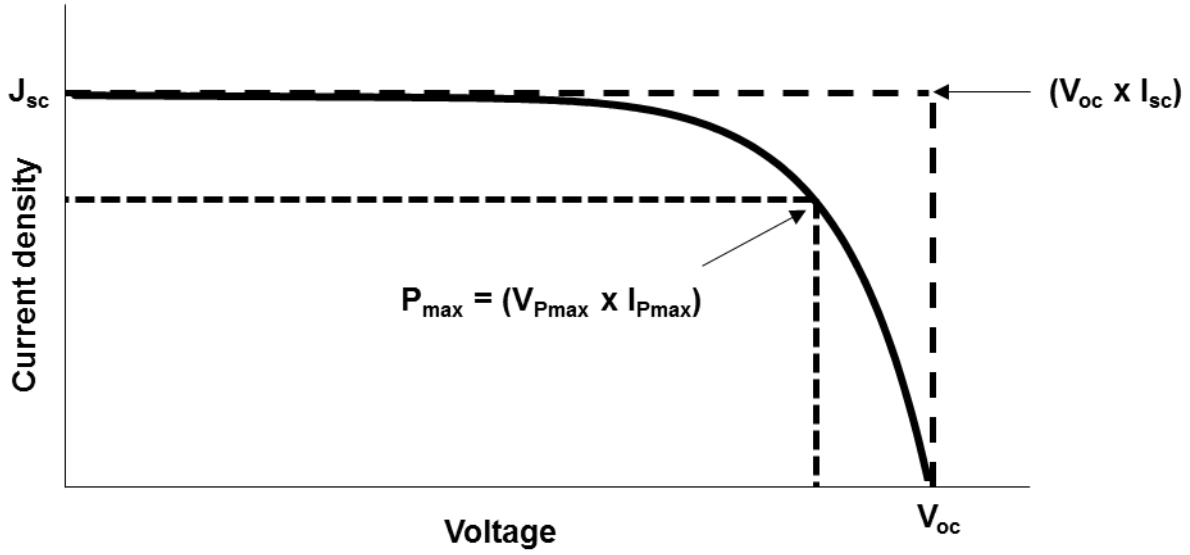

Figure 1.7: Current density versus voltage curves (J-V curves) showing parameters used for calculating fill factor (FF, %) and power conversion efficiency (η, %).

Electrochemical impedance spectroscopy (EIS) is used to investigate the interfacial characteristics of the components of a dye-sensitized solar cell in order to gain more insight into the electron transport. EIS experiments are usually carried out in the frequency range 0.10 Hz to 100 kHz with an AC amplitude of 0.010 V. The bias potential is mostly set to a value equivalent to the open circuit voltage of the DSSC. From EIS data, Nyquist and Bode phase plots are generated **[137].** The Nyquist plot represents the impedance as a vector of length |Z|, where the real part is plotted on the x-axis and the imaginary part is plotted on the y-axis (**Fig. 1.8**). Their one major shortcoming is that when you look at any data point on the plot, you cannot tell the frequency that was used to record it **[137].** The interpretation of the Nyquist plots can be modelled by an equivalent circuit (Randles circuit) comprising of, for example, solution/electrolyte resistance (R_s), charge transfer resistance (R_{ct}), Warburg impedance (W), double layer capacitance (C_{dl}) and constant phase element (Q/ CPE).

Figure 1.8 (insert) is an example of an equivalent circuit showing some of the circuit elements. The Warburg impedance (W), is a complex quantity having real and imaginary parts which are equal and is proportional to the reciprocal of the square root of the frequency ($1/\sqrt{\omega}$). Thus, at high frequencies, W is small and the diffusion process is only observed at low frequencies **[137].**

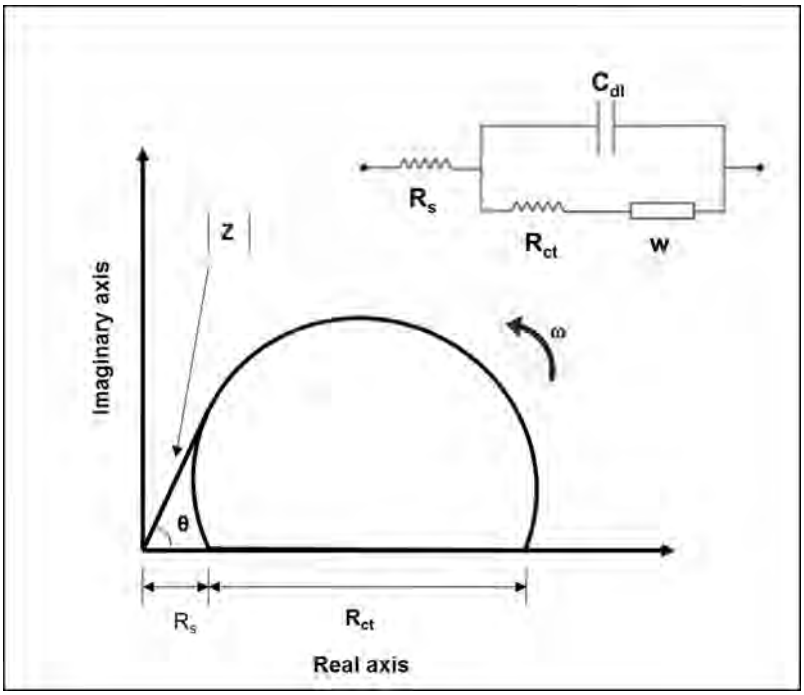

Figure 1.8. Nyquist plot representing Impedance as a vector Z (Argand diagram). ω is angular frequency. Insert is the Randles-Sevcik equivalent circuit.

C_{dl} is sometimes modelled with a constant phase element (CPE) for better accuracy. The impedance of CPE can be expressed as in **equation 1.3**

$$Z_{CPE}\,(j\omega) = \frac{1}{Q.(j\omega)^{\alpha}} \qquad \textbf{(1.3)}$$

where Q represents the double-layer capacitance/constant phase element, ω is the angular frequency while the parameter α accounts for the non-ideal electrode–electrolyte interface (the case α = 1 refers to an ideal capacitance)**.**

Three semi circles are usually observed on the Nyquist plots for DSSCs. In order of decreasing frequency (left to right), these semi circles can be attributed to the impedance contribution from: solution/electrolyte resistance of transport through the current collector (R_s), the charge transfer resistance (R_{ct}) at the counter electrode/electrolyte interface, charge transfer resistance at the photoanode/dye/electrolyte interface and diffusion of redox species in the electrolyte solution, respectively. The semicircle in the middle frequency region is the result of contributions from the electron transfer resistance and interfacial capacitance at the photoanode/dye/electrolyte interface. Generally, the low frequency region provides information concerning diffusion phenomena. The high frequency part defines the solution resistance **[137-139].** The smaller the middle semicircle diameter is, the lower the R_{ct} and thus the higher the conductance of the photoanode/dye/electrolyte interface (meaning the interface is an excellent conducting material to accelerate electron transport).

Another popular presentation method is the Bode Plot, in which the impedance is plotted with log frequency on the x-axis and both the absolute values of the impedance ($|Z|=Z_0$) and the phase-shift on the y-axis. Unlike the Nyquist Plot, the Bode Plot does show frequency information **[137].**

1.5 Summary of aims of this thesis

The aims of this thesis include:

I. Synthesis and characterisation of reduced graphene oxide nanosheets (rGONS).

II. Synthesis and characterisation of nitrogen-doped reduced graphene oxide nanosheets (NrGONS).

III. Synthesis and characterisation of axially substituted silicon phthalocyanine.

IV. Synthesis and characterisation of symmetrical and asymmetrical metallophthalocyanines.

V. Fabrication of dye-sensitized solar cells (DSSCs) based on rGONS and NrGONS in both the photoanode and photocathode, photosensitised by axially substituted metallophthalocyanines, symmetrical and asymmetrical metallophthalocyanines.

VI. Evaluation of the performance of the different DSSCs, using photocurrent - photovoltage (J-V) measurements and electrochemical impedance spectroscopy (EIS).

VII. Comparison of the performance of rGONS, NrGONS and platinum (Pt) as catalysts at the DSSC photocathode, with aim of replacing expensive and rare Pt.

Chapter 2: Experimental

2.1 Materials

Indium doped tin oxide (ITO) glass substrates 1 mm thick, titanium dioxide (TiO_2), titanium (IV) tetraisopropoxide, lithium iodide, ferric nitrate, polyvinyl pyrrolidone (PVP), dichloro silicon phthalocyanine, benzoic acid, chloroplatinic acid hydrate, tetrabutylammonium tetrafluoroborate ($TBABF_4$), melamine, 1,8-diazobicylo[5.4.0]undec-7-ene (DBU), 1-pentanol and 4-(*tert*-butyl) phthalonitrile **(6)** were purchased from Sigma Aldrich. Acetone, ethanol, acetonitrile, iodine, tetrahydrofuran (THF), dimethyl formamide (DMF), ethylene glycol, silica gel, 2-propanol and 1-octanol were from Merck. Parafilm plastic film was from Bemis. Copper foil was from the British Drug House Limited. Binder clips were from ABM Office National (2 pieces for 1 cell). Copper acetate monohydrate ($Cu(OAc)_2.H_2O$) and dichloromethane (DCM) were purchased from SAARChem. NaOH was obtained from B&M scientific. Methanol and HCl were purchased from Minema. Complexes (**1**) **[134],** (**2**) **[133]**, (**5**) **[132]** and dimethyl-5-(3,4-dicyanophenoxy)-isophthalate (**7**) **[140]** were synthesized as reported in literature.

2.2 Equipment

1. Mass spectra data were collected using a Bruker AutoFLEX III Smartbeam TOF/TOF Mass spectrometer. The mass spectra were obtained using alpha-cyano-4-hydroxycinnamic acid as the MALDI matrix and a 354 nm nitrogen laser.
2. UV-Vis absorption spectra in solution were performed on a Shimadzu® UV-2550 spectrophotometer.
3. Solid state UV-Vis absorption spectral studies were performed on Perkin Elmer Lambda 950 UV-Vis-NIR spectrophotometer where reflectance measurements

were converted into equivalent absorption spectra using the reflectance of holmium as a reference.

4. FT-IR spectra were acquired on a Bruker ALPHA FT-IR or Perkin Elmer spectrometer with universal attenuated total reflectance (ATR) sampling accessory.
5. Elemental composition data (C, H, N) for complexes (**3**) and (**4**) were acquired on a Vario Microcube EL III Elemental CHNS Analyser.
6. Proton nuclear magnetic resonance (^{1}H NMR) spectra of complex (**3)** and (**4**) were obtained using a Bruker AVANCE 600 MHz NMR spectrometer in DMSO-d_6.
7. X-ray photoelectron spectroscopy data were collected from a Kratos Axis Ultra DLD X-ray photoelectron spectrometer (XPS), using an Al (monochromatic) anode, equipped with charge neutralizer and the operating pressure kept below 5 x 10^{-9} Torr. For wide/survey XPS scans, the following parameters were used: emission current was kept at 5 mA and the anode voltage at 15 kV. The resolution used to acquire wide/survey scans was at 160 eV pass energy using a hybrid lens in the slot mode. For high resolution scans, the resolution was changed to 40 eV pass energy in the slot mode. Curve fitting was performed using Gaussian-Lorentzian peak shape after performing a linear background correction.
8. X-ray diffraction spectra for the graphene materials (rGONS and NrGONS) were recorded on a Bruker D8 Discover X-ray powder diffractometer (XRD) equipped with a LynxEye detector, under Cu-Kα radiation (λ= 1.5405 Å, nickel filter). Data were collected in the range from 2θ = 10 ° to 60 ° with a scanning rate of 0.010 ° min^{-1}, 192 s per step and a slit width of 6.0 mm. Samples were placed on a zero background silicon wafer slide. The data were processed using EVA (evaluation curve fitting) software after performing baseline corrections.

9. The morphologies of the graphene materials (rGONS and NrGONS) were obtained from a Zeiss Libra 120 model transmission electron microscope (TEM) operated at 90kV.

10. Raman spectra for the graphene materials (rGONS and NrGONS) were obtained using a Bruker Vertex 70 - Ram II spectrometer (equipped with a 1064 nm Nd:YAG laser and a liquid nitrogen cooled germanium detector).

11. Photocathode catalyst materials (rGONS or NrGONS) were spin coated onto ITO using a Specialty coating systems 6800 spin coater.

12. The metal oxide semiconductor materials (TiO_2, TiO_2/rGONS or TiO_2/NrGONS) were deposited onto ITO to fabricate the photoanodes, using two methods (**A** and **B**). In method **A**, the metal oxide semiconductor materials were deposited onto ITO using the doctor blade technique. For method **B**, the metal oxide semiconductor materials were screen printed onto ITO to fabricate the photoanodes using a Dyenamo DN-HM02 Laboratory screen-printer (**Scheme 2.1**).

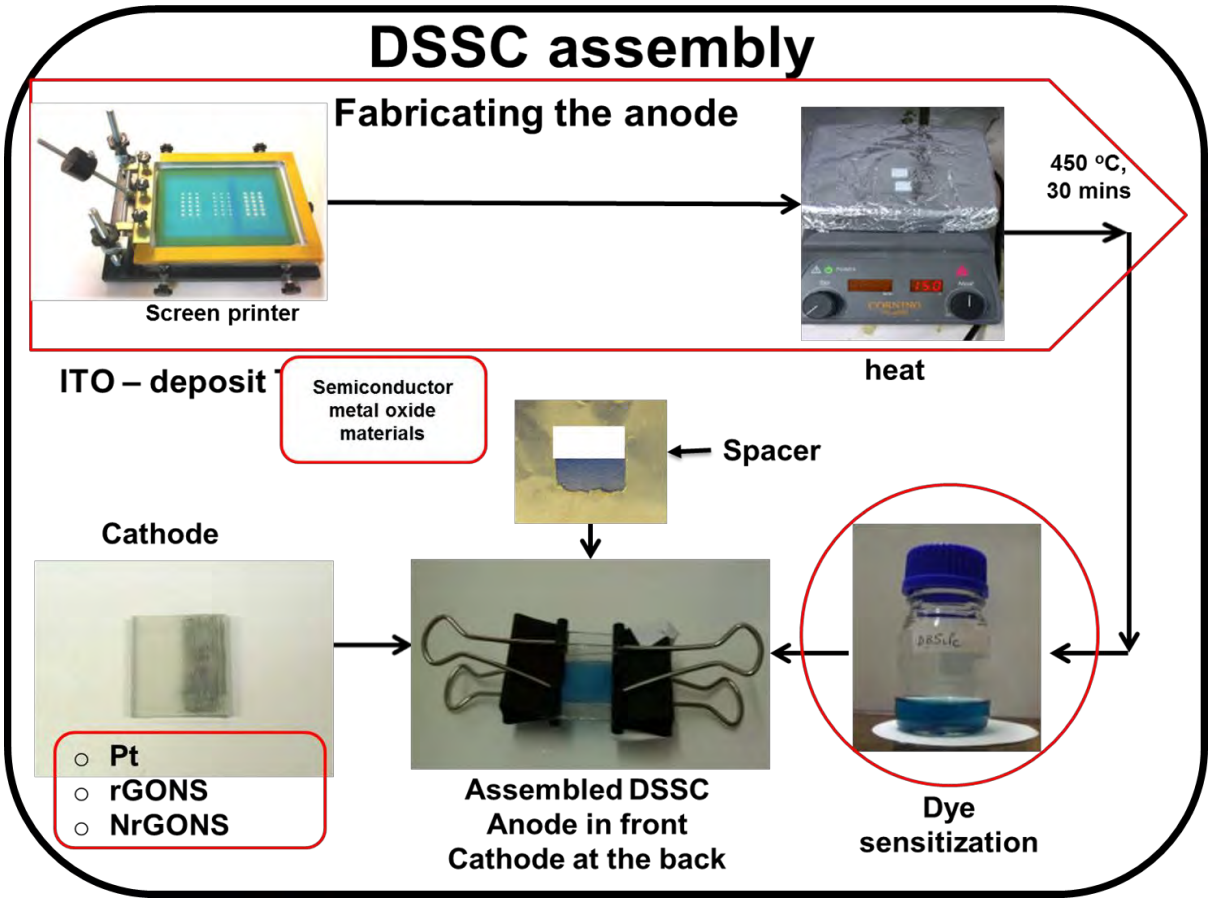

Scheme 2.1: Fabrication of dye-sensitised solar cells (DSSCs)

13. Photoanode thickness measurements were obtained using a JOEL JSM 840 scanning electron microscope (SEM) or Olympus DP72 stereo microscope equipped with stream motion software.

14. Atomic force microscopy (AFM) measurements in tapping mode were carried out using the MFP-3D Origin supplied by Asylum research (Oxford instruments company, USA).

15. Time-of-Flight Secondary Ion Mass Spectrometer (TOF-SIMS) data for the photoanodes was recorded with ION TOF GmbH TOF SIMS 5 instrument, run in imaging mode. The analysis area was 250 μm x 250 μm, and the samples were run in both positive and negative ion modes. The analyzer was set to a standard operating mode with a cycle time of 100 μs, whilst the primary beam was a Bi1 ion

cluster gun with a current of 0.13 pA and an energy of 30000 eV. The raw data was processed using the Surface Lab 6.5 software provided by ION TOF.

16. Evaluation of the dye-sensitized solar cells was done by current–voltage (J–V) and Electrochemical Impedance Spectroscopy (EIS) measurements using a Metrohm Autolab Potentiostat/Galvanostat 302 N with FRA Module and LED kit for Photovoltaic measurements (equipped with Nova 2.1.4 software) (**Fig. 2.1**). The experiments were carried out in the frequency range 0.10 Hz to 100 kHz with an AC amplitude of 0.010 V. The bias potential was set to a value equivalent to the open circuit voltage of the DSSC.

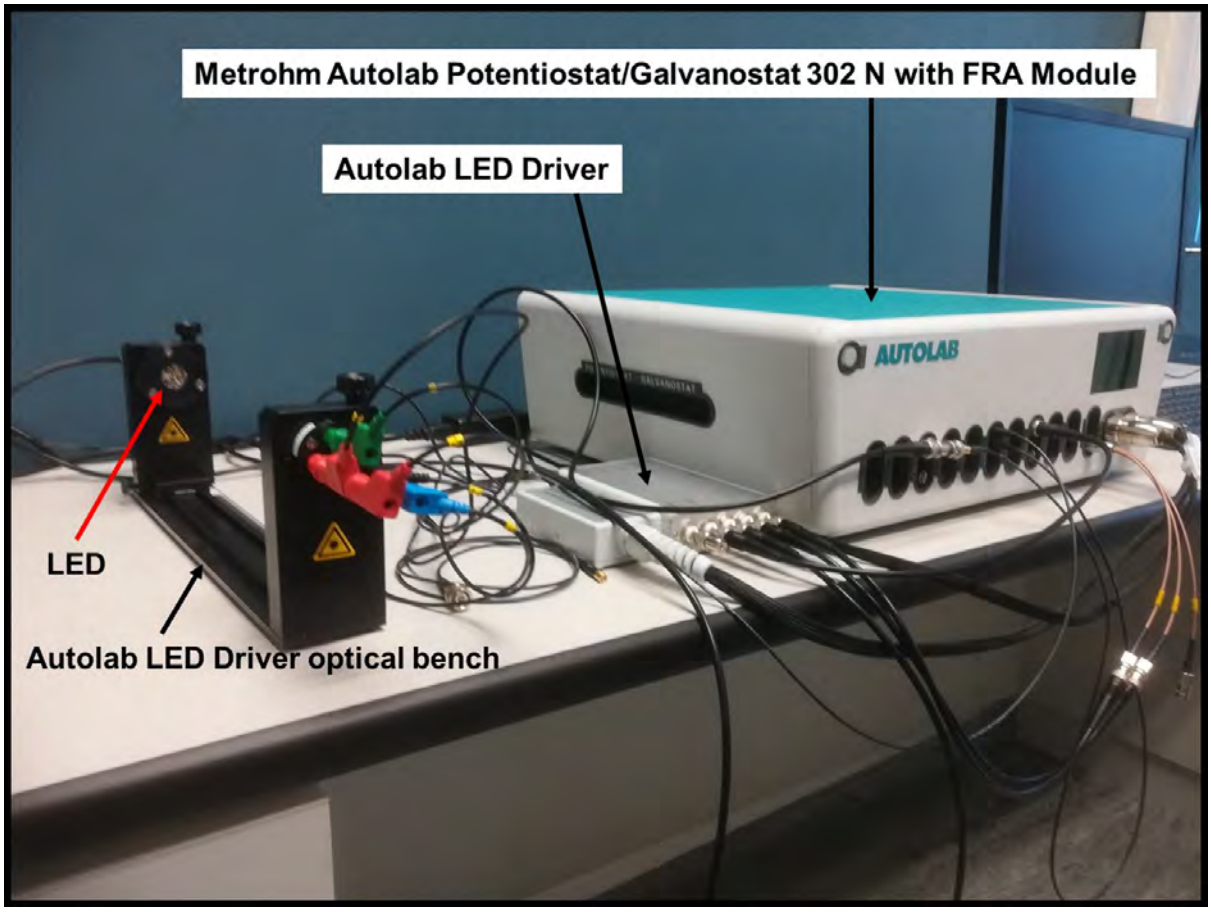

Figure 2.1: Evaluation of the dye-sensitized solar cells using a Metrohm Autolab Potentiostat/Galvanostat 302 N with FRA Module and LED kit.

Evaluation of the dye-sensitized solar cells was also done by current density – voltage (J–V) measurements using home assembled equipment based on a thermo oriel model 66902 Xenon lamp (**Fig. 2.2**) at illumination intensity of 100 $mW.cm^{-2}$. The light intensity was measured using the Field max II power meter. The light intensity was then used to calculate the power conversion efficiency. The solar cell output voltage and current were measured using Fluke 179 digital multimeter and a TTi 1906 high-resolution computing multimeter. The solar cell output was then recorded with different resistors connected as load from 1 MΩ resistor to 56 Ω until the voltage was zero. The light intensity and the recorded voltages and currents were then used to calculate the power conversion efficiency.

The home assembled equipment in **Fig. 2.2** was used to evaluate DSSCs fabricated using method **A**, based on complexes (**1-3**) before the more automated equipment in **Fig. 2.1** arrived. The equipment in **Fig. 2.1** was used to evaluate DSSCs fabricated using method **B**, based on complexes (**4**) and (**5**)**.**

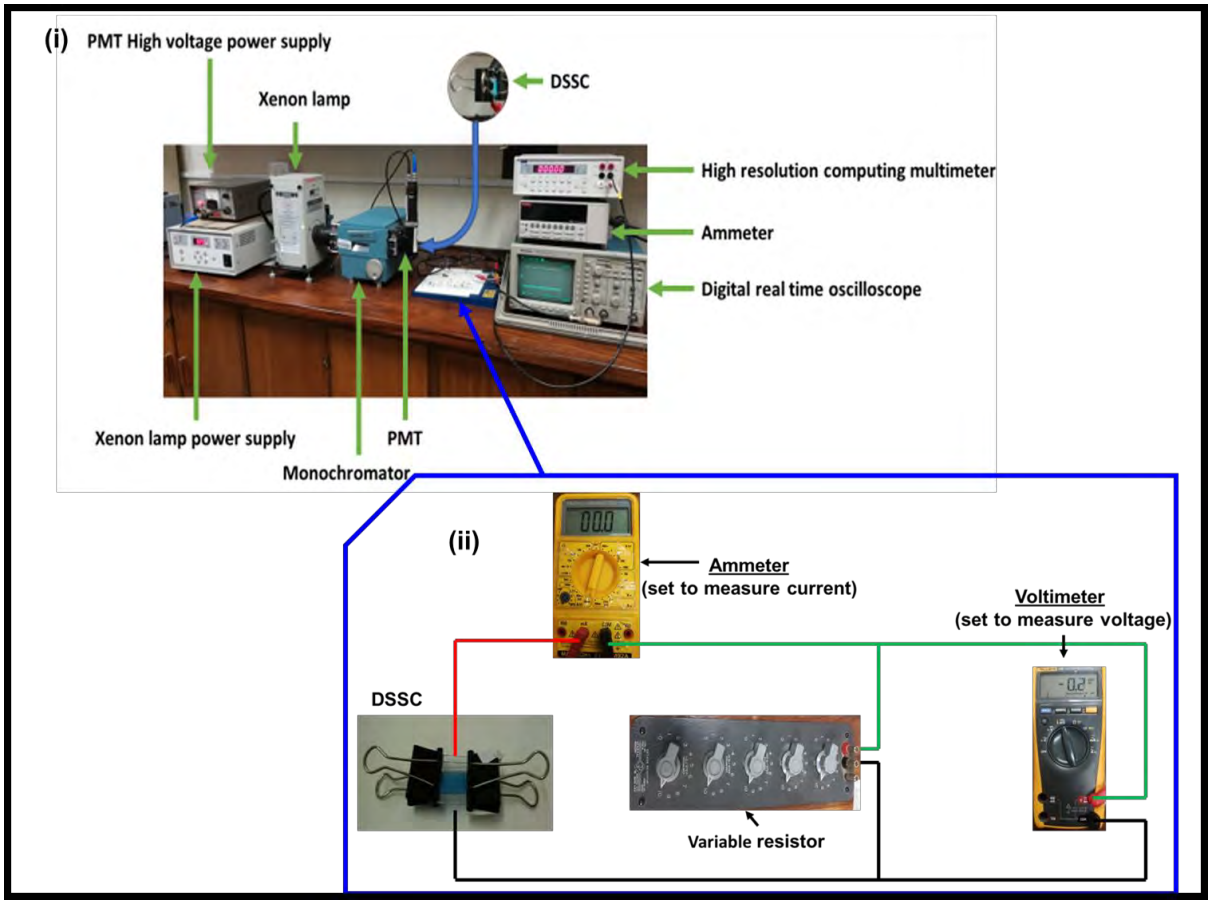

Figure 2.2: Evaluation of the dye-sensitized solar cells by current density – voltage (J–V) measurements using the thermo oriel model 66902 Xenon lamp (home assembled equipment setup) **(i)** Equipment layout **(ii)** Circuit diagram for current and voltage measurements.

17. Differential pulse voltammetry (DPV) experiments were performed using Autolab PGSTAT30 electrochemical workstation (equipped with GPES software version 4.9). The electrochemical characterization of phthalocyanines were performed in 0.050 M DMF solutions containing 0.10 M $TBABF_4$. A three-electrode electrochemical cell consisting of a glassy carbon electrode (GCE) working electrode, Ag wire pseudo-reference electrode and platinum wire as counter electrode was employed. For comparison, all electrochemical measurements

were conducted in the presence of ferrocene/ferrocenium (Fc/Fc^+) redox couple as an internal reference **[141]**.

2.3 Synthesis

2.3.1 Dibenzoic acid silicon phthalocyanine, complex (3), Scheme 3.1

Complex (**3**) was synthesised following literature methods **[142]**. A mixture of dichlorosilicon phthalocyanine (100 mg, 0.16 mmol) and benzoic acid (60 mg, 0.49 mmol) in 3 mL of 1-octanol was refluxed under nitrogen for 72 h. The product was then purified using column chromatography on silica gel and THF as the mobile phase, to obtain complex **3**, which was then dried in a fume hood.

Yield: (8%) UV/Vis (DMF): λ_{max} nm (log ε) 355 (4.75), 604 (4.49), 640 (4.49), 671 (5.28). ^{1}H NMR (600 MHz, d_6-DMSO) δ 9.64 (d, *J* = 7.3 Hz, 4H), 8.89 (m, 6H), 8.44 (d, J = 9.6 Hz, 4H), 7.78 (m, 6H), 6.74 (m, 6H). Calc. for $C_{46}H_{26}N_8O_4Si.H_2O$.: C = 68.99, H = 3.52, N = 13.99, Found: C = 69.48, H = 4.496, N = 12.94. MALDI-TOF-MS *m/z* calc: 782.84. Found $[M\text{-}Cl]^+$ 782.94.

2.3.2 Asymmetric copper phthalocyanine, complex (4), Scheme 3.2

The synthesis of complex (**5**) was reported before **[132]** and the same experimental procedure was used for the synthesis of complex **4** as shown in **Scheme 3.2**. In brief, 4-(*tert*-butyl) phthalonitrile (**6**, 383 mg, 2.08 mmol) and dimethyl-5-(3,4-dicyanophenoxy)-isophthalate (**7**, 100 mg, 0.30 mmol) were reacted with copper acetate monohydrate, $Cu(OAc)_2.H_2O$ (38.0 mg, 0.19 mmol) in the presence of catalytic DBU (30 mL) in 1-pentanol (5.0 mL). The reaction mixture was stirred and heated to 200 ^{o}C with reflux under argon. After 8 h the reaction was cooled to room temperature. The product was precipitated and subsequently washed with methanol. The precipitate

was purified using silica gel column chromatography and elution with DCM/methanol (9:1), to isolate complex **8**, 2-[dimethyl 5-(phenoxy)-isophthalate)] 9(10), 16(17), 23(24)-tris (*tert*-butyl) phthalocyaninato Cu (II). Complex **8** was then hydrolysed by dissolving 0.107 g (0.11 mmol) in THF (5.0 mL) followed by addition of 5.0 mL of 5.0 M NaOH. The resulting reaction mixture was stirred for 48 h at 80 ^{o}C under reflux. THF was then evaporated from the reaction mixture and dilute HCl was added to precipitate out complex (**4**).

Yield = 24%. FT-IR (U_{max}/cm^{-1}): 1336 (C-N), 1537 (C=N), 1685 (C=O), 2950 (C-H), 3400 (O-H). UV-vis (DMF): λ_{max} nm (log ε) 349 (4.13), 608 (3.92), 676 (4.40). ^{1}H NMR (600 MHz, DMSO_d_6) δ 8.10 (s, 2H, COO-H), 7.72 (s, 12H, Ar-H), 6.64 (s, 3H, Ar-H), 2.66 (s, 9H, CH_3-C(CH_3)$_2$), 2.27 (s, 9H, CH_3-C(CH_3)$_2$), 1.41 (s, 9H, CH_3-C(CH_3)$_2$). $C_{52}H_{44}N_80_5$ Calc. for (%): C = 67.56, H = 4.80, N = 12.12, Found (%): C = 66.33, H = 4.45, N = 11.87. MALDI-TOF-MS *m/z* calc: 923.27. Found $[M-Cl]^+$ 923.35.

2.3.3 Reduced graphene oxide nanosheets (rGONS)

Graphene nanosheets were synthesised according to literature methods **[36]**, with minor modifications. Acetylene gas and Cu foil served as carbon precursor and catalyst respectively. The copper foil was cleaned by an ultrasonic cleaner for approximately 15 min in ethanol followed by 15 min in acetone before being heated in a tube furnace to 650 ^{o}C at a rate of 10 ^{o}C/min and then annealed for 20 min while purging with Ar and H_2. To grow the graphene, acetylene gas was then turned on, while maintaining the temperature (650 ^{o}C) and a total Ar/H_2 flow rate of 1000 standard cubic centimetres per minute (sccm). After a growth time of 10 min, the furnace was allowed to cool down to room temperature under the same Ar/H_2 environment. The Cu foil with the as grown graphene was etched out in an ultrasonic cleaner with the

etchant [ferric nitrate (1g, 4.13 mmol) and hydrochloric acid (1 mL, 10.2 mmol) in deionized water (25 mL)]. Thermal annealing can eliminate oxygen functional groups on GO to produce reduced graphene oxide nanosheets **[143]**, hence the method employed in this work results in the formation of rGONS.

2.3.4 Nitrogen doped reduced graphene oxide nanosheets (NrGONS)

Catalyst free synthesis of nitrogen-doped graphene oxide (NrGONS) via thermal annealing was carried out according to literature methods **[73]** with minor modifications. The rGONS prepared above and melamine were mixed together in a mass ratio of 1:5 by grinding, forming a uniform grey mixture. The grey mixture was then heated in a tube furnace in an argon environment to 250 °C. The temperature was maintained at 250 °C for 40 min followed by 550 °C for 40 min and finally at 1000 °C for 1 h. The furnace was allowed to cool down to room temperature, to give NrGONS. The NrGONS were washed with copious amounts of water using ultrasonication and centrifugations.

2.3.5 Fabrication of the DSSCs, Scheme 2.1

The DSSCs were fabricated according to the literature methods **[135, 144]** with minor modifications. In brief, two indium tin oxide (ITO) glass substrates were cut into 20 mm x 20 mm dimensions. One ITO glass substrate was used as the photoanode and the other as the counter electrode or photocathode.

The preparation of TiO_2 paste: 3.5 g of TiO_2 nano-powder was suspended in ethanol (15 mL), followed by sonication for 30 min. About 0.5 mL of titanium (IV) tetraisopropoxide (used as a binder for TiO_2 paste) was added and the mixture stirred until the suspension was uniform. The TiO_2-rGONS paste was prepared by dispersing

0.05 g of rGONS in 30 mL of ethylene glycol and sonicating for 4 h. The rGONS containing solution was then separately mixed with TiO_2 paste and stirred for 4 h.

Two sets of dye-sensitized solar cells (DSSCs) were fabricated. For method **A**: The doctor blade technique was used to fabricate the photoanode by placing Scotch tape on the conducting side of ITO glass (20 mm x 20 mm), living approximately 10 mm in the middle and then securing it onto a table. TiO_2 paste with or without rGONS was then deposited onto the exposed part of ITO glass and flattened with a razor blade/ glass rod. The paste was left to dry in air, after which the scotch tape was removed. The photoanode was then heated at 150 °C and 450 °C for 10 min and 30 min, respectively. Pc dyes (**1**), (**2**) and (**3**) were dissolved in DMF to make a 0.5 mM solution. The heated photoanodes were then immersed into the solution of each Pc for 12 h followed by rinsing with DMF. The photoanode studies are represented as ITO-TiO_2-(**1**) for complex (**1**), ITO-TiO_2-(**2**) for complex (**2**), ITO-TiO_2-(**3**) for complex (**3**) and ITO-TiO_2-rGONS-(**3**) for rGONS and complex (**3**). Please note rGONS was also employed with complex (**3**) at the photoanode as an example, using the doctor blade technique (method **A)**. Counter electrodes/photocathodes containing rGONS or NrGONS were fabricated according to literature methods **[135, 145]** with minor modifications. In brief, rGONS or NrGONS (0.05 g) were suspended in a mixture of water and ethylene glycol (20 mL each). The mixtures were sonicated for 2 h. Following this, PVP (2 g) was added and mixture stirred for a further 5 h at 80 °C. The rGONS or NrGONS suspensions were then spin coated onto ITO at 6000 rpm for 30 s. For comparison, platinum was also used as catalyst on the counter electrode (CE). To fabricate the Pt counter electrode, 100 µL of 5 mM chloroplatinic acid hydrate in 2-propanol was placed on ITO glass substrate. The substrate was then heated up to

350-400 °C for 1 h **[135, 145].** The counter electrodes in method **A** are represented as ITO-PVP/NrGONS, ITO-PVP/rGONS and ITO-Pt.

To make a spacer (between the photoanode and counter electrode), a 1 cm x 0.6 cm hole was cut on a parafilm plastic sheet of dimensions 1.5 cm (width) by 2 cm (length). Liquid electrolyte was formed by using 0.5 M lithium iodide and 0.05 M iodine in acetonitrile. To fabricate the DSSC, a spacer was then placed on the photoanode and 3 drops of the electrolyte added via the hole. The photoanode and the counter electrode were combined facing each other, and then fixed with binder clips. This was done quickly to prevent the solvent (acetonitrile) from drying out.

In method **B**, TiO_2/rGONS paste was screen printed onto ITO substrate to form ITO-TiO_2/rGONS photoanode. Due to the success of ITO-TiO_2/rGONS-(**3**) photoanode in method **A**, in method **B**, photoanodes with TiO_2 alone (without GONS) were not fabricated. The photoanode was then heated at 150 °C and 450 °C for 10 min and 30 min respectively. To make the dye photosensitizer, 50 μM of each complex (**4** and **5** separately) were dissolved in ethanol. The ITO-TIO_2/rGONS photoanodes were then separately immersed in solutions of complex (**4**) and (**5**) for 12 h followed by rinsing with ethanol. The photoanodes are represented as ITO-TiO_2/rGONS-(**4**) for complex (**4**) and ITO-TiO_2/rGONS-(**5**) for complex (**5**). Photoanodes where NrGONS was used instead of rGONS were also prepared. The full list of the photoanodes prepared using method **B** is: ITO-TiO_2/rGONS-(**4**), ITO-TiO_2/NrGONS-(**4**), ITO-TiO_2/rGONS-(**5**), and ITO-TiO_2/NrGONS-(**5**). The counter electrode containing NrGONS as electrocatalyst was fabricated using the same procedure as in method **A** [**135, 145]** using only NrGONS (50 mg) to form ITO-PVP/NrGONS counter electrode. In method **B**, only ITO-PVP/NrGONS counter electrode was used because it showed comparable performance with ITO-Pt counter electrode in method **A**. To make a spacer (between

the photoanode and counter electrode), a 0.6 cm x 0.6 cm hole was cut on a parafilm plastic sheet of dimensions 2.0 cm (length) x 1.5 cm (width). The DSSCs were then assembled as shown in the first set of DSSCs.

Chapter 3: Results and Discussion

Publications arising from this work

The results discussed in the forthcoming chapters have been published or submitted for publication in peer reviewed journals. The articles are listed below

1. Francis Chindeka, Philani Mashazi, Jonathan Britton, Gertrude Fomo, David O. Oluwole, Azole Sindelo, Tebello Nyokong, Optimizing phthalocyanine based dye-sensitized solar cells: the role of reduced graphene oxide. **Synthetic Metals**, 246 (2018) 236–245.
2. Francis Chindeka, Philani Mashazi, Jonathan Britton, David O. Oluwole, Sivuyisiwe Mapukata and Tebello Nyokong, Fabrication of dye-sensitized solar cells based on push-pull asymmetrical substituted zinc and copper phthalocyanines and reduced graphene oxide nanosheets. Submitted to **Journal of Photochemistry and Photobiology A: Chemistry**, accepted with revision.

Additional not related to thesis

3. Munyaradzi Shumba, Sixolile Centane, Francis Chindeka, Tebello Nyokong, Nanocomposites of Sulphur-Nitrogen Co-doped graphene oxide nanosheets and Cobalt Mono Carboxyphenoxy Phthalocyanines for Facile electrocatalysis. **J. Electroanal. Chem**, 791 (2017) 36-48.
4. Sivuyisiwe Mapukata, Francis Chindeka, Kutloano E. Sekhosana, Tebello Nyokong, Laser induced photodegradation of Orange G using phthalocyanine – cobalt ferrite magnetic nanoparticle conjugates electrospun in polystyrene nanofibers. **J. Mol. Cat. A**: Chem Editor's choice paper, 439 (2017) 211-223.

Chapter 3: Results and Discussion

3.1 Synthesis and Characterisation of Metallophthalocyanines (MPc) only

Table 1.3 shows MPc derivatives which were employed in this research. Synthesis and characterisation of complexes (**1**), (**2**) and (**5**) will not be discussed in the following subsections, since they are known MPcs **[132-134]**. Complexes (**3**) and (**4**) are new hence their characterization is provided in this subsection.

3.1.1 Synthesis

3.1.1.1 Complex (3)

Scheme 3.1 shows the synthetic route for complex (**3**).

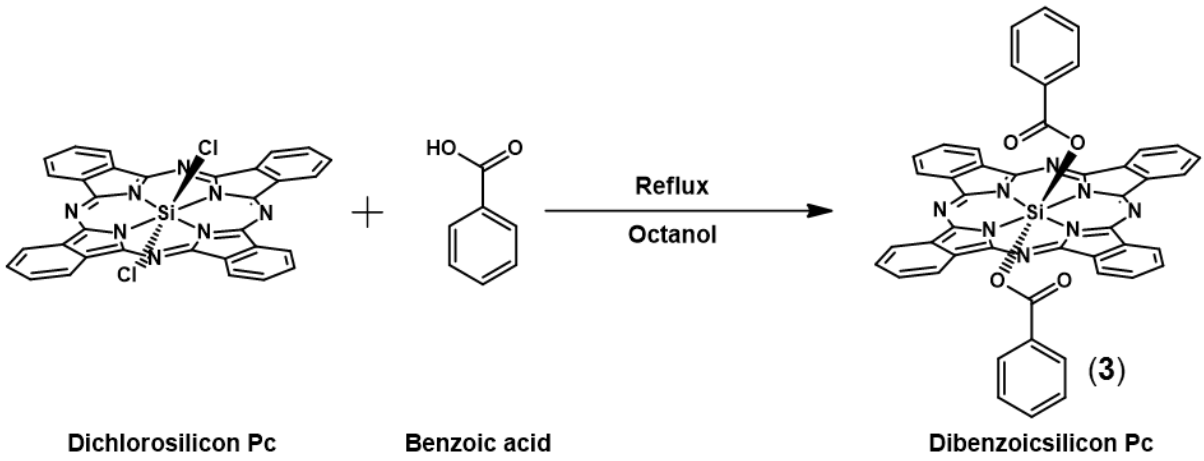

Scheme 3.1: Synthesis of dibenzoicsilicon phthalocyanine complex (**3**)

Evidence of formation of complex (**3**) was proved by MALDI-TOF mass spectrometry. The molecular ion peak at 782.94 m/z is in agreement with the expected value of 782.84 m/z. ^{1}H NMR spectrum as shown in the experimental section integrated for protons was as expected and was in agreement with the proposed structure. Elemental analysis (CHN) for calculated was in agreement with the found CHN values and is in agreement with the fact that Pcs are isolated as hydrates **[146]**.

3.1.1.2 Complex (4)

The **Scheme 3.2** shows the synthesis scheme for complex (**4**). The statistical condensation method between compounds (**6**) and (**7**) in ratio 7: 1 resulted in the formation of symmetrical and asymmetrical complexes. Silica gel column chromatography using DCM/methanol resulted in the elution of the asymmetrical complex (**8**). The hydrolysis of complex (**8**) was carried out to yield carboxylic acid functionalized phthalocyanine complex (**4**).

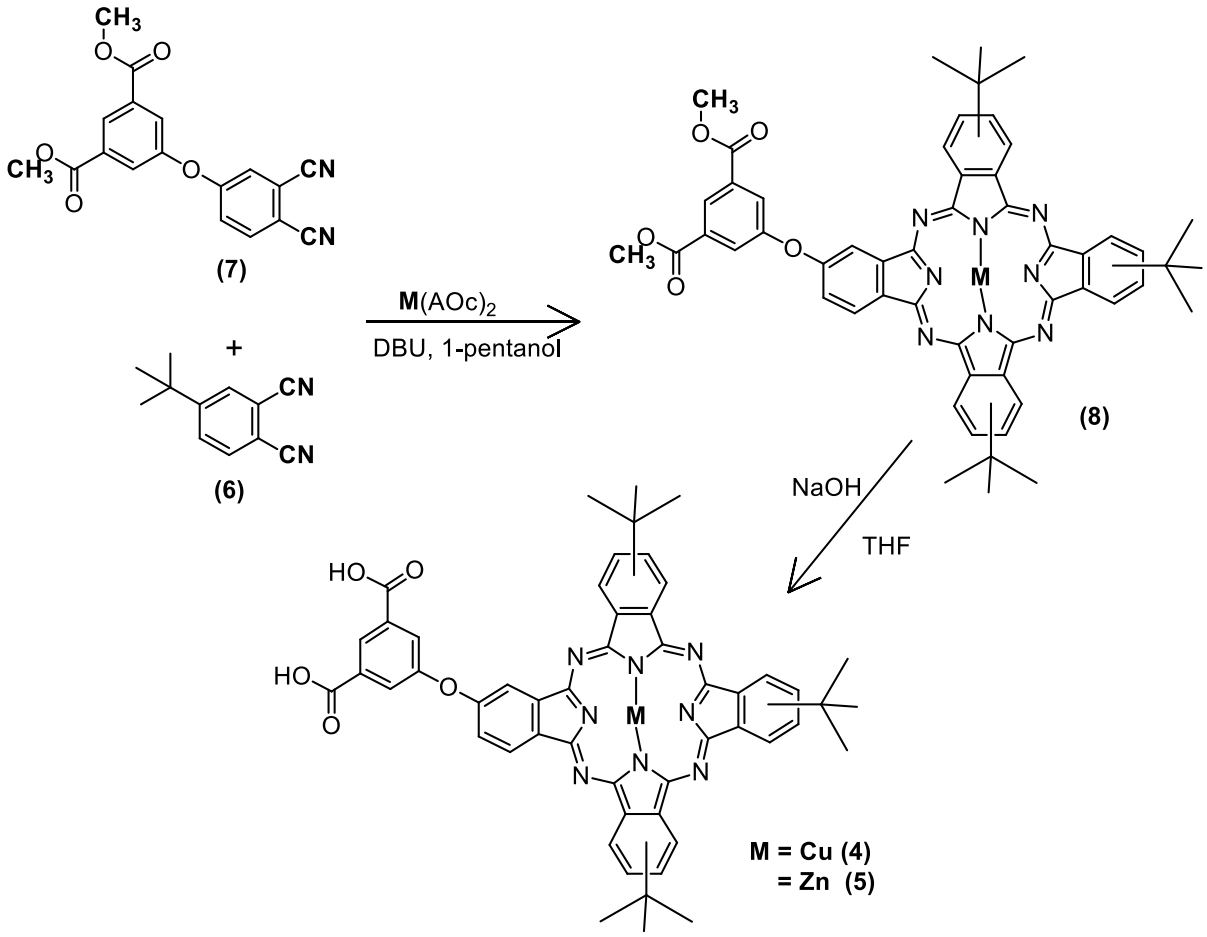

Scheme 3.2: Synthesis route for asymmetric phthalocyanine, CuPc (complex **4**) and the structure of (**5**) **[132].**

3.1.2 UV-Vis Absorption Spectra

Figure 3.1 shows UV-Vis absorption spectra of complexes (i) (**1**), (ii) (**2**), and (iii) (**3**), (a) in DMF and (b) in solid state (ITO-TiO_2 electrode photosensitised with complexes (i) (**1**)**,** (ii) (**2**) and (iii) (**3**). In **Fig. 3.1**(a), an intense Q-band was observed at 688 nm for complex (**1**), 707 nm for complex (**2**), and 675 nm for complex (**3**) (**Table 3.1**). For complexes (**1**) and (**3**) the Q-band showed monomeric behaviour, as can be seen in **Fig. 3.1** (a)(i) and (iii) respectively. The UV-Vis absorption spectrum of complex (**2**) in **Fig. 3.1** (a)(ii) showed a broadened Q-band typical of an aggregated MPc complex **[118]**. Complexes (**1**) and (**3**) did not show aggregation behaviour which is important for the effective sensitisation of the metal oxide semiconducting material. The complexes (**1**-**3**) showed an additional B-band below 450 nm. The Q-band of complex (**3**) is blue shifted (**Table 3.1**) compared to those of (**1**) and (**2**) as a result of a large central metal in (**1**) and (**2**) **[118]**. The solid-state UV-Vis spectra recorded on the ITO-TiO_2 after adsorption of complexes (**1**)-(**3**) are shown in **Fig. 3.1** (b). The solid-state UV-Vis absorption spectra were broad, and this is typical of MPCs which are

aggregated **[125]**. Complex (**3**) in solid state exhibited less aggregation with a less broadened peak.

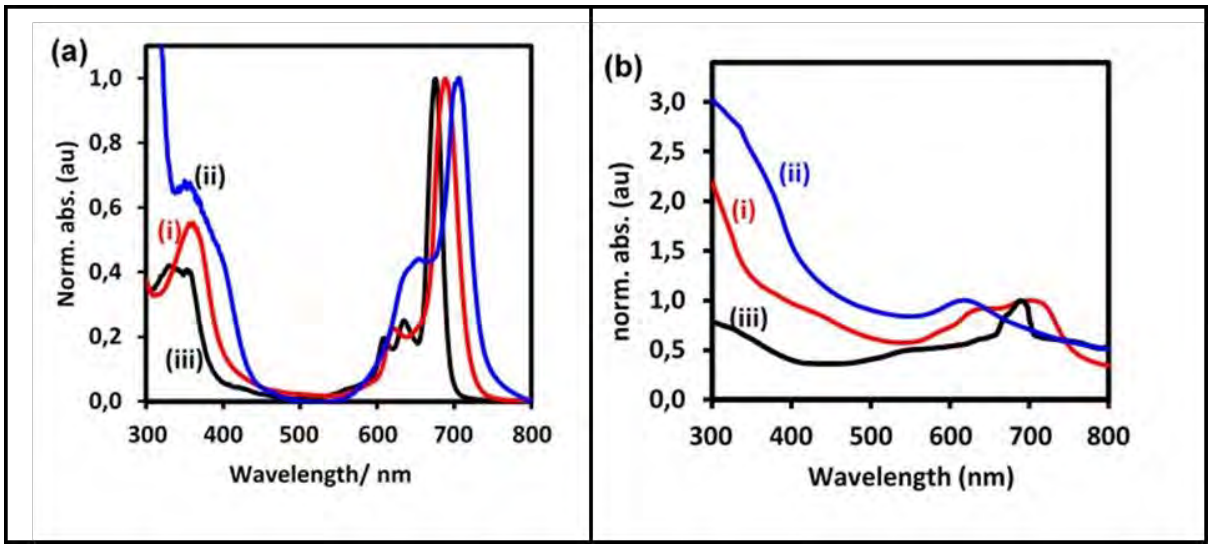

Figure 3.1: UV-Vis absorption spectra of complexes (i) (**1**), (ii) (**2**), and (iii) **3**, (a) 1.0 μM in DMF and (b) in solid state (ITO-TiO_2 electrode photosensitised with complex (i) (**1**)**,** (ii) (**2**) and (iii) (**3**).

The UV-Vis absorption spectra of complexes (**4**) and (**5**) are shown in **Fig. 3.2**. Similar to the UV-Vis in **Fig. 3.1** above, in DMF solution, the absorption spectra of complexes (**4**) and (**5**) exhibited monomeric behaviour with Q-band maxima at 678 nm and 676 nm respectively (**Table 3.1**). The solid-state UV-Vis spectra confirm aggregation as observed for complexes (**1-3**) above. The solid-state spectra on ITO-TiO_2-(**1**)-(**3**) and ITO-TiO_2-(**4**) and (**5**) confirmed the presence of the photosensitiser on the photoanodes for DSSC.

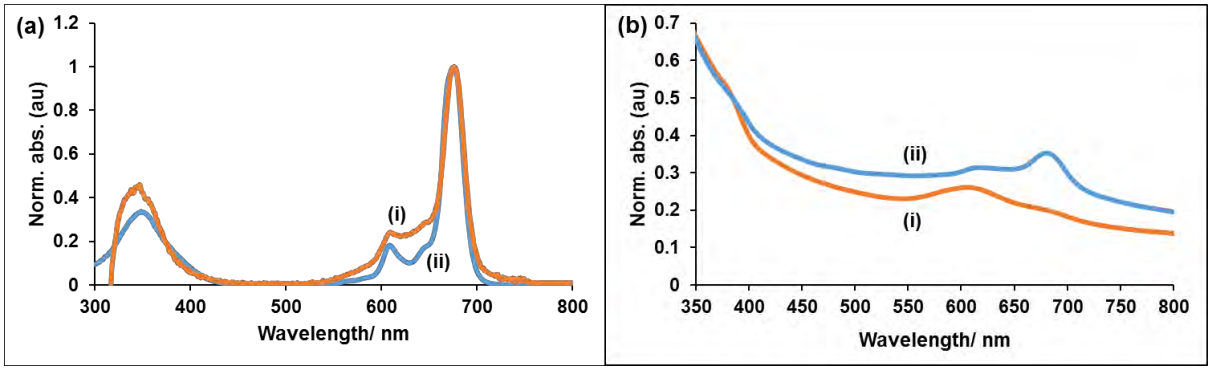

Figure 3.2: UV-Vis absorption spectra of complexes (i) (**4**) and (ii) (**5**) in (a) 1.0 μM in DMF and (b) solid state (ITO-TiO_2/rGONS electrode photosensitised with either complex (i) (**4**) or (ii) (**5**).

3.1.3 Electrochemistry

Differential pulse voltammetry (DPV), **Fig. 3.3,** was employed for the determination of the highest occupied molecular orbital (HOMO) and the lowest unoccupied molecular orbital (LUMO) of complexes (**1**)-(**5**).

The energies of the HOMO (E_{HOMO}) and LUMO (E_{LUMO}) are defined by equations **3.1** and **3.2 [141, 142, 147, 148]**.

$$E_{HOMO}\ (eV) = -E_{1/2}^{ox}(Vs.Fc/Fc^{+}) - 4.8 \qquad (\mathbf{3.1})$$

$$E_{LUMO}\ (eV) = E_{HOMO} + E_g \qquad (\mathbf{3.2})$$

where $E_{1/2}^{ox}$ is the first ring oxidation and E_g is the difference between the HOMO and the LUMO.

$E_{1/2}^{ox}$ values were determined using DPV scans shown in **Fig. 3.3.**

For molecules in which the absorption spectrum mirrors the emission spectrum as in MPcs, E_g is easily determined experimentally as the energy at the intersection of the normalized fluorescence and absorption spectra **[148].**

The potential for the first ring oxidations (**I**, $E_{1/2}^{ox}$) for complexes (**1**)-(**5**)**,** were determined to be 0.82, 0.99, 1.03, 0.45 and 1.07 V, respectively. Using the energy at the intersection of the normalized fluorescence and absorption spectra, the E_g values for complexes (**1**)-(**5**)**,** were found to be 1.78, 1.74, 1.91, 1.82 and 1.83 eV**,** respectively**.** The HOMO/LUMO energy levels, $E_{1/2}^{ox}$ (**I**) and E_g are summarised in **Table 3.1.** According to literature **[142]**, the conduction band of TiO_2 has an energy value of ~ - 4.2 eV and the energy level of the I^-/I_3^- redox couple is ~- 4.89 eV. It can be observed from **Table 3.1** and **Fig 3.4** that the LUMO positions for the MPcs in this work are higher than TiO_2 conduction band, which is a fundamental requisite for electron injection into the TiO_2 conduction band from the excited dye. The HOMO levels of the MPcs are also lower than the energy of the redox (I^-/I_3^-) couple, enabling the regeneration of the oxidised dye.

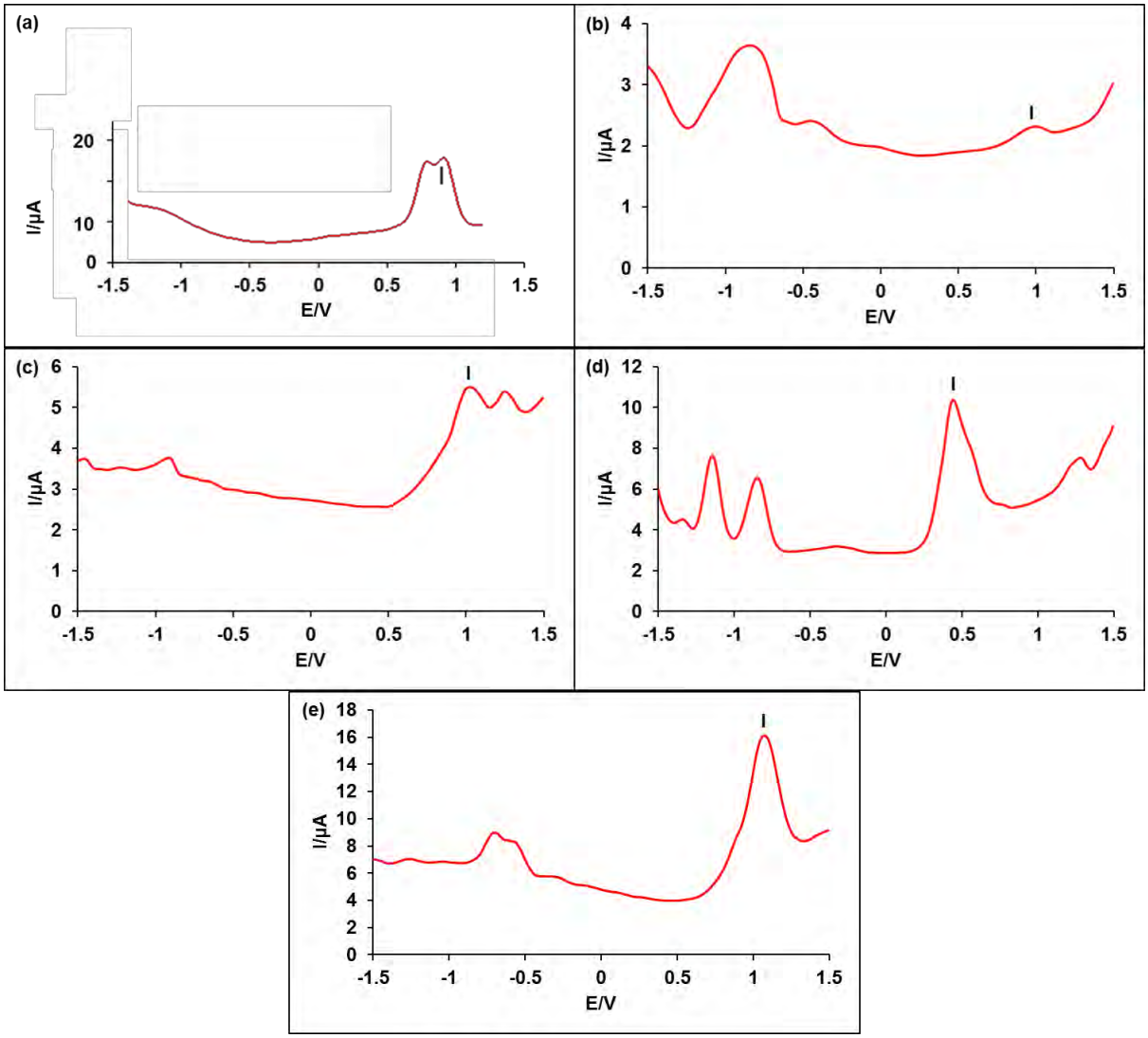

Figure 3.3: Differential pulse voltammograms (DPV) for complexes (**a**) (**1**), (**b**) (**2**), (**c**) (**3**), (**d**) (**4**) and (**e**) (**5**). MPcs in the presence of Fc/Fc^{+}. MPc concentration = 0.050 M in DMF containing 0.100 M of $TBABF_4$.

Table 3.1: Maximum absorption and emission wavelengths (nm), half-wave potential ($E_{1/2}^{ox}$), band gap (eV), HOMO and LUMO energies (eV) for complexes (**1**)-(**5**) in DMF. All potentials are referenced to ferrocene/ferrocenium (Fc/Fc^+) redox couple.

Complex	λ $(abs)_{max}$ (nm)	λ $(em)_{max}$ (nm)	$E_{½}^{ox}$ (V)	E_{HOMO} (eV)	E_{LUMO} (eV)	E_g (eV)
(1)	688	717	0.82	-5.62	-3.84	1.78
(2)	707	728	0.99	-5.79	-4.05	1.74
(3)	675	678	1.03	-5.83	-3.92	1.91
(4)	678	698	0.45	-5.25	-3.43	1.82
(5)	676	683	1.07	-5.87	-4.04	1.83

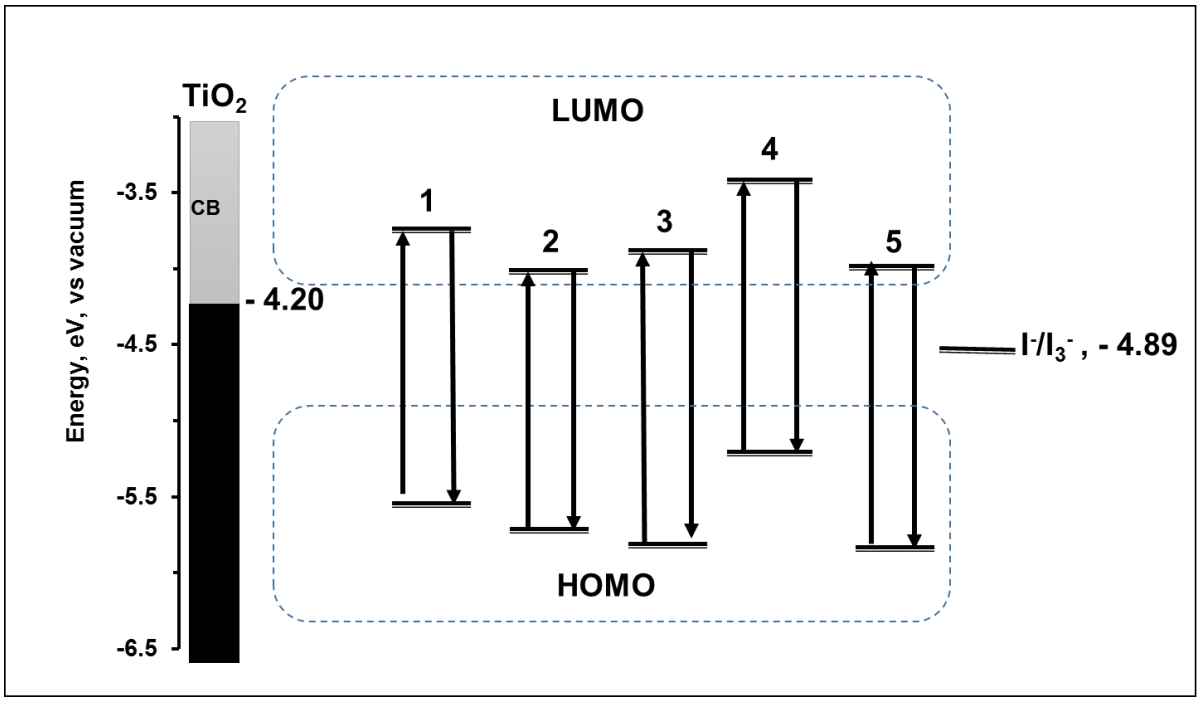

Figure 3.4: Energy level diagram for complexes (**1**)-(**5**) (relative to TiO_2 and the redox mediator) derived from electrochemical and optical data. CB = conduction band of TiO_2.

3.2 Synthesis and characterization of graphene oxide nanosheets (rGONS and NrGONS)

3.2.1 Synthesis

The rGONS were synthesized using the atmospheric pressure chemical vapour deposition (APCVD) method according to literature **[36]**, **Scheme 3.3**, but at a lower temperature (650 °C instead of 1000 °C used in literature). Also, a slower heating rate of 10 °C/min to reach the final temperature was used instead of 15 °C/min used in literature **[36]**. As stated above, thermal annealing can eliminate oxygen functional groups on GONS to produce rGONS **[143]**, as is the case in this work.

The growth mechanism of graphene may be different depending on the type of metal used as substrate **[149, 150]**. In this work copper was used as a substrate. Graphene grows on Cu by direct deposition using chemical vapour deposition (CVD). According to literature **[150]** parameters such as temperature, hydrocarbon flow rate and partial pressures seem to affect the number of graphene nucleation islands. It has been reported that island density decreases, and their sizes increase at higher temperatures, lower hydrocarbon flux and partial pressures. However, conditions that yield low nucleation densities also yield an incomplete coverage of the Cu surface **[150]**. Loginova et al. **[151]** intentionally used low temperatures (500–700°C) to avoid carbon diffusion to the substrate bulk during the evaporation of C atoms over Ru(0001). In contrast, Sutter et al. **[152]** used higher temperature (850–1150 °C) to promote carbon dissolution and segregation for the growth of single and bilayer graphene. These two examples represent the ability to use different temperature ranges to select the mechanism by which graphene grows. In this work, low

temperature was used and in addition to the above reasons, the use of low temperature avoids hazards especially when working with flammable gases like C_2H_2.

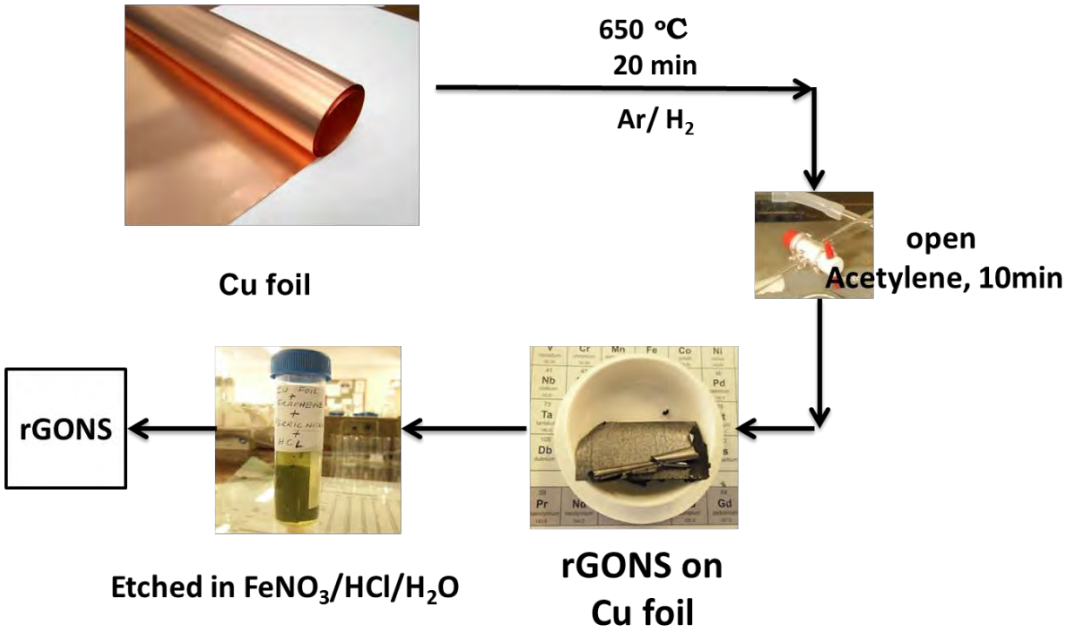

Scheme 3.3: Reduced graphene oxide nanosheets synthesis by atmospheric pressure chemical vapor deposition (APCVD) with acetylene.

The incorporation of the nitrogen heteroatom into graphene can significantly enhance the catalytic activity, decrease the charge transfer resistance, and hence improve the photovoltaic performance of DSSCs **[153]**. Nitrogen doping of graphene can produce local strains in a hexagonal carbon network. This will lead to structural deformations. The additional lone pair of electrons of nitrogen atoms can bring negative charges with respect to the delocalized π-system of an sp^2-hybridized carbon framework. This can enhance electron-transfer ability and electrocatalytic activity **[63]**. Melamine was used as a source of nitrogen in this work.

The degree of nitrogen doping depends on mass ratio of rGONS to melamine, the annealing temperature and time. At constant annealing temperature and time, the

doping level will increase with an increase in the amount of melamine **[73]**. In this study, the mass ratio was 1:5 (rGONS:melamine). According to Sheng et. al. **[73]** the possible doping process is as follows: melamine adsorbed on graphene oxide is condensed to carbon nitride with increasing temperature, simultaneously oxygen groups linked to graphene nanosheets are removed at high temperature. This removal of oxygen species provides active sites that can be attacked by nitrogen atoms formed by decomposition of carbon nitride.

3.2.2 TEM Analysis

The morphologies of the rGONS and NrGONS were investigated using TEM, **Fig. 3.5**. The TEM micrograph for rGONS, **Fig. 3.5** (a), shows that the nanosheets are randomly compact and disorderly stacked together showing wrinkles typical of graphene like materials **[36,71,72,154,155]**. TEM images of nitrogen doped graphene oxide (NrGONS) showed morphologies in agreement with literature **[73,155,156]**. The nanosheets were randomly compact and stacked together showing uniform laminar morphology like crumpled silk veil waves as shown by micrograph in **Fig 3.6** (b). This morphology is attributed to defective structures that are formed due to the presence of doped nitrogen atoms **[72,73,156]**.

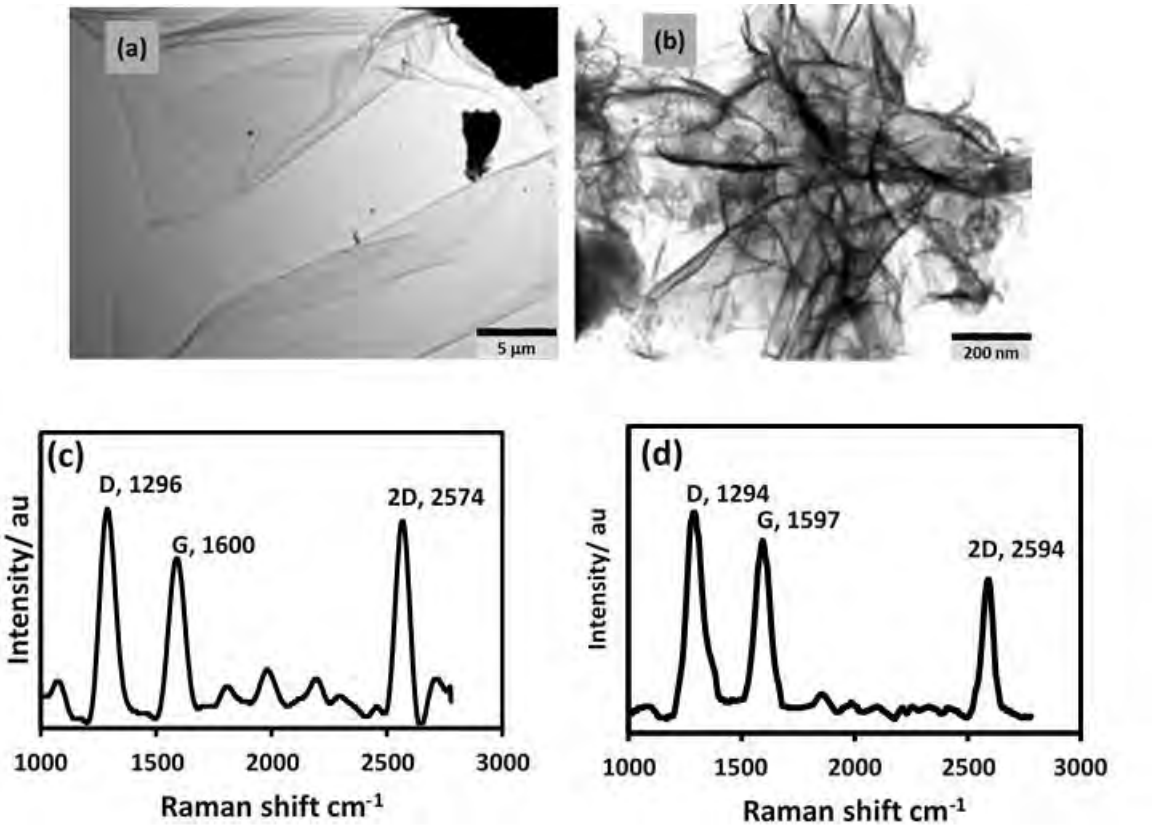

Figure 3.5: TEM micrographs of (a) rGONS and (b) NrGONS and the Raman spectra of (c) rGONS and (d) NrGONS.

3.2.3 Raman Spectroscopy

Raman spectroscopy was used to characterise rGONS and NrGONS, **Fig. 3.5** (**c**) and (**d**), respectively. The D bands are centred at 1296 cm^{-1} and 1294 cm^{-1} for rGONS and NrGONS, respectively, and are attributed to structural defects on the graphitic plane (disorder band; sp^3). The G bands are centred at 1600 cm^{-1} and 1597 cm^{-1} for rGONS and NrGONS, respectively. G bands are attributed to the E_{2g} vibrational mode present in the sp^2 bonded graphitic carbons (tangential mode). The 2D bands (overtones of the D band) are centred at 2574 cm^{-1} and 2594 cm^{-1} for rGONS and NrGONS, respectively, and are attributed to a two-photon double resonance Raman process

[36,71-73,118,155-161]. The ratio of D/G provides an indication of the amount of structural defects and a quantitative measure of edge exposure (the lower the intensity ratio, the less the structural defects) **[36,71-73,118, 155-161]**. rGONS had D/G ratio of 1.3 and NrGONS of 1.2, hence less defects for NrGONS. This could be because nitrogen doping also causes reduction of rGONS thus slightly restoring the graphitic structure. Ju et al **[162]** and Sheng et al **[73]** made similar observations. The second order Raman 2D band is sensitive to the number of layers **[36,71-73,118, 155-161]**. The shape and position of the 2D peak distinguishes between single layer, bilayer and few layer graphene nanosheets. The intensity ratio G/2D gives an indication of number of layers. G/2D ratios for rGONS and NrGONS were 0.80 and 1.24 respectively indicating bilayers for both. According to literature bilayers are present for G/2D ratio ranging from 0.77 to 1.69 **[36]**.

3.2.4 XPS Analysis

XPS is a useful tool in determining the chemical compositions of surfaces. **Figure 3.6** shows the XPS spectra for the rGONS and the NrGONS both the (**a**) survey spectra and (**b-f**) high resolution spectra of carbon (C 1s), nitrogen (N 1s) and oxygen (O 1s). **Figure 3.6(a)** shows the survey spectra of (i) rGONS and (ii) NrGONS which revealed the presence of C 1s, N 1s (for NrGONS only) and O 1s at their respective positions. The sample compositions showed that the rGONS contained 92.1% C 1s and 7.9% of O 1s, **Table 3.2.** The NrGONS samples showed an additional peak at around 400 eV due to the doped nitrogen. The elemental composition was 94.2% C1s, 1.4% N1s and 4.4% O1s for NrGONS, confirming the doping of nitrogen onto the graphene oxide nanosheets. It was interesting to observe the decrease in the oxygen (O1s) content for rGONS (7.9%) compared to NrGONS (4.4%), **Table 3.2**. This decrease was due

to the simultaneous displacement of oxygen by nitrogen. The C/O ratios for rGONS and NrGONS are 11.7 and 21.4, respectively.

The C 1s high resolution XPS profile of rGONS was deconvoluted and had the following bonding configurations, **Fig. 3.6** (**b**): undamaged structures of sp^2-hybridized carbon (284.4 eV, C=C, non-oxygenated, aromatic), damaged structures or sp^3-hybridized carbons (285.5 eV, C-C, aliphatic), C-OH groups (286.6 eV, hydroxyl), O-C-O/ C=O functional groups (288.2 eV, carbonyl), C(O)OH groups (289.5 eV, carboxyl) and π – π shake up (291.1 eV), **Table 3.2 [71,159,160]**.

The high resolution C1s XPS spectra of NrGONS has 4 peaks, one main peak at 284.5 eV corresponding to sp^2 hybridised graphitic carbon atoms (C=C), two small peaks at 286.0 and 289.0 eV representing C=N and C-N/C-O respectively and at 290.9 representing π-π shake up **[72,73,156,157,161]**, **Fig. 3.6 (c)**, **Table 3.2**.

The high resolution N1s XPS spectra of the NrGONS in **Fig. 3.6(d)** has four peaks at 398.0, 399.4, 401.1 and 404.7 eV, **Table 3.2**. According to literature **[72,73,156, 157,161]** these peaks correspond to pyridine-N (sp^2 hybridisation), pyrrollic-N, graphitic-N, and N-oxides of pyridinic-N, respectively.

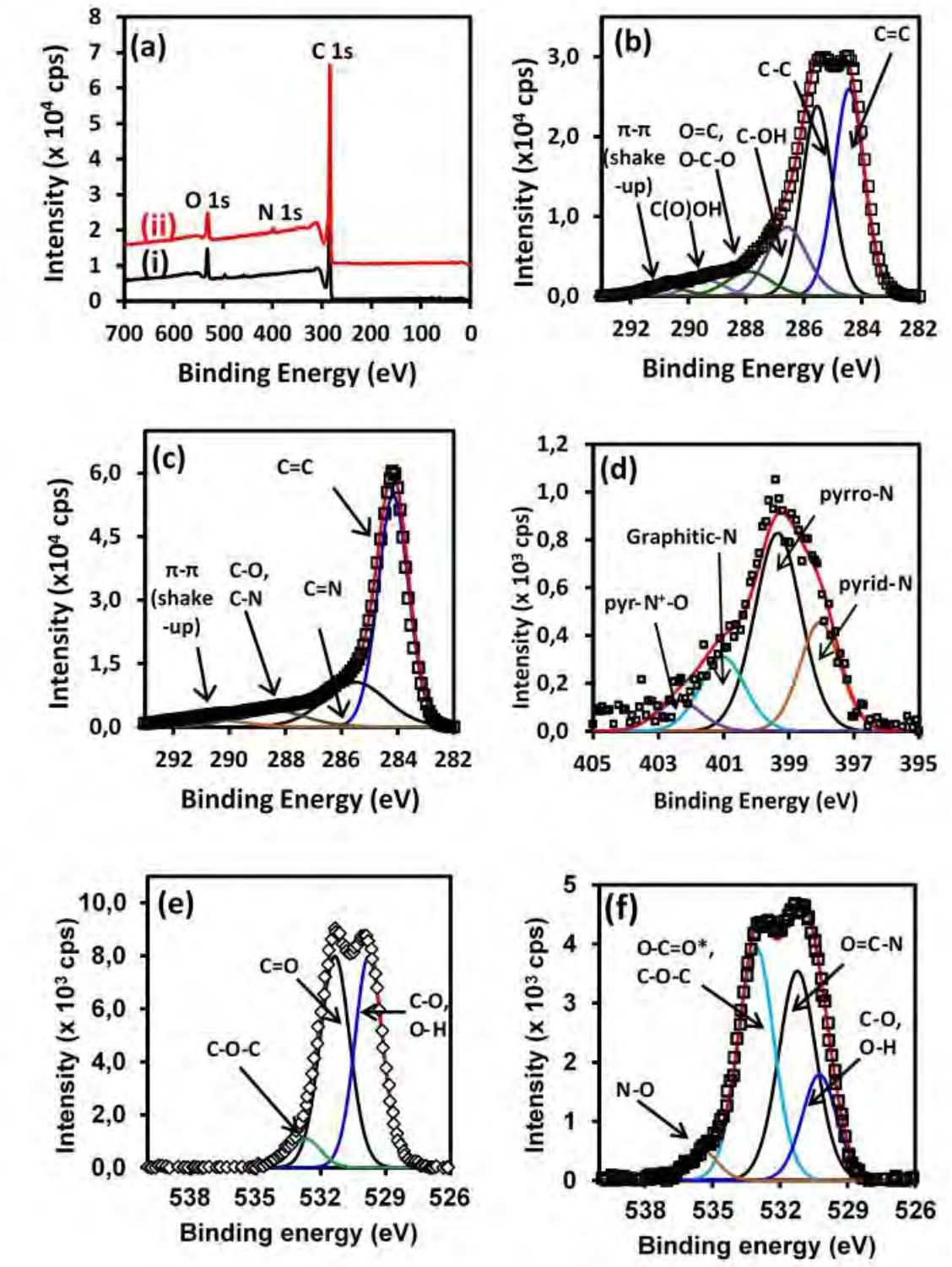

Figure 3.6: (a) Survey spectra of (i) rGONS and (ii) NrGONS, high resolution C1s spectra for (b) rGONS and (c) NrGONS, (d) N1s spectra for NrGONS, and O1s of (e) rGONS and (f) NrGONS.

The contribution of the nitrogen functional groups to the enhanced electrocatalytic activity is not well defined. Previous studies suggest that the nitrogen states, rather than the total N content, have a significant effect on the catalytic activity. The nitrogen states can provide active sites for promoting triiodide reduction reaction, probably due to the shift in redox potential and the lowered adsorption energy **[63,153,157]**. Some studies **[72,73,156,157,153,161]** suggest that pyridinic and /or pyrolic-N, and others suggest graphitic nitrogen functional groups contribute to the improvement in the catalytic activity of NrGONS. In this study, data analysis of the high resolution N1s XPS spectra show that pyrrolic-N (48.5% atomic concentration, 399.4 eV) is the main component in NrGONS, **Table 3.2**.

The O 1s high resolution was also investigated and the deconvoluted spectra are shown in **Fig. 3.6(e)** and **(f)** for rGONS and NrGONS, respectively. The O 1s of rGONS in **Fig. 3.6(e)** revealed three peaks at 529.8 eV for C-O, O-H (46.8%), 531.4 eV for C=O (46.8%) and at 532.7 eV for C-O-C (6.4%). For NrGONS in **Fig. 3.6(f)**, the O 1s high resolution spectrum was deconvoluted and four components were synthesized at 530.3 eV for C-O and O-H (16.8%), 531.2 eV for C=O (33.2%), 533.1 eV for C-O-C (36.9%) and at 535.4 eV for N-O (13.1%). There was a drastic decrease in the C-O and O-H components from 46.8% for rGONS to 16.8% for NrGONS confirming the displacement of oxygen by nitrogen during the doping reaction. Also, the C=O decreased from 46.8% for rGONS to 33.2% for NrGONS further confirming the nitrogen doping. The XPS results are summarized in **Table 3.2.**

Table 3.2: Summary of the XPS data, percentage compositions (at %), and components obtained after deconvolution and their percentage contributions, peak assignments.

Sample	Element	% Atomic composition	Position (BE, eV)[a]	Assignment (% composition contribution)
rGONS	C 1s	92.1	284.4	C=C (**37.0**)
			285.5	C-C (**34.0**)
			286.6	C-OH (**16.4**)
			288.2	C=O, O-C-O (**6.6**)
			289.5	C(O)OH (**3.6**)
			291.1	π-π (**2.4**)
	O 1s	7.9	529.8	C-O, O-H (**46.8**)
			531.4	C=O (**46.8**)
			532.7	C-O-C (**6.4**)
NrGONS	C 1s	94.2	284.5	C=C (**76.7**)
			286.0	C=N (**14.8**)
			289.0	C-N/C-O (**5.7**)
			290.9	π-π (shake-up) (**2.8**)
	N1s	1.4	398.0	Pyridinic-N (**26.7**)
			399.4	Pyrrolic-N (**48.5**)
			401.1	Graphitic-N (**18.2**)
			404.7	Pyridinic-N^+-O (**6.7**)
	O1s	4.4	530.3	C-O, O-H (**16.8**)
			531.2	C=O (**33.2**)
			533.1	C-O-C (**36.9**)
			535.4	N-O (**13.1**)

[a]BE (binding energy)

3.2.5 XRD Analysis

X-ray diffraction patterns were recorded in the range of 10° to 60° for rGONS and NrGONS, **Fig. 3.7**. The pattern for rGONS shows a broad and intense diffraction peak at 2θ = 25.5°. This corresponds to d-spacing of 0.349 nm assigned to (002) reflection plane of graphene which confirms the formation of reduced graphene oxide (rGONS) **[163]**. A lower intensity peak observed at around 44° corresponds to (001) plane of

rGONS. NrGONS had a pattern similar to rGONS, with a less intense peak seen at around 2θ = 25.7° with interlayer spacing (d_{002}) of 0.346 nm. There was also a less intense peak at 43.65°. The slight difference between rGONS and NrGONS spectra maybe due to defects resulting from the nitrogen doping **[163, 164]**.

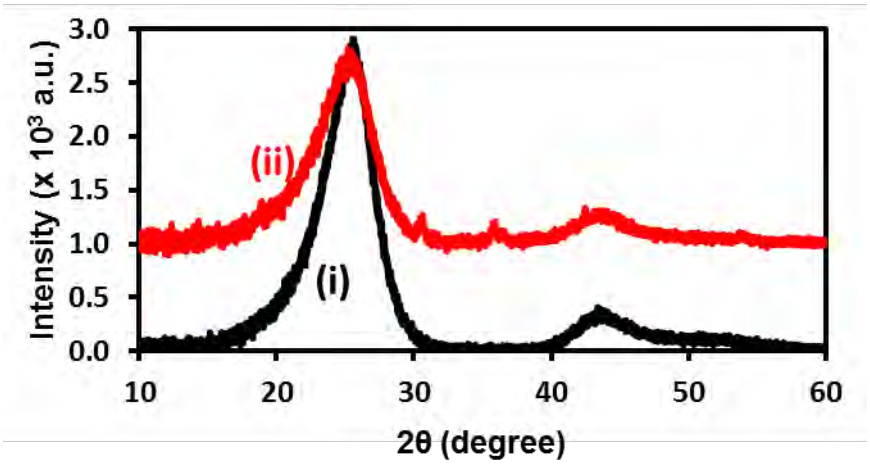

Figure 3.7: XRD diffraction pattern of (i) rGONS and (ii) NrGONS.

3.3 Characterisation of photoanodes and counter electrodes

Figure 3.8 represents one of the DSSCs fabricated in this work, with photoanode consisting of ITO-TiO_2/rGONS-(**3**) and ITO-PVP/NrGONS counter electrode (as an example).

Photoanodes for the DSSCs were fabricated using two different methods (**A** and **B**). In method **A**, the doctor blade technique was used for applying the metal oxide semiconducting materials (TiO_2 or TiO_2/rGONS or TiO_2/NrGONS) onto ITO in order to fabricate the photoanodes. In method **B**, screen printing was used. Photoanodes fabricated using method **A,** were photosensitised using complexes (**1**) to (**3**) and those fabricated using method **B** were photosensitised using complexes (**4**) and (**5**)**.** The

equipment for the latter method **B** (screen printer), was not available at the time DSSCs for complexes (**1**) to (**3**) were developed.

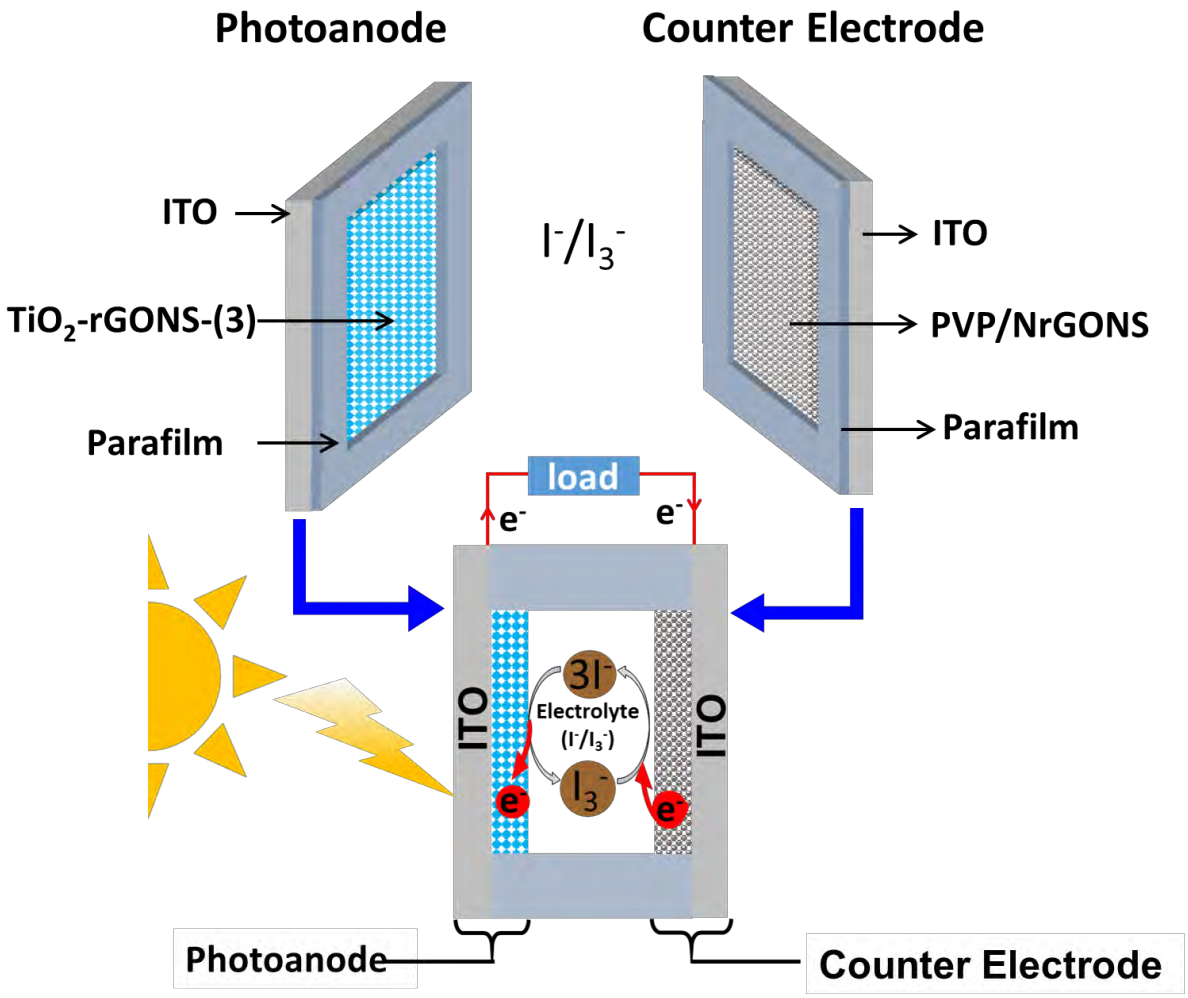

Figure 3.8: Schematic representation of the photoanode (ITO-TiO_2/rGONS-**3**), counter electrode (ITO-PVP/NrGONS) and the complete dye-sensitized solar cell (as an example).

3.3.1 SEM

The SEM image in **Fig. 3.9(a)** shows the photoanode with TiO_2 film deposited using method **A** (doctor blade technique). **Figure 3.9(b)** represents the photoanode with TiO_2/rGONS deposited using method **B** (screen printing). **Figure 3.9(a)** shows that the

TiO_2 film is unevenly distributed with thicknesses ranging from 87.6 to 116 µm and **Fig. 3.9(b)** shows that the TiO_2/rGONS film had thicknesses ranging from 24.48 to 25.60 µm. Thus screen printing (method **B**) resulted in lower thicknesses and narrow ranges, which is preferred, hence the remaining characterisation (except EIS) of the photoanodes (AFM, TOF-SIMS) was done on photoanodes fabricated using method **B**.

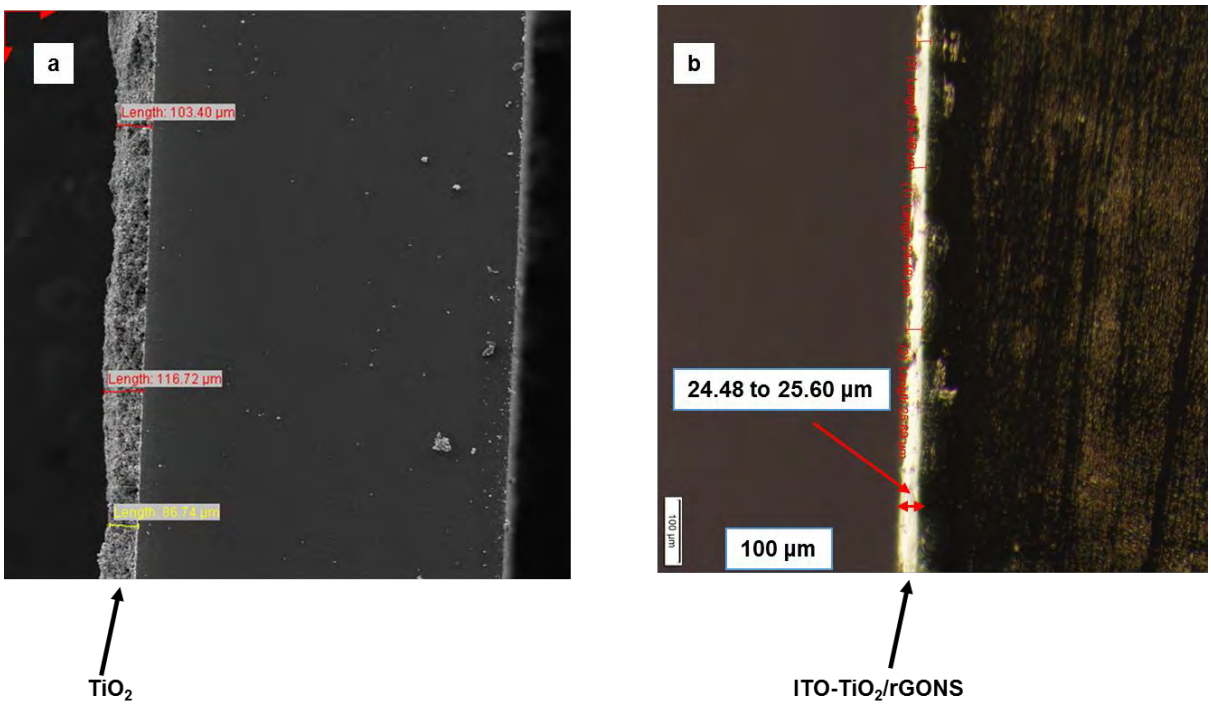

Figure 3.9: Scanning electron microscopy (SEM) cross-section analysis of (**a**) TiO_2 deposited using method **A** and (**b**) TiO_2/rGONS deposited using method **B**.

3.3.2 AFM

The surface morphology of the ITO-TiO_2/rGONS photoanode fabricated using method **B** (as a representative) was investigated using atomic force microscopy (AFM). **Figure 3.10** shows the AFM **(i)** 2D surface topology, **(ii)** section graph and **(iii)** 3D surface topology on a scan size of 20 x 20 µm of **(a)** ITO and **(b)** ITO-TiO_2/rGONS photoanode.

A range of parameters divided into four categories namely amplitude, spacing, hybrid and functional are used to describe surface profiles. Root mean square (RMS) falls under the amplitude parameters and together with peak to valley roughness and average roughness are used to describe roughness of a surface in AFM. RMS is given by the standard deviation of the height (z) values for the sample area **[1, 165,166]**. **Figure 3.10(a)** represents the surface topology of ITO. It shows that the surface is generally smooth with an RMS roughness value of 1.33 nm. The AFM topography images and section graph in **Fig. 3.10(b)** reveal that the ITO-TiO_2/rGONS photoanode is porous and has an RMS roughness value of 121.95 nm, which is higher than that of ITO. The higher the RMS value, the higher the surface roughness. Higher surface roughness improves DSSC efficiency due to an increase in the surface area and hence increased dye adsorption. A good photoanode will facilitate light harvesting, electron injection and electron collection. Maximising light harvesting requires: (a) transparency for the unsensitised semiconductor framework and (b) sufficiently high internal surface area to enable maximum absorption of the dye **[167-169]**. Since the roughness is related to the internal area available for the absorption of dye, a larger area means more dye is absorbed and better performance.

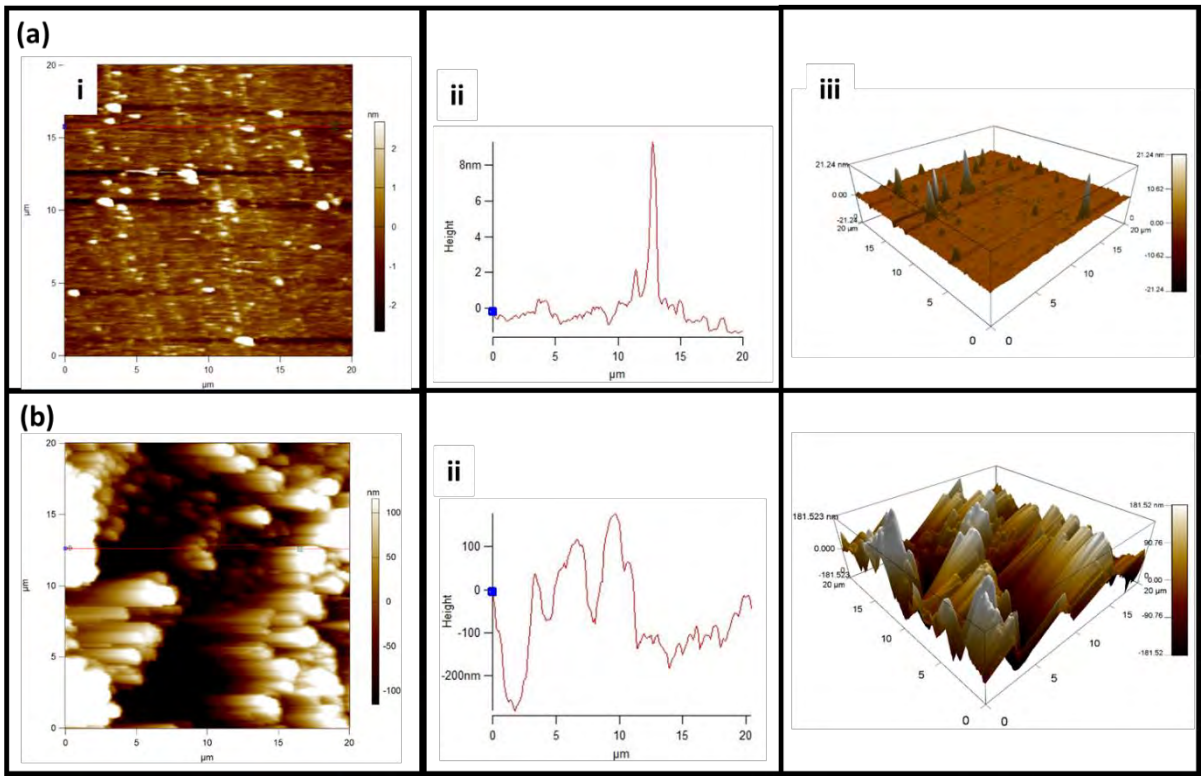

Figure 3.10: AFM images **(i)** 2D surface topology, **(ii)** section graph and **(iii)** 3D surface topology on a scan size of 20 x 20 µm of **(a)** ITO and **(b)** ITO-TiO_2/rGONS photoanode fabricated in method **B**.

3.3.3 TOF-SIMS Analysis

TOF-SIMS was used for characterizing the surface of rGONS modified TiO_2 photoanode (ITO-TiO_2/rGONS), fabricated using method **B** (as an example), before and after dye adsorption, in order to determine the characteristic distributions of the different compounds. TOF-SIMS uses a focused bismuth beam to dislodge species on the sample surface. Particles produced closer to the site of impact tend to be dissociated ions (positive or negative) while those generated further from the impact site tend to be molecular compounds, typically fragments of much larger organic macromolecules. In order to detect both positive and negative ions, TOF-SIMS can be run in positive ion mode (detects positive ions) or negative ion mode (detects negative ions). In this work, ion density maps, or secondary ion images and spectra, were

acquired in both positive and negative ion mode over areas of 250 × 250 μm^2. These TOF-SIMS secondary ion images present “chemical images” of the different samples, showing characteristic distributions of the elements/ compounds.

The 2D TOF-SIMS positive ion mode image of ITO in **Fig. 3.11 (a)** shows the mass locations of indium (red, m/z 115), tin (green, m/z 120) and sodium (blue, m/z 24) originating from ITO. Indium and tin occupy the same locations.

Figure 3.11(b) is a 2D TOFSIMS positive ion mode image of ITO-TiO_2/rGONS photoanode showing mass locations for titanium (red, m/z 48), indium (green, m/z 115) and the phenol ring (blue, m/z 91). Due to the harsh nature of the bismuth cluster gun, it is conceivable that hydrogen atoms could be lost from any phenol rings present in the photoanode. Titanium and the phenol ring are fragments from TiO_2 and rGONS respectively. The purple color is due to Ti (red) and the phenol ring (blue) appearing in the same locations. This is proof that TiO_2 and rGONS formed a homogenous mixture. There is also some indication of the ITO being exposed in the cracks in the image, indicating that there is no TiO_2/GONS within these cracks. The cracks are due to sintering/heating the photoanode at 450 °C.

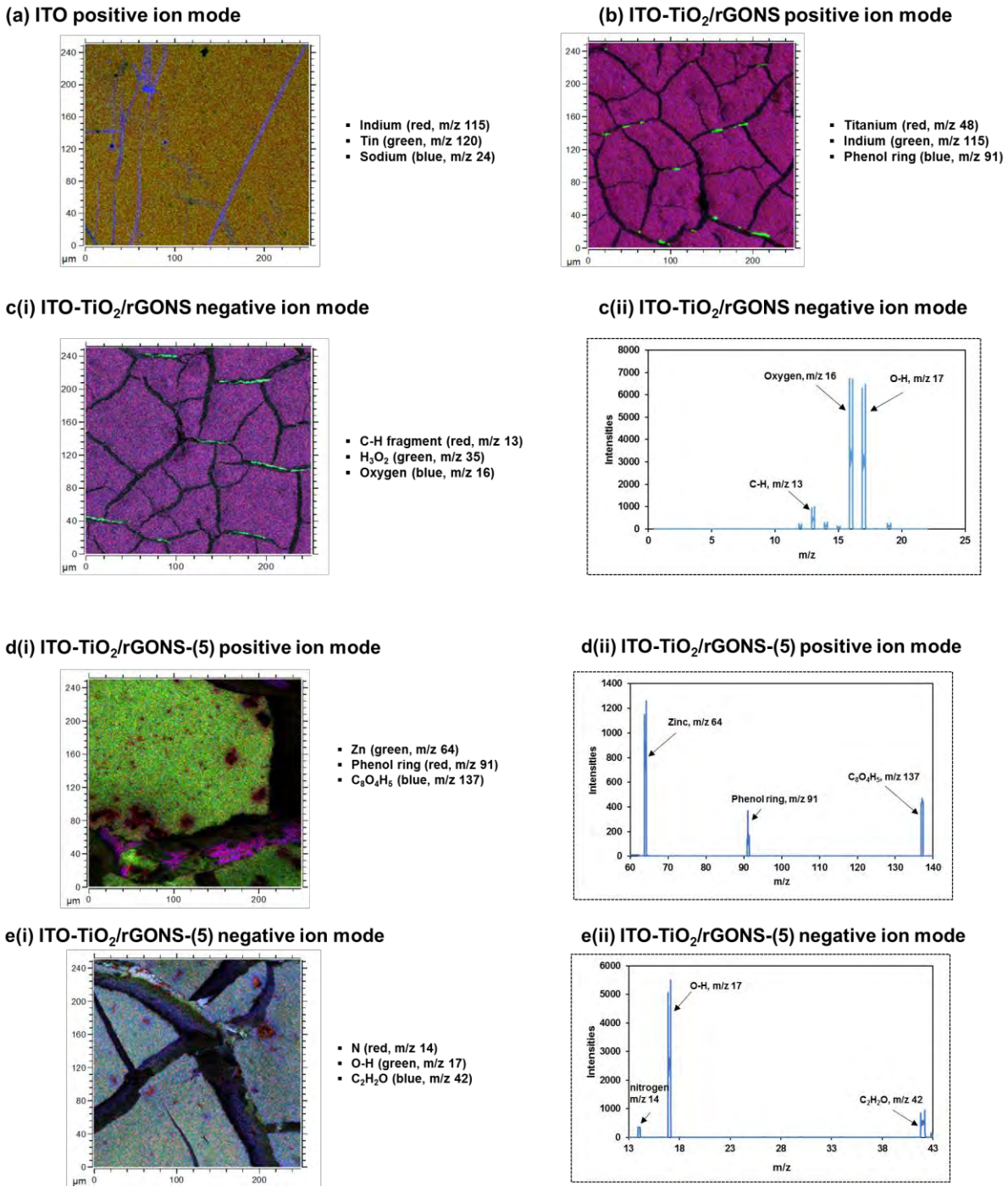

Figure 3.11: 2D TOF-SIMS ion images of **(a)** ITO, **(b)** ITO-TiO_2/rGONS photoanode positive ion mode, **(c)(i)** ITO-TiO_2/rGONS photoanode negative ion mode and **(ii)** the corresponding ion spectrum extracted from (c)(i). **(d)(i)** ITO-TiO_2/rGONS-**5** photoanode positive ion mode and **(ii)** the corresponding ion spectrum extracted from (d)(i). **(e)(i)** ITO-TiO_2/rGONS-**5** negative ion mode and **(ii)** the corresponding ion spectrum extracted from (e)(i).

The negative ion mode image of ITO-TiO_2/rGONS **(Fig. 3.11 (c)(i))** shows mass locations for the C-H fragment (red, m/z 13), H_3O_2 (green, m/z 35) and oxygen (blue, m/z 16). H_3O_2 is a fragment from both TiO_2 and rGONS. C-H and oxygen occur in the same locations. However, there is a difference in intensities of these two masses, expressed as maximal number of counts in a pixel (mc) (C-H, 18 mc and oxygen, 117 mc). This suggests that C-H is a fragment from rGONS, whilst the oxygen is originating from both rGONS and TiO_2 (because there is higher oxygen content than C-H content), **Fig. 3.11(c)(ii)**. It can be inferred from these positive and negative ion mode images that titanium is also present where oxygen and C-H are present because they are within the same islands/ plates, also confirming that rGONS and TiO_2 formed a homogenous mixture. **Figure 3.11(c)(ii)** represents the mass spectrum extracted from the negative ion mode image of ITO-TiO_2/rGONS (**Fig. 3.11(c)(i)**) in the range m/z 0 - 25 showing peaks for the C-H fragment (m/z 13), oxygen (m/z 16) and the O-H fragment (m/z 17). **Figure 3.11(d)(i)** is a 2D image (positive ion mode) of ITO-TiO_2/rGONS-(**5**) indicating mass locations for the phenol ring (red, m/z 91), Zn (green, m/z 64), and $C_8O_4H_5$ (blue, m/z 137). **Figure 3.11(d)(ii)** is the mass spectrum extracted from the image in **Fig. 3.11(d)(i)**. Zinc originates from complex (**5**). The phenol ring and the $C_8O_4H_5$ fragment are from both complex (**5**) and rGONS. It can also be observed that TiO_2 and the organic compounds (from the phthalocyanine and rGONS) occupy the same area. This confirms sensitisation of the photoanode by complex (**5**) because of the presence of Zn and organic fragments from the zinc phthalocyanine derivative (**5**). **Figure 3.11 (e)(i)** represents a 2D negative ion mode image of ITO-TiO_2/rGONS-(**5**) showing mass locations for N (m/z 14, red), O-H (m/z 17, green) and C_2H_2O (m/z 42, blue). N and C_2H_2O are fragments from the complex (**5**) and rGONS respectively. The hydroxyl group (O-H) emanates from both the TiO_2

surface and rGONS. This also confirms photosensitisation of the photoanode by complex (**5**). **Figure 3.11e(ii)** represents the mass spectrum extracted from the image in **Fig. 3.11 (e)(i).** The discussions on **Figs. 3.11(b)** to **(e)** prove that rGONS and TiO_2 are homogenously mixed. The discussions also confirm the presence of the phthalocyanine in the titanium layer thus confirming photosensitisation.

3.3.4 Electrochemical Impedance Spectroscopy

Electrochemical impedance spectroscopy (EIS) studies were conducted to evaluate the charge transfer properties of the different counter electrodes used in this study (ITO-Pt, ITO-PVP/rGONS and ITO-PVP/NrGONS), fabricated using method **A**. The Nyquist plots obtained from EIS are shown in **Fig. 3.12** measured in 0.2 mM $[Fe(CN)_6]^{3-/4-}$ containing 1.0 mM KCl. The semicircle diameter at high frequency region represents the charge transfer resistance (R_{ct}) of the studied electrodes and the linear part at lower frequency region corresponds to the electrolyte diffusion properties. The experimental fitting of the Nyquist plots was modelled by Randles-Sevcik equivalent circuit (inset in **Fig. 3.12**) comprising of the solution resistance (R_{sol}), charge-transfer resistance (R_{ct}), Warburg impedance (W, Z_w) and constant phase element (CPE, Q). The larger the semicircle diameter, the higher the charge transfer resistance (R_{ct}). R_{ct} of Pt (4.01 kΩ) and NrGONS (4.24 kΩ) modified surfaces were very comparable. Thus NrGONS are a good candidate for replacing Pt as catalyst at the counter electrode. The value of the charge transfer resistance (R_{ct}) depends on the dielectric and insulating features at the electrode/electrolyte interface. The lower the value of R_{ct}, the higher the conductance of the electrode (meaning the electrode is an excellent conducting material and can accelerate electron transfer).

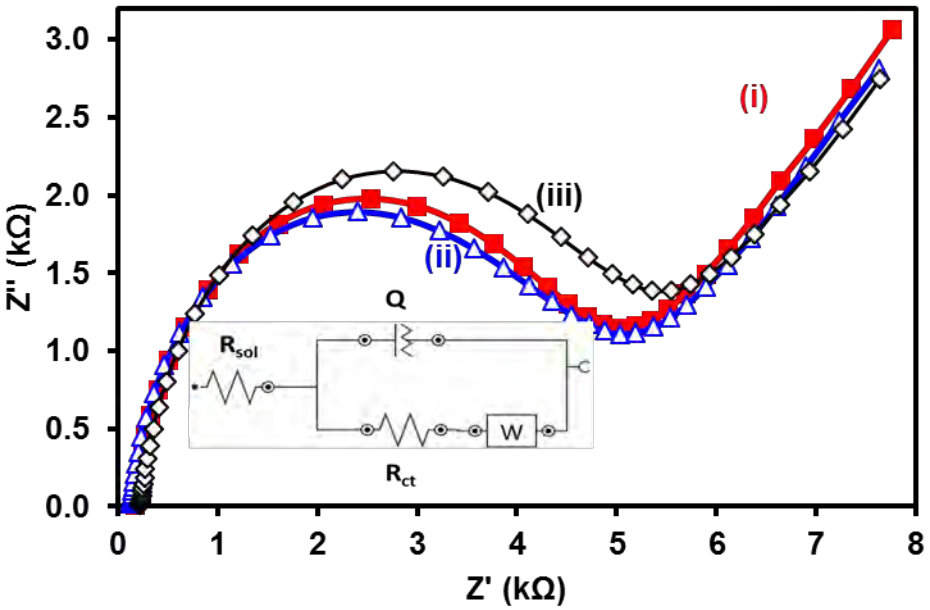

Figure 3.12: Impedance spectroscopy data (Nyquist Plot representation) for (i) ITO-PVP/ NrGONS, (ii) ITO-Pt and (iii) ITO-PVP/rGONS counter electrodes, measured in 0.2 mM $[Fe(CN)_6]^{3-/4-}$ containing 1.0 mM KCl. Inset is the Randles-Sevcik equivalent circuit used to fit the impedance data.

3.4 Evaluation of DSSCs

3.4.1 Current density vs voltage curves (J-V curves)

Two equipment setups shown in **Figs. 2.1** (automated setup) and **2.2** (home made setup) were used to evaluate the DSSCs. Equipment setup shown in **Fig. 2.2** was used to evaluate DSSCs fabricated using method **A** (photosensitised with complexes (**1**)-(**3**)) and the setup in **Fig. 2.1** was used to evaluate DSSCs fabricated via method **B** (photosensitised with complexes (**4**) and (**5**)), by current density vs voltage curves (J-V curves) shown in **Fig. 3.13** (method **A**) and **Fig. 3.14** (method **B**).

The DSSC photoanodes evaluated using setup in **Fig. 2.2** are: ITO-TiO_2-(**1**), ITO-TiO_2-(**2**), ITO-TiO_2-(**3**) and ITO-TiO_2-rGONS-(**3**) each measured against the three

counter electrodes (i) ITO-PVP/rGONS, (ii) ITO-PVP/NrGONS and (iii) ITO-Pt (J-V curves are shown in **Fig. 3.13**). The DSSC photoanodes evaluated using setup in **Fig. 2.1** are: (i) ITO-TiO_2/NrGONS-(**4**), (ii) ITO-TiO_2/rGONS-(**4**), (iii) ITO-TiO_2/NrGONS-(**5**), and (iv) ITO-TiO_2/rGONS-**5** each measured against ITO-PVP/NrGONS counter electrode (J-V and power curves are shown in **Fig. 3.14**). A complete list is shown in **Table 3.3**.

The fill factor (FF) and power conversion efficiency (η) were calculated using **Equations 3.3** and **3.4 [4,135,136].**

$$FF\ (\%) = \frac{P_{max}}{J_{sc}\ x\ V_{oc}} x\ 100 \qquad (\mathbf{3.3})$$

$$\eta(\%) = \frac{J_{sc}\ x\ V_{oc}\ x\ FF}{I_o}\ x\ 100 \qquad (\mathbf{3.4})$$

where, P_{max}, J_{sc}, V_{oc} and I_0 are the maximum power output, short circuit photocurrent density, open circuit photovoltage and intensity of incident light respectively. FF is a measure of the squareness of the J-V curve of a solar cell. A solar cell with a higher voltage has a larger possible FF since the rounded portion of the J-V curve takes up less area.

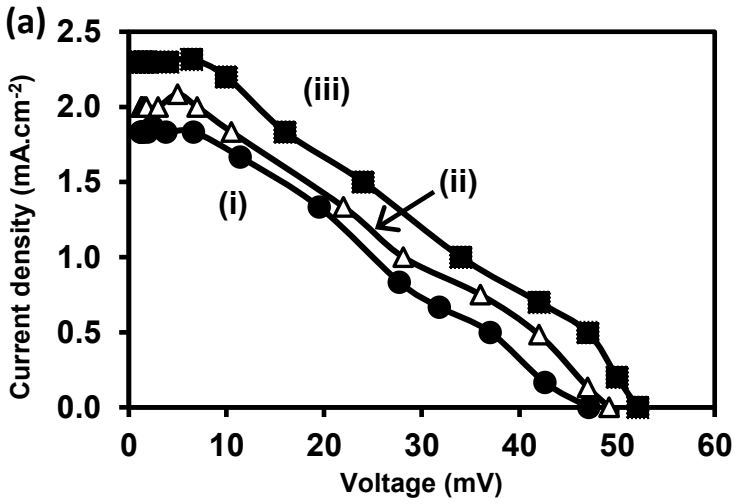

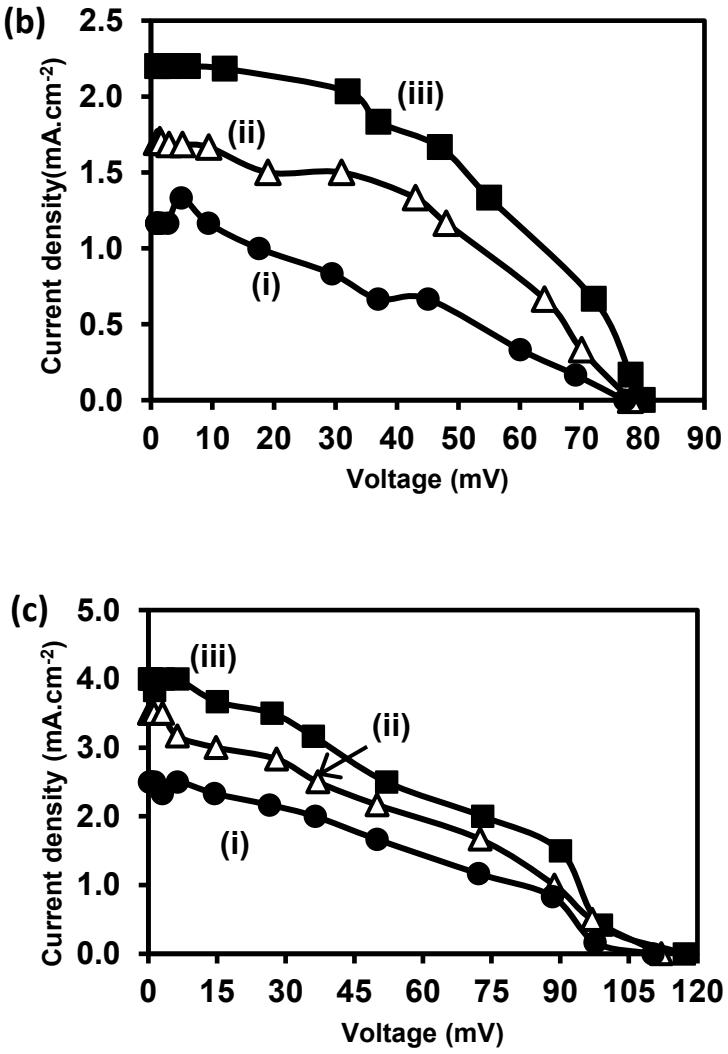

Figure 3.13: Current density versus voltage (J-V) curves for DSSCs fabricated using the following photoanodes (a) ITO-TiO_2-(**1**), (b) ITO-TiO_2-(**2**) and (c) ITO-TiO_2-(**3**) measured against the counter electrodes (i) ITO-PVP/rGONS, (ii) ITO-PVP/NrGONS and (iii) ITO-Pt.

DSSCs were fabricated using method **A** and evaluated using home assembled equipment setup in **Fig. 2.2.** Complexes (**1)**, (**2**) and (**3**) were used to photosensitize ITO-TiO_2 photoanode and complex (**3)** was further used to photosensitise ITO-TiO_2/rGONS photoanode fabricated via method **A**.

From **Table 3.3**, for DSSCs fabricated using method **A**, it can be observed that the DSSCs made with complex (**3**) as dye photosensitizer had a higher η (ITO-PVP/rGONS counter electrode 1.50%, ITO-PVP/NrGONS counter electrode 2.20%, ITO-Pt counter electrode 2.70%) compared to those sensitised with complexes (**1)** and (**2**) which had η as low as 0.50% and 0.60% respectively, with ITO-PVP/rGONS counter electrode. This may be attributed to aggregation in the solid state and electron recombination. **Figure 3.1(b)** shows solid-state absorption spectra of complexes (**1**), (**2**) and (**3**) which confirm aggregation for the first two complexes.

The η values reported in **Table 3.3** for DSSCs fabricated using method **A,** show that complex **3** had η values higher than those reported in literature at 0.13% using zinc octacarboxy phthalocynine (ZnOCPc) as dye on ZnO electrode **[170]**, at 0.77% using silicon Pc axially substituted with carboxylic acid **[142]**, and 0.92% for asymmetrical zinc phthalocyanine functionalised with catecholate **[171].** A higher η value of 3.05% was reported for asymmetrical zinc phthalocyanine functionalised with carboxylic acid **[5]**. The latter value is close to the values reported in this work for symmetrical Pcs. FF values for the symmetrical Pcs (**1**-**3**) ranged from 30 to 55% and are within the range reported in literature **[142,170]**.

Table 3.3: Dye-sensitized solar cell parameters (fill factor, FF (%) and efficiency, η (%)).

Photoanode	Counter Electrode	Fill factor (FF, %)	Efficiency (η, %)
Method A			
ITO-TiO_2-(**1**)	ITO-PVP/rGONS	30	0.50
	ITO-PVP/NrGONS	30	0.54
	ITO-Pt	30	0.66
ITO-TiO_2-(**2**)	ITO-PVP/rGONS	33	0.60
	ITO-PVP/NrGONS	43	1.04
	ITO-Pt	44	1.40
ITO-TiO_2-(**3**)	ITO-PVP/rGONS	30	1.50
	ITO-PVP/NrGONS	31	2.20
	ITO-Pt	31	2.70
ITO-TiO_2-rGONS-(**3**)	ITO-PVP/rGONS	52	1.89
	ITO-PVP/NrGONS	55	3.19
	ITO-Pt	54	3.80
Method B			
ITO-TiO_2/NrGONS-(**4**)	ITO-PVP/NrGONS	68	4.36
ITO-TiO_2/rGONS-(**4**)	ITO-PVP/NrGONS	69	4.32
ITO-TiO_2/NrGONS-(**5**)	ITO-PVP/NrGONS	69	3.80
ITO-TiO_2/rGONS-(**5**)	ITO-PVP/NrGONS	69	3.77

From **Table 3.3**, it can also be observed that DSSCs fabricated using method **A** with ITO-Pt counter electrode, show higher power conversion efficiencies η: complex (**1**) = 0.66%, (**2**) = 1.4%, (**3**) = 2.7%) compared to those with ITO-PVP/rGONS and ITO-PVP/NrGONS counter electrodes. This is in agreement with the fact that Pt is highly electrocatalytic towards triiodide reduction **[63,154]**. DSSCs with ITO-PVP/NrGONS counter electrode had power conversion efficiencies of 0.54%, 1.04% and 2.2% for complexes (**1**), (**2**) and (**3**) respectively. These are very much comparable to those of

DSSCs with ITO-Pt counter electrode, thus confirming that NrGONS is a promising candidate to replace Pt at the counter electrode. DSSCs with ITO-PVP/rGONS counter electrode had the least power conversion efficiencies (complexes (**1**): 0.50%, (**2**): 0.60%, (**3**): 1.50%). These results show that NrGONS have better electrocatalytic properties than rGONS as also observed in literature **[63,154,157]**. This can be attributed to the heteroatom doping-induced high electrical conductivity (a decrease in the charge transfer resistance at the interface of ITO-PVP/NrGONS counter electrode and electrolyte) thus enhancing collection of electrons from the external circuit.

Table 3.3 shows an improved power conversion efficiency for DSSCs fabricated using method **A** with rGONS modified TiO_2 photoanode compared to pure TiO_2 photoanode (for complex **3** only). Sharma et. al **[144]** made similar observations and they attributed the improved performance to the energy level structure of the rGONS-TiO_2 photoanode which favours electron transfer from the TiO_2 conduction band to ITO via graphene. Graphene acts as an electron transfer medium in the TiO_2 film, scavenging the generated electrons and transferring them to the collecting ITO electrode thus reducing charge recombination and back transfer reaction rates. This enhances J_{sc} **[144].**

For method **B**, TiO_2 alone was not employed due to the success of ITO-TiO_2/rGONS photoanode in method **A**. Complexes (**4**) and (**5)** were used to photosensitise ITO-TiO_2/rGONS and ITO-TiO_2/NrGONS photoanodes fabricated using method **B**. As mentioned earlier, the equipment for method **B** (screen printer), was not available at the time DSSCs for complexes (**1-3)** were developed.

Figure 3.14 (a) and **(b)** show the J-V and power curves respectively for DSSCs fabricated using method **B** and evaluated using equipment setup in **Fig. 2.1**. The

highest power conversion efficiency (η) was calculated to be 4.36 %, FF 68 % for DSSC based on ITO-TiO_2/NrGONS-(**4**) photoanode and ITO-PVP/NrGONS counter electrode. The best performing photoanodes for method **B**, in terms of higher η, are those containing NrGONS compared to rGONS. The maximum power points from the power curves in **Fig. 3.14 (b)** are 0.327 mW and 0.285 mW for the ITO-TiO_2/NrGONS-(**4**) and ITO-TiO_2/NrGONS-(**5**) based DSSCs respectively.

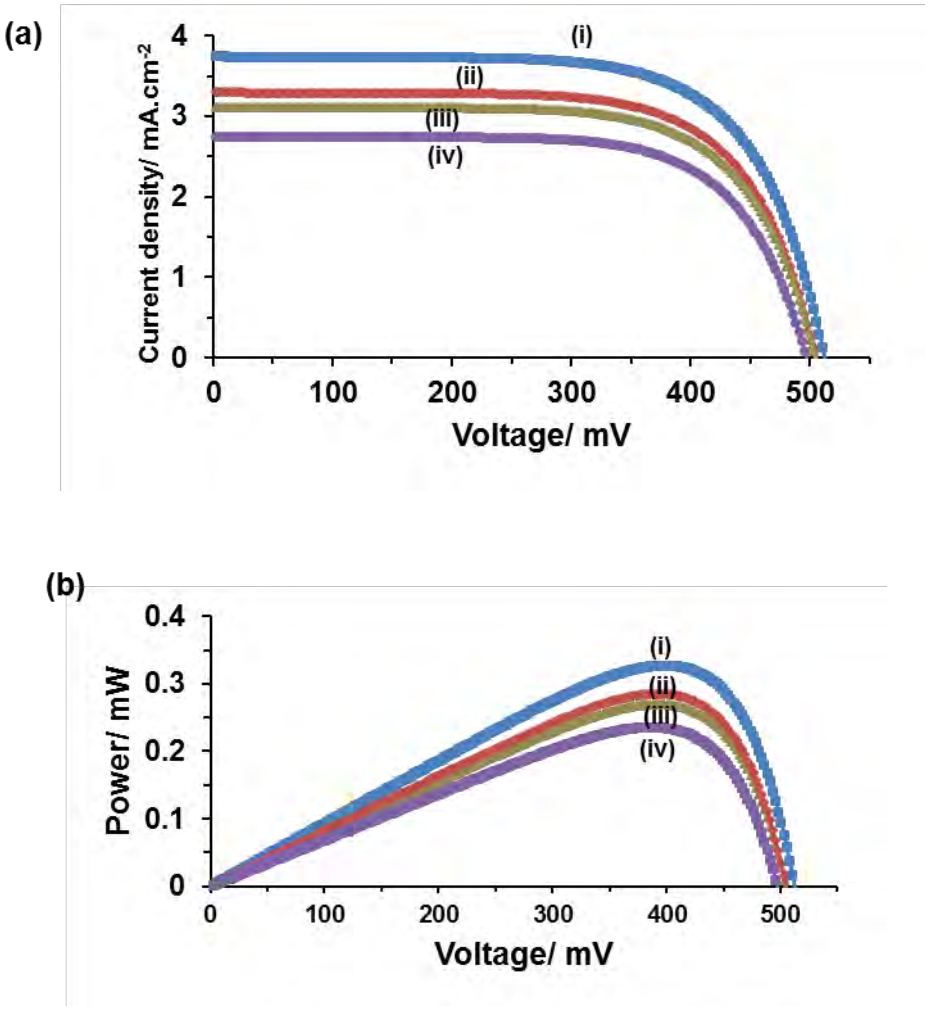

Figure 3.14: **(a)** Current density versus voltage curves (J-V curves) and **(b)** Power curves for DSSCs fabricated using the following photoanodes (i) ITO-TiO_2/NrGONS-(**4**), (ii) ITO-TiO_2/rGONS-(**4**), (iii) ITO-TiO_2/NrGONS-(**5**), and (iv) ITO-TiO_2/rGONS-(**5**), each measured against ITO-PVP/NrGONS counter electrode. DSSCs were fabricated using method **B** and evaluated using automated equipment setup in **Fig. 2.1.**

DSSCs fabricated using method **B**, generally performed better than those fabricated using method **A** and also those in literature **[5,6]**. The improvement could be due to enhancement in the fabrication process where the semiconductor was deposited using screen printing instead of using the doctor blade technique. This improves the electronic contact not only between the particles and support but also among the semiconductor particles leading to improved charge transport. The DSSC active area was reduced from 0.6 cm^2 in the first set of DSSCs (method **A**) to 0.36 cm^2 in the second set (method **B**) due to the design of the screen printer. The three bulky *tert*-butyl groups in complexes (**5**) and (**6**), also enhance solubility, minimise aggregation, act as electron releasing (push) groups and also create directionality in the excited state, thus providing an efficient electron-injection pathway into the TiO_2 conduction band. The presence of carboxyl groups allows for the immobilization of the dye photosensitizer onto the nanocrystalline TiO_2 and act as electron withdrawing (pull) groups. The significant effect asserted by the “push” and “pull” groups is evident on the current-voltage characteristics and efficiencies for second set of DSSCs (method **B**) compared to the first set of DSSCs (method **A**).

DSSCs based on complex (**4**) in method **B**, performed better than those based on complex (**5)**. This could be due to copper having higher electrical conductivity than zinc, thus providing better charge transport. These experimental results underline how the design of new dyes has to be planned to take into account the whole system **[172,173]**. Giribabu et al. **[5]** have reported a DSSC of η equal to 3.05% with an asymmetrical zinc phthalocyanine. They also suggest that η is essentially controlled by (i) the rate of electron transfer by the iodide to the oxidised phthalocyanine after electron injection and (ii) the rate of the charge recombination of the oxidised phthalocyanine with conduction band electrons.

Cid et al. **[6]** synthesized a series of asymmetrical phthalocyanines and discussed the effect the spacer between the anchoring group (COOH) and TiO_2 surface, has on the photovoltaic properties. The highest efficiency they obtained was 3.55%. In this work, a higher efficiency of 4.36% was obtained when using complex (**4**) as dye photosensitizer and NrGONS as electrocatalyst at the counter electrode.

3.4.2 Electrochemical Impedance Spectroscopy (EIS)

The main factors generally limiting the solar to electrical energy conversion efficiency in DSSCs are charge transfer and recombination at the photoanode/dye/electrolyte interface and insufficient catalytic activity at the cathode for the redox couple reduction. To investigate these interfacial characteristics, electrochemical impedance spectroscopy (EIS) experiments were carried out on DSSCs fabricated using method **B**. **Figures 3.15(a)** and **(b)** respectively show the Nyquist and Bode phase plots of EIS data for the fabricated DSSCs. Three semi circles are usually observed on the Nyquist plots representing from high to low frequencies: solution/electrolyte resistance of transport through the current collector (R_s), the charge transfer resistance (R_{ct}) at the electrode/electrolyte interface, and the electrolyte diffusion, respectively. The Nyquist plots in **Fig. 3.15(a)** show a dominating middle frequency semicircle and two not well-defined semi circles in the lowest and highest frequency regions. **Figure 3.15(a)** insert is the equivalent circuit used to fit the EIS impedance data showing solution/electrolyte resistance (R_s), charge transfer resistance at the counter electrode (R_{ct1}) and charge transfer resistance at the photoanode/dye/electrolyte interface (R_{ct2}). The values of R_s, R_{ct1} and R_{ct2} are summarized in **Table 3.4.** These values are in agreement with the trend in the power conversion efficiencies (η) whereby the DSSC

fabricated using ITO-TiO_2/NrGONS photoanode, complex (**4**) as dye photosensitizer and NrGONS photocathode, had the highest power conversion efficiency. Lower R_s, R_{ct1}, and R_{ct2} imply efficient electron transport as observed for complex (**4**) compared to (**5**). Incorporating copper as the central metal of the MPc (dye) and graphene material in the photoanode improves conductivity, enhances electron transfer and also reduces the recombination of electrons with dye or back transfer reaction **[173,174]**.

The maximum phase angles illustrated in the bode phase plots in **Fig. 3.15(b)** are less than 90 degrees expected of an ideal capacitive behaviour. This infers that the DSSC interfaces are composed of some constant phase elements (CPE) and pseudo capacitances instead of ideal capacitors. This is also confirmed by the equivalent circuit in **Fig. 3.15(a) insert** that has constant phase elements (CPE) **[144,175-178]**. ITO-TiO_2/rGONS-(**5**) DSSC had bode plots similar to those of ITO-TiO_2/NrGONS-**5**.

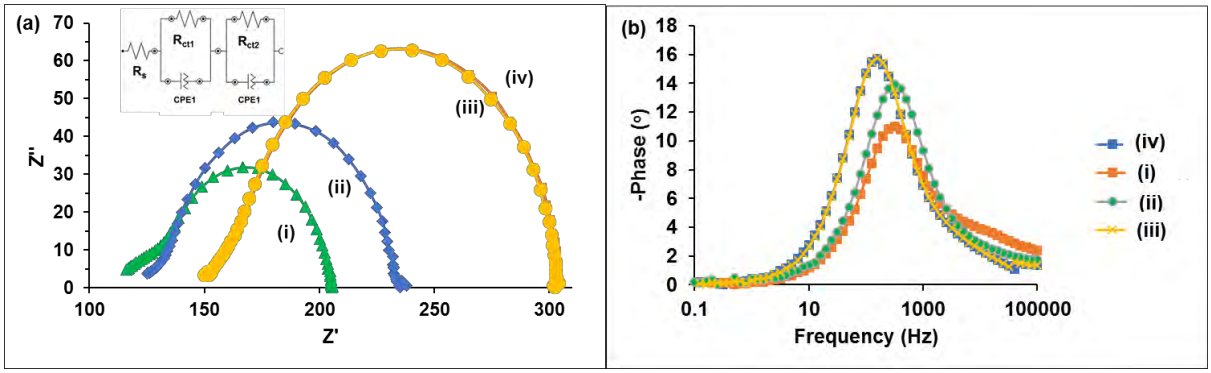

Figure 3.15: (a) Nyquist and **(b)** Bode phase plots of electrochemical impedance spectroscopy (EIS) data for DSSCs fabricated using the following photoanodes (method **B**) (i) ITO-TiO_2/NrGONS-(**4**), (ii) ITO-TiO_2/rGONS-(**4**), (iii) ITO-TiO_2/NrGONS-(**5**) and (iv) ITO-TiO_2/rGONS-(**5**). ITO-PVP/NrGONS counter electrode was used in all experiments. The Inset in (a) shows the Randles-Sevcik model used to fit the impedance data.

Table 3.4: Nyquist fitted parameter values for the DSSCs fabricated using method **B**, with an estimated error not exceeding 2%.

Photoanode		R_s/ Ω	R_{ct1}/ Ω	R_{ct2}/ Ω
(i)	ITO-TiO_2/NrGONS-(**4**)	109.18	34.071	62.451
(ii)	ITO-TiO_2/rGONS-(**4**)	113.54	35.209	88.298
(iii)	ITO-TiO_2/NrGONS-(**5**)	147.00	40.90	116.00
(iv)	ITO-TiO2/rGONS-(**5**)	148.51	23.88	131.73

3.5 Conclusions for the chapter

The synthesis and characterisation of graphene materials and metallophthalocyanines and their application in dye-sensitized solar cells (DSSCs), were discussed.

Two new metallophthalocyanines, axially substituted silicon Pc complex (**3**) and asymmetrically substituted copper Pc complex (**4**), exhibited a monomeric behaviour under the UV-Vis absorption spectra in solution typical of MPcs. The sharp and intense well-defined Q-band at 675 nm for complex (**3**) and a slightly broadened Q-band at 678 nm for complex (**5**)**.** The HOMO and LUMO energy levels of complexes (**1)**-(**5)** were found to be higher than the conduction band of TiO_2 and less than the redox (I^-/I_3^-) couple respectively, thus confirming that the MPcs can be applied in DSSCs.

Evaluation of the DSSCs showed that the DSSC fabricated using ITO-TiO_2/NrGONS-(**4**) photoanode and ITO-PVP-NrGONS counter electrode had the highest power conversion efficiency (η) of 4.36%. This can be attributed to the substituents (*tert*-butyl, carboxyl) on the MPc and the central metal (Cu). The bulky *tert*-butyl groups enhance solubility, minimise aggregation, act as electron releasing (push) groups and also create directionality in the excited state, thus providing an efficient electron-injection

pathway into the TiO_2 conduction band. The presence of carboxyl groups allows for the immobilization of the dye photosensitizer onto the nanocrystalline TiO_2 and act as electron withdrawing (pull) groups. Copper has a higher electrical conductivity thus provides better charge transport.

4. Conclusions and future prospects

4.1 Conclusions and future prospects from the first set of DSSCs (method A)

Silicon phthalocyanine (**3**) was successfully synthesised as confirmed by elemental analysis, NMR and MALDI-TOF-MS. Dye-sensitized solar cells (DSSCs) were fabricated using complex (**1**), (**2**) and (**3**) as dye-sensitizers for nanocrytstalline TiO_2 photoelectrodes and rGONS or NrGONS as electrocatalysts at the counter electrodes. rGONS modified TiO_2 photoanodes were also used. The photovoltaic characteristics: fill factor (FF) and power conversion efficiency (η) of the fabricated DSSCs were investigated. The highest power conversion efficiency obtained was 3.19% and an FF of 55% for ITO-TiO_2/rGONS photoanode, complex (**3**) as dye and NrGONS as electrocatalyst at the counter electrode. These findings are fairly promising and should encourage continued study of improving power conversion efficiencies of phthalocyanine sensitised DSSCs and graphene-based materials as electrocatalysts at the CE.

4.2 Conclusions and future prospects from the second set of DSSCs (method B)

Unsymmetrical phthalocyanines, CuPc (complex (**4**)) and ZnPc (complex (**5**)) with three bulky *tert*-butyl groups and two carboxyl groups were successfully synthesised and used for the photosensitization of a graphene oxide modified TiO_2 photoanode. The *tert*–butyl groups enhance solubility, minimise aggregation, have electron releasing ability (push) and also create directionality in the excited state. The two carboxyl groups anchor the sensitizer to the semiconductor and act as electron withdrawing (pull) groups. The sensitised photoanodes were then used in fabricating DSSCs with I^-/I_3^- liquid electrolyte and NrGONS photocathode. The DSSCs had power

conversion efficiencies η of 4.36 % and 3.80 % for the complex (**4**) and (**5**) respectively (with ITO-TiO_2/NrGONS as the photoanode and ITO-PVP/NrGONS counter electrode), which are an improvement compared to complexes (**1**)-(**3**). The probable reason for the improvement is the push-pull effect induced by the *tert*-butyl and carboxyl groups. These data contribute to the design and development of DSSCs and the findings in this study should encourage continued study of improving DSSC efficiencies.

References

[1] B. O'Regan, M. Grätzel, A low-cost, high-efficiency solar cell based on dye-sensitized colloidal TiO_2 films, Nature 353 (1991)737–740

[2] D. Schlettwein, T. Nyokong, Chapter Title: Phthalocyanines as sensitizers in dye-sensitized solar cells, Edited by K. M. Kadish, K. M. Smith, R. Guilard, Handb. Porphyrin Sci., World scientific, Singapore, 24 (2012), Chapter 114, 389-420.

[3] K. E. Jasim, In book: Solar Cells - Dye-Sensitized Devices, Dye-sensitized solar cells - working principles, challenges and opportunities, L. A. Kosyachenko (Ed.), ISBN: 978-953-307-735-2, InTech, Kingdom of Bahrain, 8 (2011) http://www.intechopen.com/books/solar-cells-dye-sensitized-devices/dye-sensitized-solar-cellsworking-principles-challenges-and-opportunities

[4] J. D. Roy-Mayhew, I. A. Aksay, Graphene materials and their use in dye-sensitized solar cells, Chem. Rev. 114 (2014) 6323−6348.

[5] L. Giribabu, Ch. V. Kumar, V. G. Reddy, P. Y. Reddy, Ch. S. Rao, Song-Rim Jang, Jun-Ho Yum, Md. K. Nazeeruddin, M. Gratzel, Unsymmetrical alkoxy zinc phthalocyanine for sensitization of nanocrystalline TiO_2 films, Sol. Energy Mater. Sol. Cells 91 (2007) 1611–1617.

[6] J.-J. Cid, M. Garcia-Iglesias, J.-H. Yum, A. Forneli, J. Albero, E. Martinez-Ferrero, P. Vazquez, M. Grätzel, M. K. Nazeeruddin, E. Palomares, T. Torres, Structure–function relationships in unsymmetrical zinc phthalocyanines for dye-sensitized solar cells, Chem. Eur. J. 15 (2009) 5130 – 5137.

[7] M.K. Nazeeruddin, R. Humphry-Baker, M. Grätzel, D. Wöhrle, G. Schnurpfeil, G. Schneider, A. Hirth, N. Trombach, Efficient near-IR sensitization of nanocrystalline TiO_2 films by zinc and aluminum phthalocyanines, J. Porphyrins Phthalocyanines 3 (1999) 230-237.

[8] M. Ince, F. Cardinali, J-H. Yum, M.V. Martinez-Diaz, M.K. Nazeeruddin, M. Grätzel, T. Torres, Convergent synthesis of near-infrared absorbing, “push-pull”, bisthiophene-substituted, zinc (II) phthalocyanines and their application in dye-sensitized solar cells. Chem Eur J 18 (2012) 6343-6348.

[9] K. Parvez, Z.-S. Wu, R. Li, X. Liu, R. Graf, X. Feng, K. M llen, Exfoliation of graphite into graphene in aqueous solutions of inorganic salts, J. Am. Chem. Soc. 136 (2014) 6083−6091.

[10] S. R. Kim, M. K. Parvez, M. Chhowalla, UV-reduction of graphene oxide and its application as an interfacial layer to reduce the back-transport reactions in dye-sensitized solar cells, Chem. Phys. Lett. 483 (2009) 124–127.

[11] S. Pei, H.-M. Chen, The reduction of graphene oxide, Carbon 50 (2012) 3210 – 3228.

[12] W. E. Ghann, H. Kang, J. Uddin, F. A. Chowdhury, S. I. Khondaker, M. Moniruzzaman, Md H. Kabir, M. M. Rahman, Synthesis and characterization of reduced graphene oxide and their application in dye-sensitized solar cells, ChemEngineering 3 (2019) 7-19.

[13] S. S. Shams, R. Zhang, J. Zhu, Graphene synthesis: a Review, Mater Sci-Poland 33 (2015) 566-578.

[14] M. S. A. Bhuyan, M. N. Uddin, M. M. Islam, F. A. Bipasha, S. S. Hossain, Synthesis of graphene, Int. Nano Lett. 6 (2016) 65–83.

[15] R. S. Edwards, K. S. Coleman, Graphene synthesis: relationship to applications, Nanoscale 5 (2013) 38-51.

[16] J. H. Warner, F. Schäffel, A. Bachmatiuk, M. H. Rűmmeli, Graphene: Fundamentals and emergent applications, Elsevier, Oxford, 2012.

[17] K. S. Novoselov, A. K. Geim, S. Morozov, D. Jiang, Y. Zhang, S. Dubonos, I. V. Grigorieva, A. A. Firso, Electric field effect in atomically thin carbon films, Science 306 (2004) 666-669.

[18] A. Dato, V. Radmilovic, Z. Lee, J.Phillips, M. Frenklach, Substrate-free gas-phase synthesis of graphene sheets, Nano Lett. 8 (2008) 2012-2016.

[19] A. Reina, X. Jia, J. Ho, D. Nezich, H. Son, V. Bulovic, Large area, few-layer graphene films on arbitrary substrates by chemical vapor deposition, Nano Lett. 9 (2008) 30-35.

[20] R. Verdejo, M. M. Bernal, L. J. Romasanta, M. A. Lopez-Manchado, Graphene filled polymer nanocomposites, J. Mater. Chem. 21 (2011) 3301-3310.

[21] S. Park, R. S. Ruoff, Chemical methods for the production of graphenes, Nat. Nanotechnol. 4 (2009) 217-224.

[22] M. Segal, Selling graphene by the ton, Nat. Nanotechnol. 4 (2009) 612-614.

[23] A. K. Geim, A. H. Macdonald, Graphene exploring carbon flatland, Phys. Today 60 (8) (2007) 35-41.

[24] L. Jiao, L. Zhang, X. Wang, G. Diankov, H. Dai, Narrow graphene nanoribbons from carbon nanotubes, Nature 458 (2009) 877-880.

[25] D. V. Kosynkin, A. L. Higginbotham, A. Sinitskii, J. R. Lomeda, A. Dimiev, B. K. Price, Longitudinal unzipping of carbon nanotubes to form graphene nanoribbons, Nature 458 (2009) 872-876.

[26] P. Sutter, How silicon leaves the scene, Nat. Mater. 8 (2009) 171-172.

[27] A. Chakrabarti, J. Lu, J. C. Skrabutenas, T. Xu, Z. Xiao, J. A. Maguire, Conversion of carbon dioxide to few-layer graphene, J. Mater. Chem. 21 (2011) 9491-9493.

[28] K. S. Kim, Y. Zhao, H. Jang, S. Y. Lee, J. M. Kim, K. S. Kim, Large-scale pattern growth of graphene films for stretchable transparent electrodes, Nature 457 (2009) 706-710.

[29] Y. Zhang, L. Zhang, C. Zhou, Review of chemical vapor deposition of graphene and related applications, Accounts Chem. Res. 46 (2013) 2329-2339.

[30] S. Bae, H. Kim, Y. Lee, X. Xu, J.-S. Park, Y. Zheng, Roll-to-roll production of 30-inch graphene films for transparent electrodes, Nat. Nanotechnol. 574 (2010) 574-578.

[31] J. Rafiee, X. Mi, H. Gullapalli, A. V. Thomas, F. Yavari, Y. Shi, Wetting transparency of graphene, Nat. Mater. 11 (2012) 217-222.

[32] D. R. Lenski, M. S. Fuhrer, Raman and optical characterization of multilayer turbostratic graphene grown via chemical vapor deposition, J. Appl. Phys. 110 (2011) 013720-013724.

[33] X. Li, W. Cai, J. An, S. Kim, J. Nah, D. Yang, Large-area synthesis of high-quality and uniform graphene films on copper foils, Science 324 (2009) 1312-1314.

[34] M. P. Levendorf, C. S. Ruiz-Vargas, S. Garg, J. Park, Transfer-free batch fabrication of single layer graphene transistors, Nano Lett. 9 (2009) 4479-4483.

[35] J. K. Wassei, M. Mecklenburg, J. A. Torres, J. D. Fowler, B. Regan, R. B. Kaner, Chemical vapor deposition of graphene on copper from methane, ethane and propane: evidence for bilayer selectivity, Small 8 (2012) 1415-1422.

[36] M. Qi, Z. Ren, Y. Jiao, Y. Zhou, X. Xu, W. Li, J. Li, X. Zheng, J. Bai, Hydrogen kinetics on scalable graphene growth by atmospheric pressure chemical vapor deposition with acetylene, J. Phys. Chem. C 117 (2013) 14348–14353.

[37] T. Chen, W. Hu, J. Song, G. H. Guai, C. M. Li, Interface functionalization of photoelectrodes with graphene for high performance dye-sensitized solar cells, Adv. Funct. Mater. 22 (2012) 5245–5250.

[38] A. J. Frank, N. Kopidakis, J. van de Lagemaat, Electrons in nanostructured TiO_2 solar cells: transport, recombination and photovoltaic properties, Coord. Chem. Rev., 248 (2004) 1165-1179.

[39] X. Wang, L. J. Zhi, K. Müllen, Transparent, conductive graphene electrodes for dye-sensitized solar cells, Nano Lett. 8 (2008) 323-327.

[40] L. J. He, J. Chen, F. Q. Bai, R. Jia, J. Wang, H. X. Zhang, The influence of a dye–TiO_2 interface on DSSC performance: a theoretical exploration with a ruthenium dye, RSC Adv. 6 (2016) 81976–81982.

[41] J. D. Roy-Mayhew, G. Boschloo, A. Hagfeldt, I. A. Aksay, Functionalized graphene sheets as a versatile replacement for platinum in dye-sensitized solar cells, ACS Appl. Mater. Interfaces 4 (2012) 2794−2800.

[42] P. J. Cameron, L. M. Peter, Characterization of titanium dioxide blocking layers in dye-sensitized nanocrystalline solar cells, J. Phys. Chem. B 107 (2003) 14394-14400.

[43] L. Meng, C. Li, Blocking layer effect on dye-sensitized solar cells assembled with TiO_2 nanorods prepared by dc reactive magnetron sputtering, Nanosci. Nanotechnol. Lett. 3 (2011) 81–185.

[44] N.Yang, J. Zhai, D. Wang, Y. Chen, L. Jiang, Two-dimensional graphene bridges enhanced photoinduced charge transport in dye-sensitized solar cells, ACS Nano 4 (2010) 887-894.

[45] B. Tang, G. Hu, Two kinds of graphene-based composites for photoanode applying in dye-sensitized solar cell, J. Power Sources 220 (2012) 95-102.

[46] Y.-B. Tang, C. -S. Lee, J. Xu, Z.-T. Liu, Z.-H. Chen, Z. He, Y.-L. Cao, G. Yuan, H. Song, L. Chen, L. Luo, H.-M. Cheng, W.-J. Zhang, I. Bello, S.-T. Lee, Incorporation of graphenes in nanostructured TiO_2 films via molecular grafting for dye-sensitized solar cell application, ACS Nano 4 (2010) 3482-3488.

[47] S. Sun, L. Gao, Y. Liu, Enhanced dye-sensitized solar cell using graphene-TiO_2 photoanode prepared by heterogeneous coagulation, Appl. Phys. Lett. 96 (2010) 083113.

[48] H. Wang, S. L. Leonard, Y. H. Hu, Promoting effect of graphene on dye-sensitized solar cells, Ind. Eng. Chem. Res. 51 (2012) 10613−10620.

[49] J. Chang, J. Yanga, P. Ma, D. Wu, L. Tiana, Z. Gao, Kai Jiang, Lin Yang, Hierarchical titania mesoporous sphere/graphene composite, synthesis and application as photoanode in dye-sensitized solar, J. Colloid Interface Sci. 394 (2013) 231-236.

[50] J. Durantini, P. P. Boix, M. Gervaldo, G. M. Morales, L. Otero, J. Bisquert, E. M. Barea, Photocurrent enhancement in dye-sensitized photovoltaic devices with titania–graphene composite electrodes, J. Electroanal. Chem. 683 (2012) 43–46.

[51] J. Song, Z. Yin, Z. Yang, P. Amaladass, S. Wu, J. Ye, Y. Zhao, W.-Q. Deng, H. Zhang, X.-W. Liu, Enhancement of photogenerated electron transport in dye-sensitized solar cells with introduction of a reduced graphene oxide–TiO_2 junction, Chem. Eur. J. 17 (2011) 10832 – 10837.

[52] Y.-C. Wang, C.-P. Cho, Application of TiO_2-graphene nanocomposites to photoanode of dye-sensitized solar cell, J. Photochem. Photobiol. A 332 (2017) 1-9.

[53] Y. Bai, Y. Cao, J. Zhang, M. Wang, R. Li, P. Wang, S. M. Zakeeruddin, M. Grätzel, High-performance dye-sensitized solar cells based on solvent-free electrolytes produced from eutectic melts, Nat. Mater. 7 (2008) 626-630.

[54] M. Grätzel, Conversion of sunlight to electric power by nanocrystalline dye-sensitized solar cells, J. Photochem. Photobiol. A 164 (2004) 3-14.

[55] M. Grätzel, Photoelectrochemical cells, Nature, 414 (2001) 338-344.

[56] J. A. Chang, J. H. Rhee, S. H. Im, Y. H. Lee, H.-j. Kim, S. I. Seok, M. K. Nazeeruddin, M. Grätzel, High-performance nanostructured inorganic-organic heterojunction solar cells, Nano Lett. 10 (2010) 2609-2612.

[57] E. Trancik, S. C. Barton, J. Hone, Transparent and catalytic carbon nanotube Films, Nano Lett. 8 (2008) 982-987.

[58] G.-r. Li, F. Wang, Q.-w. Jiang, X.-p. Gao, P.-w. Shen, Carbon nanotubes with titanium nitride as a low‐cost counter‐electrode material for dye‐sensitized solar cells, Angew. Chem. Int. Ed. 49 (2010) 3653-3656.

[59] K. Suzuki, M. Yamaguchi, M. Kumagai, S. Yanagida, Application of carbon nanotubes to counter electrodes of dye-sensitized solar cells, Chem. Lett. 32 (2003) 28-29.

[60] J. Qian, P. Liu, Y. Xiao, Y. Jiang, Y. Cao, X. Ai, H. Yang, TiO_2-coated multilayered SnO_2 hollow microspheres for dye-sensitized solar cells, Adv. Mater. 21 (2009) 3663-3667.

[61] S. Das, P. Sudhagar, V. Verma, D. Song, E. Ito, S. Y. Lee, Y. S. Kang, W. B. Choi, Amplifying charge-transfer characteristics of graphene for triiodide reduction in dye-sensitized solar cells. Adv. Funct. Mater. 21 (2011) 3729–3736.

[62] S. Casaluci, M. Gemmi, V. Pellegrini, A. Di Carloa, F. Bonaccorso, Graphene-based large area dye-sensitized solar cell modules, Nanoscale 8 (2016) 5368-5378.

[63] J.D. Roy-Mayhew, D.J. Bozym, C. Punckt, I.A. Aksay, Functionalized graphene as a catalytic counter electrode in dye-sensitized solar cells, ACS Nano 4 (2010) 6203–6211.

[64] I. Jung, D.A. Dikin, R.D. Pinter, R.S. Ruoff, Tunable electrical conductivity of individual graphene oxide sheets reduced at “low” temperatures, Nano Letters 8 (2008) 4283-4287.

[65] H.-S. Jang, J.-M. Yun, D.-Y. Kim, D.-W. Park, S.-I. Na, S.-S. Kim, Moderately reduced graphene oxide as transparent counter electrodes for dye-sensitized solar cells, Electrochimica Acta 81 (2012) 301–307.

[66] C.-T. Hsieh, B.-H. Yang, Y.-F. Chen, Dye-sensitized solar cells equipped with graphene-based counter electrodes with different oxidation levels, Diamond Relat. Mater. 27–28 (2012) 68–75.

[67] D. S. Yu, E. Nagelli, F. Du, L. M. Dai, Metal-free carbon nanomaterials become more active than metal catalysts and last longer, J. Phys. Chem. Lett. 1 (2010) 2165 – 2173.

[68] D. S. Yu, Q. Zhang, L. M. Dai, Highly efficient metal-free growth of nitrogen-doped single-walled carbon nanotubes on plasma-etched substrates for oxygen reduction, J. Am. Chem. Soc. 132 (2010) 15127 – 15129.

[69] K. P. Gong, F. Du, Z. H. Xia, M. Durstock, L. M. Dai, Nitrogen-doped carbon nanotube arrays with high electrocatalytic activity for oxygen reduction, Science 323 (2009) 760 – 764.

[70] Y. Xue, J. Liu, H. Chen, R. Wang, D. Li, J. Qu, L. Dai, Angew. Nitrogen-doped graphene foams as metal-free counter electrodes in high-performance dye-sensitized solar cells. Chem., Int. Ed. 51 (2012) 12124-12127.

[71] S. Nyoni, T. Nyokong, Electrocatalytic behaviour of cobalt tetraamino-phthalocyanine in the presence of a composite of reduced graphene nanosheets and of multi-walled carbon nanotubes, Electrochimica Acta 136 (2014) 240-249.

[72] D. Geng, Y. Chen, Y. Chen, Y. li, R. Li, X. Sun, S. Ye, S. Knights. High oxygen-reduction activity and durability of nitrogen doped graphene, Energy Environ. Sci. 4 (2011) 760-764.

[73] Z. Sheng, L. Shao, J. Chen, W. Bao, F. Wang, and X. Xia. Catalyst-free synthesis of nitrogen-doped graphene via thermal annealing graphite oxide with melamine and its excellent electrocatalysis, J. Am. Chem. Soc. 5 (2011) 4350–4358.

[74] L.-C. Chen, C.-H. Hsu, P.-S. Chan, X. Zhang, C.-J. Huang, Improving the performance of dye-sensitized solar cells with TiO_2/graphene/TiO_2 sandwich structure, Nanoscale Research Letters 9 (2014) 380-387.

[75] F. W. Low, C. W. La, Reduced graphene oxide decorated TiO_2 for Improving dye-sensitized solar cells (DSSCs), Curr. Nanosci. 15 (2019) 631-636.

[76] A. Y. Kim, J. Kim, M. Y. Kim, S. W. Ha, T. T. T. Ngyen, M. Kang, Photovoltaic efficiencies on dye-sensitized solar cells assembled with graphene-linked TiO_2 anode films, Korean Chem. Soc. 33 (2012) 3355-3360.

[77] C. Y. Neo, J. Ouyang, Graphene oxide as auxiliary binder for TiO_2 nanoparticle coating to more effectively fabricate dye-sensitized solar cells. J. Power Sources 222 (2013) 161-168.

[78] S. H. Choi, H.-M. Ju, S. H. Huh, C. K. Song, S. H. Park, B. M. Kim, A Catalytic graphene oxide film for a dye-sensitized solar cell, J. Korean Phys. Soc. 57 (2010) 1653-1656.

[79] H. Choi, H. Kim, S. Hwang, Y. Han, M. Jeon, Graphene counter electrodes for dye-sensitized solar cells prepared by electrophoretic deposition, J. Mater. Chem. 21 (2011) 7548-7551.

[80] S. Sarker, K.-S. Lee, H. W. Seo, Y.-K. Jin, D. M. Kim, Reduced graphene oxide for Pt-free counter electrodes of dye-sensitized solar cells, Solar Energy 158 (2017) 42–48.

[81] S.-Y. Jang, Y.-G. Kim, D. Y. Kim, H.-G. Kim, S. M. Jo, Electrodynamically sprayed thin films of aqueous dispersible graphene nanosheets: highly efficient cathodes for dye-sensitized solar cells, ACS Appl. Mater. Interfaces 4 (2012) 3500-3507.

[82] J.-S. Lee, H.-J. Ahn, J.-C. Yoon, J.-H. Jang, Three-dimensional nano-foam of few-layer graphene grown by CVD for DSSC, Phys. Chem. Chem. Phys. 14 (2012) 7938-7943.

[83] N.B. McKeown, In: Phthalocyanine Materials–Synthesis, Structure and Function, Cambridge University Press, vol. 6, chapt 1, pp 1-10 (1998).

[84] K. Kadish, K. M. Smith, R. Guilard (eds), In The Porphyrin Handbook: Inorganic, Organometallic and Coordination Chemistry, Academic Press, San Diego CA, USA, vol. 3, chapt. 15 (2003).

[85] F.H. Moser, A.I. Thomas, In: The Phthalocyanines: Manufacture and Applications, CRC Press, Boca Raton FL, vol. 2 (1983).

[86] J. Jeong, R. S. Kumar, I. J. Kim, Y-A Son, Synthesis characterization of symmetrical and unsymmetrical naphthoxy substituted metallophthalocyanines, Mol. Cryst. Liq. Cryst. 644 (2017) 249-256.

[87] V. K. Singh, R. K. Kanaparthi, L. Giribabu, Emerging molecular design strategies of unsymmetrical phthalocyanines for dye-sensitized solar cell applications, RSC Adv. 4 (2014) 6970-6984.

[88] K. Sakamoto, E. Okumura, R. Hirohashi, In: Phthalocyanine as functional Dyes, IPC, Tokyo, Japan, 2004.

[89] G. de la Torre, P. Vazquez, F. Agullo´-Lo´pez, T. Torres, Role of structural factors in the nonlinear optical properties of phthalocyanines and related compounds, Chem. Rev. 104 (2004) 3723-3750.

[90] J. J. Cid, J. H. Yum, S.R. Jang, M. K. Nazeeruddin, E. Martinez–Ferrero, E. Palomares, J. Ko, M. Graetzel, T. Torres, Molecular cosensitization for efficient panchromatic dye-sensitized solar cells, Angew. Chem. Int. Ed. 46 (2007) 8358-8362.

[91] S. Campidelli, B. Ballesteros, A. Filoramo, D. Diaz, G. de la Torre, T. Torres, G.M.A. Rahman, E.C. Aminur, D. Kiessling, F. Werner, V. Sgobba, D.M. Guldi, C. Cioffi, M. Prato, J.P. Bourgoin, Facile decoration of functionalized single-wall carbon nanotubes with phthalocyanines via “Click Chemistry”, J. Am. Chem. Soc. 130 (2008) 11503-11509.

[92] I. Okura, In: Photosensitization of Porphyrins and Phthalocyanines, Gordon and Breach, Amsteldijk, Netherlands, chapt. 4, pp 151 (2000).

[93] D. Dini, M. Hanack. In: Phthalocyanines properties and materials. The Porphyrin Handbook, K.M. Kadish, K.M. Smith, R. Guilard (Eds.), Academic Press New York, vol. 17, chapt. 107, pp 1-31 (2003).

[94] E. Ben-Hur, W.S. Chan, In: Phthalocyanines in photobiology and their medical applications. The Porphyrin Handbook, K.M. Kadish, K.M. Smith, R. Guilard (Eds.), Academic Press, New York, vol. 19, chapt. 117, pp 1-30 (2003).

[95] P. Gregory, Industrial applications of phthalocyanines, J. Porphyrins Phthalocyanines 4 (2000) 432-437.

[96] C.G. Claessens, U. Hahn, T. Torres, Phthalocyanines: From outstanding electronic properties to emerging applications, The Chemical Record 8 (2008) 75-97.

[97] G. Mele, R. D. Sole, G. Vasapollo, E. García-López, L. Palmisano, M. Schiavello, Photocatalytic degradation of 4-nitrophenol in aqueous suspension by using polycrystalline TiO_2 impregnated with functionalized Cu(II)–porphyrin or Cu(II)–phthalocyanine, J. Catal. 217 (2003) 334–342.

[98] D. Wöhrle, O. Suvorova, R. Gerdes, O. Bartels, L. Lapok, Efficient oxidations and photooxidations with molecular oxygen using metal phthalocyanines as catalysts and photocatalysts, J. Porphyrins Phthalocyanines 8 (2004) 1020-1041.

[99] M. Emmelius, G. Pawlowski, H.W. Vollmann, Materials for Optical Data Storage, Angew. Chem. Int. Ed. 28 (1989) 1445-1471.

[100] R. Rella, A. Serra, P. Siciliano, A. Tepore, L. Troisi, L. Valli, Characterization of novel copper phthalocyanine Langmuir-Blodgett films for NO_2 detection, Thin Solid Films 284-285 (1996) 870-872.

[101] A. N. Cammidge, H. Gopee, Macrodiscotic triphenylenophthalocyanines, Chem. Commun. 9 (2002) 966-967.

[102] M. Kimura, H. Ueki, K. Ohta, H. Shirai, N. Kobayashi, Self-organization of low-symmetry adjacent-type metallophthalocyanines having branched alkyl chains, Langmuir 22 (2006) 5051-5056.

[103] D.K.P. Ng, J. Jiang, Sandwich-type heteroleptic phthalocyaninato and porphyrinato metal complexes, Chem. Soc. Rev. 26 (1997) 433-442.

[104] R. Koeppe, N.S. Sariciftci, P.A. Troshin, R.N. Lyubovskaya, Complexation of pyrrolidinofullerenes and zinc-phthalocyanine in a bilayer organic solar cell structure, Appl. Phys. Lett. 87 (2005) 244102-244104.

[105] S. M. O' Flaherty, S. V. Hold, M. J. Cook, T. Torres, Y. Chen, M. Hanack, W. J. Blau, Molecular engineering of peripherally and axially modified phthalocyanines for optical limiting and nonlinear optics, Adv. Mater. 15 (2003) 19-32.

[106] D. Dini, M. Hanack, Phthalocyanines as materials for advanced technologies: some examples, J. Porphyrins Phthalocyanines 8 (2004) 915-933.

[107] S.B. Brown, E.A. Brown, I. Walker, The present and future role of photodynamictherapy in cancer treatment, The Lancet Oncology 5 (2004) 497-508.

[108] D. Wöhrle, G. Schnurpfeil, S. G. Makarov, A. Kazarin, O. N. Suvorova, Practical applications of phthalocyanines – from dyes and pigments to materials for optical, electronic and photo-electronic devices, Macroheterocycles 5 (2012) 191-202.

[109] A.K. Kempa, J. Dobrowolski, Palladium phthalocyanine and its polymorphic forms, Canadian J. Chem. 66 (1988) 2553-2555.

[110] Y. Chen, Y. Lin, M.E. Ei-Khouly, X. Zhuang, Y. Araki, O. Ito, W. Zhang, Supramolecular zinc phthalocyanine-perylene bisimide triad: synthesis and photophysical properties, J. Phy. Chem. 111 (2007) 16096-16099.

[111] M. Quintilian, E.M Garcia-Frutos, P.Vazquez, T. Torres, Synthesis of diiodo butadiynyl-bridged bisphthalocyaninatozinc(II) complexes, J. Inorg. Biochem. 102 (2008) 388-394.

[112] F. Dumoulin, M. Durmuş, V. Ahsen, T. Nyokong, Synthetic pathways to water-soluble phthalocyanines and close analogs, Coord. Chem. Rev. 254 (2010) 2792-2847.

[113] V.N. Nemykin, E.A. Lukyanets, Synthesis of substituted phthalocyanines, ARKIVOC, I (2010) 136-208.

[114] R.P. Linstead, Phthalocyanines. Part I. A new type of synthetic colouring matters., J. Chem. Soc. 0 (1934) 1016-1017.

[115] J. M. Robertson, An X-Ray Study of the structure of the phthalocyanines. Part 1. The metal-free, nickel, copper, and platinum compounds, J. Chem. Soc. (1935) 615-621.

[116] V. N. Nemykin, S. V. Dudkin, F. Dumoulin, C. Hirel, A. G. Gürek, V. Ahsen, Synthetic approaches to asymmetric phthalocyanines and their analogues, Reviews and Accounts, ARKIVOC, (i) (2014) 142-204, http://dx.doi.org/10.3998/ark.5550190.p008.412.

[117] T. Fukuda, K. Ono, S. Homma, N. Kobayashi, A Phthalocyanine Producing Green, Ocher, and Red Colors Depending on the Central Metals, Chem. Lett. 32 (2003) 736-737.

[118] T. Nyokong, In Chapter title: Electronic spectral and electrochemical behaviour of near infrared absorbing metallophthalocyanines, Structure and Bonding:

Functional Phthalocyanine Molecular Materials, J. Jiang (Eds.), Springer, New York, vol. 135, chapt. 2, pp 45-87 (2010).

[119] N. Kobayashi, H. Ogata, N. Nonaka, E. A. Luk'yanets. Effect of Peripheral Substitution on the Electronic Absorption and Fluorescence Spectra of Metal-Free and Zinc Phthalocyanines, Chem. Eur. J. 9 (2003) 5123-5134.

[120] N. Kobayashi, H. Konami, In Phthalocyanines: Properties and Application, C. C. Leznoff, A.B.P. Lever (Eds.), VCH, New York, 4 (1999).

[121] M. Gouterman, In The Porphyrins, Part A. Physical chemistry, Optical spectra and electronic structure of porphyrins and related rings, D. Dolphin (Ed), Academic Press, New York, vol. 3, chapt. 1, pp 1-29 (1978).

[122] L. Edwards, M. Gouterman, Porphyrins: XV. Vapor absorption spectra and stability: Phthalocyanines, J. Mol. Spectrosc. 33 (1970) 292-310.

[123] A. Henrikson, M. Soundbom, Semiempirical molecular orbital studies of phthalocyanines, Theor. Chim. Acta. 27 (1972) 213-222.

[124] D. R. Tackley, G. Dent, W. E. Smith, Phthalocyanines : structure and vibrations, Phys. Chem. Chem. Phys. 3 (2001) 1419-1426.

[125] L. Alagna, A. Capobianchi, M.P. Casaletto, G. Mattogno, M. Paoletti, G. Pennesi, G. Rossi, C. Nazionale, A.M. Paoletti, Effect of molecular packing on the solid-state spectra of ruthenium phthalocyanine: anomalous behaviour of a monodimensional stacked assembly, J. Mater. Chem. 11 (2001) 1928–1935.

[126] P. Y. Reddy, L. Giribabu, C. Lyness, H. J. Snaith, C. Vijaykumar, M. Chandrasekharam, M. Lakshmikantam, J.-H. Yum, K. Kalyanasundaram, M. Grätzel, M. K. Nazeeruddin, Efficient sensitization of nanocrystalline TiO_2 films by

a near-IR-absorbing unsymmetrical zinc phthalocyanine, Angew. Chem. Int. Ed. 46 (2007) 373 –376.

[127] L. Giribabu, Ch. Vijay Kumar, M. Raghavender, K. Somaiah, P. Yella Reddy, P. Venkateswara Rao, Durable unsymmetrical zinc phthalocyanine for near IR sensitization of nanocrystalline TiO_2 films with non-volatile redox electrolytes, J. Nano Res. 2 (2008) 39-48.

[128] L. Giribabu, C. H. V. Kumar, P. Y. Reddy, J.-H. Yum, M. Grätzel, M.D K. Nazeeruddin, Unsymmetrical extended π-conjugated zinc phthalocyanine for sensitization of nanocrystalline TiO_2 films, J. Chem. Sci. 121 (2009) 75–82.

[129] S. Cogal, S. Erten-Ela, K. Ocakoglu, A. U. Oksuz, Asymmetric phthalocyanine derivatives containing 4-carboxyphenyl substituents for dye-sensitized solar cells, Dyes and Pigments 113 (2015) 474-480.

[130] G. Tunç**,** E. Güzel, İ. Şişman, V. Ahsen, G. Cárdenas-Jirón, A. G. Gürek, Effect of new asymmetrical Zn(II) phthalocyanines on the photovoltaic performance of a dye-sensitized solar cell, New J. Chem. 43 (2019) 14390—14401.

[131] C. Chen, Y. Cheng, J. Jin, Q. Dai, H. Song, CdS/CdSe quantum dots and ZnPc dye cosensitized solar cells with Au nanoparticles/graphene oxide as efficient modified layer, J. Coll. Interface S.ci. 480 (2016) 49–56.

[132] S. Mapukata, N. Kobayashi, M. Kimura, T. Nyokong, Zinc phthalocyanine-cobalt ferrite conjugates in electrospun fibers as photocatalysts in degradation of azo dyes; Methyl Orange and Orange G, J. Photochem. Photobiol. A: 379 (2019) 112-122.

[133] C. Tshangana, T. Nyokong, Improved triplet state parameters for indium octacarboxy phthalocyanines when conjugated to quantum dots and magnetite nanoparticles, J. Mol. Stru. 1089 (2015) 161–169.

[134] D.O. Oluwole, T. Nyokong, Comparative photophysicochemical behaviour of nanoconjugates of indium tetracarboxyphenoxy phthalocyanines covalently linked to GSH-CdTe/ZnSe/ZnO, J. Photochem. Photobiol. A: Chem. 312 (2015) 34–44.

[135] K. Takechi, R. Muszynski, P. V. Kamat, Fabrication procedure of dye-sensitized solar cells. http://www3.nd.edu/~pkamat/pdf/solarcell.pdf

[136] P. Gemeiner, M. Mikula, Efficiency of dye-sensitized solar cells with various compositions of TiO_2 based screen printed photoactive electrodes, Acta Chimica Slovaca 6 (2013) 29-34.

[137] https://www.gamry.com/application-notes/EIS/basics-of-electrochemical-impedance-spectroscopy

[138] N. D. Cogger, N. J. Evans, An Introduction to Electrochemical Impedance Measurement, Technical Report No. 6 Part No.: BTR006.

[139] M. Grossi, B. Riccò, Electrical impedance spectroscopy (EIS) for biological analysis and food characterization: a review, JSSS 6 (2017) 303 - 325.

[140] M.S. Ağirtaş, C. Karataş, S. Ozdemir, Synthesis of some metallophthalocyanines with dimethyl 5-(phenoxy)-isophthalate substituents and evaluation of their antioxidant-antibacterial activities, Spectrochim. Acta A. Mol. Biomol. Spectrosc. 135 (2015) 20–24.

[141] P. Petrova, P. Ivanov, Y. Marcheva, R. Tomova, Estimation of energy levels of new Iridium cyclometalated complexes via cyclic voltammetry, Bulg. Chem. Commun.: B, 45 (2013) 159 – 164.

[142] L. Martín-Gomis, E. M. Barea, F. Fernández-Lázaro, J. Bisquert y A. Sastre-Santos, Dye-Sensitized Solar Cells using Non-Aggregated Silicon Phthalocyanines, J. Porphyrins Phthalocyanines, 15 (2011) 1004 – 1010

[143] M. N. Rani, S. Ananda, D. Rangappa, Preparation of Reduced Graphene Oxide and Its Antibacterial, Properties, Materials Today: Proceedings 4 (2017) 12300–12305.

[144] G.D. Sharma, D. Daphnomili, K.S.V. Gupta, T. Gayathri, S.P. Singh, P.A. Angaridis, T.N. Kitsopoulos, D. Tasise, A.G. Coutsolelos, Enhancement of power conversion efficiency of dye-sensitized solar cells by co-sensitization of zinc-porphyrin and thiocyanate-free ruthenium(II)-terpyridine dyes and graphene modified TiO_2 photoanode, RSC Adv. 3 (2013) 22412–22420.

[145] S. Bykkam, K.V. Rao, Ch.Shilpa Chakra, V. Rajendar, R. N. Kumar, J. Ananthaiah, Graphene Oxide Thin Films: A Simple Profilometer for Film Thickness Measurement, International Journal of Engineering and Advanced Technology, 2 (2013) 2249 – 8958.

[146] J. Rusanova, M. Pilkington, S. Decurtins, A novel fully conjugated phenanthroline-appended phthalocyanine: synthesis and characterization, Chem. Comm. (2002) 2236–2237.

[147] C. Ye, M. Li, J.L. Chen, Z. Tang, J. Pei, L. Jiang, Y. Song, D. Zhu, Photo-induced amplification of readout contrast in nanoscale data storage, J. Mater. Chem. 22 (2012) 4299-4305.

[148] J. Gierschner, J. Cornil, H.-J. Egelhaaf, Optical Bandgaps of p-Conjugated Organic Materials at the Polymer Limit: Experiment and Theory, Adv. Mater.19 (2007) 173–191.

[149] S. Pei, H. Cheng, The reduction of graphene oxide. Carbon 50 (2011) 3210-3228.

[150] A. Reina, J. Kong. R. Murali, in Graphene Nanoelectronics: From Materials to Circuits, Cht 7, 2012, Springer Science Business Media.

[151] E. Loginova, N. C. Bartelt, Peter J. Feibelman, K. F. McCarty, Evidence for graphene growth by c cluster attachment, New J. Phys. 10 (2008) 093026 (http://www.njp.org/) doi:10.1088/1367-2630/10/9/093026.

[152] P. W. Sutter, Jan-Ingo Flege, E. A. Sutter. Epitaxial Graphene on Ruthenium, Nat Mater, 7 (2008) 406–411.

[153] S. Hou, X. Cai, H. Wu, X. Yu, M. Peng, K. Yan, D. Zou, Nitrogen-doped graphene for dye-sensitized solar cells and the role of nitrogen states in triiodide reduction, Energy Environ. Sci. 6 (2013) 3356-3362.

[154] Z. Xu, H. Li, W. Li, G. Cao, Q. Zhang, K. Li, Q. Fu, J. Wang, Large-scale production of graphene by microwave synthesis and rapid cooling, Chem. Commun. 47 (2011) 1166–1168.

[155] C. Botas, P. Álvarez, C. Blanco, R. Santamaría, M. Granda, M. D. Gutiérrez, F. Rodríguez-Reinoso, R. Menéndez, Critical temperatures in the synthesis of

graphene-like materials by thermal exfoliation-reduction of graphite oxide, Carbon 52 (2013) 476-485.

[156] L.S. Panchakarla, K.S. Subrahmanyam, S.K. Saha, A. Govindaraj, H.R. Krishnamurthy, U.V. Waghmare, C.N.R. Rao, Synthesis, Structure, and Properties of Boron- and Nitrogen-Doped Graphene. Adv. Mater. 21 (2009) 4726–4730.

[157] C. A. Lin, C. P. Lee, S.T. Ho, T. C. Wei, Y. W. Chi, K. P. Huang, Jr H. He, Nitrogen-Doped Graphene/Platinum Counter Electrodes for Dye-Sensitized Solar Cells, ACS Photonics, 1 (2014) 1264−1269.

[158] M. O'Brien, B. Nichols, CVD Synthesis and Characterization of Graphene Thin Films. Army Research Laboratory. ARL-TR-5047 (2010).

[159] S. Park, K. Kim. Surface characterisation of carbon materials by X-ray photoelectron spectroscopy. Microscopy: Science, technology, applications and education, Formatex Research Center, Badajoz, Spain, 2010, Vol. 3, 1905-1916.

[160] D. R. Dreyer, S. Park, C. W. Bielawski, R. S. Ruoff, The chemistry of graphene oxide. Chem. Soc. Rev. 39 (2010) 228–240.

[161] Y. Shao, S. Zhang, M. H. Engelhard, G. Li, G. Shao, Y. Wang, J. Liu, I. A. Aksay, Y. Lin, Nitrogen-doped graphene and its electrochemical applications, J. Mater. Chem. 20 (2010) 7491–7496.

[162] M. J. Ju, J. C. Kim, H. J. Choi, I. T. Choi, S. G. Kim, K. Lim, J. Ko, J. J. Lee, I. Y. Jeon, Jong-B. Baek, H. K. Kim, N Doped Graphene Nanoplatelets as Superior Metal-Free Counter Electrodes for Organic Dye-Sensitized Solar Cells, ACS NANO. 7 (2013) 5243–5250.

[163] S. Srivastava, V. Kumar, M. A. Ali, P. R. Solanki, A. Srivastava, G. Sumana, P. S. Saxena, A. G. Joshi and B. D. Malhotra, Electrophoretically deposited reduced graphene oxide platform for food toxin detection, Nanoscale, 5 (2013) 3043–3051

[164] M. Du, J. Sun, J. Chang, F. Yang, L. Shi, L. Gao, Synthesis of nitrogen-doped reduced graphene oxide directly from nitrogen-doped graphene oxide as a high-performance lithium ion battery anode, RSC Adv., 4 (2014) 42412–42417.

[165] M. Raposo, Q. Ferreira, P.A. Ribeiro, A guide for atomic force microscopy analysis of soft condensed matter. Modern Research and Educational Topics in Microscopy. Formatex, 2007, 758-769.

[166] S. Çörekçí, K. Kızılkaya, T. Asar, M.K. Ö rk, M. Çakmak, S. Özçelí, Effects of thermal annealing and film thickness on the structural and morphological properties of titanium dioxide films, Acta Physica Polonica A, 121 (2012) 247-248.

[167] A. Henning, G. Günzburger, R. Jöhr, Y. Rosenwaks, B. Bozic-Weber, C. E. Housecroft, E. C. Constable, E. Meyer, T. Glatzel, Kelvin probe force microscopy of nanocrystalline TiO_2 photoelectrodes, Beilstein J. Nanotechnol. 4 (2013) 418–428.

[168] T. W. Hamann, R. A. Jensen, A. B. F. Martinson, H. Van Ryswykac, J.T. Hupp, Advancing beyond current generation dye-sensitized solar cells, Energy Environ. Sci. 1 (2008) 66–78.

[169] J.M.K.W. Kumari, N. Sanjeevadharshini, M.A.K.L. Dissanayake, G.K.R. Senadeera, C.A. Thotawatthage, The effect of TiO_2 photoanode film thickness on photovoltaic properties of dye-sensitized solar cells, Ceylon J. Sci., 45 (2016) 33-41.

[170] L. Jin, W. Chen, D. Chen, Synthesis and photovoltaic properties of octacarboxy-metallophthalocyanine dyes applied in dye-sensitized solar cells, J. Serb. Chem. Soc. 77 (2012) 1223–1237.

[171] A. K. Sarker, M. G. Kang, J. D. Hong, A near-infrared dye for dye-sensitized solar cell: Catecholate-functionalized zinc phthalocyanine, Dyes Pigm. 92 (2012) 1160-1165.

[172] P. Y. Reddy, L. Giribabu, C. Lyness, Efficient sensitization of nanocrystalline TiO_2 films by a near-IR-absorbing unsymmetrical zinc phthalocyanine, Angewandte Chemie, 46 (2007) 373–376.

[173] D. D. Ngoc, T. V. Nhi, Hybrid dye-sensitized solar cells based on titanium dioxide and metal – phthalocyanines, A major qualifying project report submitted to the Faculty of Worcester polytechnic institute in partial fulfilment of the requirements for the Degree of Bachelor of Science in Chemistry, Worcester, United states, 2012.

[174] G. Zanotti, N. Angelini, S. Notarantonio, A. M. Paoletti, G. Pennesi, G. Rossi, A. Lembo, D. Colonna, A. D. Carlo, A. Reale, T. M. Brown, G. Calogero, Bridged phthalocyanine systems for sensitization of nanocrystalline TiO_2 films, International Journal of Photoenergy, 2010, Article ID 136807, 11 pages, https://doi.org/10.1155/2010/136807

[175] M. Liberatore, F. Decker, L. Burtone, V. Zardetto, T. M. Brown, A. Reale, A. Di Carlo, Using EIS for diagnosis of dye-sensitized solar cells performance, J. Appl. Electrochem. 39 (2009) 2291–2295.

[176] K. I. Ozoemena, T. Nyokong, D. Nkosi, I. Chambrier, M. J. Cook, Insights into the surface and redox properties of single-walled carbon nanotube—cobalt (II) tetra-aminophthalocyanine self-assembled on gold electrode, Electrochim. Acta, 52 (2007) 4132–4143.

[177] M. K. Panda, G. D. Sharma, K. R. Justin Thomas, A. G. Coutsolelos. A new family of A2B2 type porphyrin derivatives: synthesis, physicochemical characterization and their application in dye-sensitized solar cells, J. Mater. Chem., 22 (2012) 8092.

[178] A. T. Chidembo, K. I. Ozoemena, B. O. Agboola, V. Gupta, G. G. Wildgoose, R. G. Compton. Nickel(II) tetra-aminophthalocyanine modified MWCNTs as potential nanocomposite materials for the development of supercapacitors, Energy Environ. Sci., 3 (2010) 228–236.